

1-1-2013

CMOS Low Noise Amplifiers for Wireless Body Area Networks Applications: Techniques and Designs

Mohammad Rezvani
Ryerson University

Follow this and additional works at: <http://digitalcommons.ryerson.ca/dissertations>

 Part of the [Electrical and Computer Engineering Commons](#)

Recommended Citation

Rezvani, Mohammad, "CMOS Low Noise Amplifiers for Wireless Body Area Networks Applications: Techniques and Designs" (2013). *Theses and dissertations*. Paper 1965.

CMOS Low Noise Amplifiers for Wireless Body Area Networks Applications: Techniques and Designs

by

Mohammad Rezvani

(B.A.Sc, Qazvin Islamic Azad University, 2007)

A thesis presented to the Ryerson University
in partial fulfillment of the
requirement for the degree of
Master of Applied Science
In the program of
Electrical and Computer Engineering

Toronto, Ontario, Canada, 2013

©Mohammad Rezvani 2013

AUTHOR'S DECLARATION

I hereby declare that I am the sole author of this thesis. This is a true copy of the thesis, including any required final revisions, as accepted by my examiners.

I authorize Ryerson University to lend this thesis to other institutions or individuals for the purpose of scholarly and humanitarian research

I further authorize Ryerson University to reproduce this thesis by photocopying or by other means, in total or in part, at the request of other institutions or individuals for the purpose of scholarly and humanitarian research.

I understand that my thesis may be made electronically available to the public

Abstract

CMOS Low Noise Amplifiers for Wireless Body Area Networks Applications; Techniques and Designs.

Master of Applied Science, 2013

Mohammad Rezvani

Electrical and Computer Engineering, Ryerson University

Recently, the growing advances in communication systems has led to urgent demand for low power, low cost, and highly integrated circuit topologies for transceiver designs, as key components of nearly every wireless application. Regarding to the usually weak input signal of such systems, the primary purpose of the wireless transceivers is consequently amplifying the signal without adding additional noise as much as possible. As a result, the performance of the low noise amplifier (LNA), measured in terms of features like gain, noise figure, dynamic range, return loss and stability, can highly determine the system's achievement.

Along with the evolution in wireless technologies, people get closer to the global seamless communication, which means people can unlimitedly communicates with each other under any circumstances. This achievement, as a result, paves the way for realizing wireless body area network (WBAN), the required applications for wireless sensor network, healthcare technology, and continuous health monitoring.

This thesis suggests a number of LNA designs that can meet a wide range of requirements viz gain, noise figure, impedance matching, and power dissipation at 2.4Ghz frequency based on 0.13 μ m and 65nm CMOS technologies.

This dissertation focused on the low power, high gain, CMOS reused current (CICR) LNA with noise optimization for on-body wireless body area networks (WBAN). A new design

methodology is introduced for optimization of the LNA to attain gain and noise match concurrently.

The designed LNA achieves a 28.5 dB gain, 2.4 dB noise figure, -18 dB impedance matching, while dissipating 1mW from a 1.2V power supply at 2.4 GHz frequency which is intended for WBAN applications. The tests and simulations of LNA are utilized in Cadence IC6.15 with IBM 130nm CMRF-8-SF library. The provided CICR LNA results inclusively prove the advantages of our design over other recorded structures.

In the second step, a new linearization method is proposed based on Cascade LNA structure (CC-LNA). The proposed negative feedback intermodulation sink (NF-IMS) method benefits from the feedback to improve the linearity of CC-LNA. It proves that the additional negative feedback enhances the linearity of LNA despite the previous research. Furthermore, the heavily mathematical calculations of NF-IMS technique are carried on with the proposed modified Volterra series method.

The NF-IMS method demonstrates more than 9.5dBm improvement in IIP3. Comparing to the previous techniques like: MDS and IMS, the improvement in the linearity aspect of the CC-LNA with is significant while it achieves a sufficient gain and noise performance of 16.7dB and 1.26db, respectively. Besides, the NF-IMS method presents a noise cancellation behavior as well. To increase the practical reliability of simulation, the real element model from TSMC 65nm CRN65GP library is applied. The CC-LNA that employed NF-IMS method is an excellent match with the market demands in WBAN's gateway applications.

Acknowledgements

Returning to the university and re-starting research as a master student was one of the brilliant steps in my life which could not be possible without help and support of many others. The generous people who share their time and resources with me to make this research available for others, I would like to thank all of them in front.

First of all, I would like to gratefully and sincerely thank my supervisors, Dr. Kaamran Raahemifar and Dr. Shahab Ardalan, for all of their helps, kindness, and inspiration which gave me during the difficult times in ryerson. The thesis is written under the guidance of Dr. Raahemifar whose valuable advice and extended knowledge helped me along. His mentorship was paramount in providing a comprehensive research supports and encouraging me to fostering new skills. He gave me lots of suggestions on how to come up with the best solution for research obstacles and providing proper facilities. He has also helped me during one of the important and sensitive part of my life. For that, I am forever indebted to him. I also appreciate the grate support of Dr. Ardalan for shearing his vision in field of mix-mode designs and helping me to develop my future career goals. I especially grateful his friendship during my graduate studies as well as his valuable advises and constant support of the research progress.

I would also like to thank Dr. Fei Yuan for his insightful lecturing. These technical ideas have aroused my interest in the low noise amplifier designs.

I would like to thank my parents for their faith in me, patients, and continuous supports. Allowing me to be as ambitious as I wanted, they motivated me to tackle challenges head on. I am thoroughly indebted to their generous helps. All the support they have provided me over the years was the greatest gift anyone has ever given me. My love and gratitude for them is beyond words and will last forever.

I would also wish to thank my wife for standing beside me throughout my research and for being my inspiration and motivation for continuing to improve my knowledge. Since the beginning of the project, her helpful companionship assisted me in overcoming all challenges and difficulties.

I would like to thank my amazing mother and father-in-law, for their constant encouragements I have gotten over the years, and for their support at rough times.

I would like to thank all of my grate friends and colleagues in ENG 313, Alaa, Masoud, and Yushi. Especially, I am grateful to Dr. Mohammadreza Balouchestani for his great friendship and all the good time that we had in ENG 313. Not only did I gain a lot of professional academic advises from him, but he also opened the doors of wireless body area network to me.

Finally, I thank the Allah for all the blessing, mercy, and grants.

Dedication

To Montazer, who is praying for us days and nights.

Table of Contents

AUTHOR'S DECLARATION	ii
Abstract	iii
Acknowledgements	v
Dedication	vii
Table of Contents	viii
List of Tables	xi
List of Figures	xii
List of Appendices	xv
List of Symbols and Abbreviations.....	xvi
Chapter 1 Introduction	1
1.1 Motivation	2
1.2 Applications	3
1.3 Organization of Thesis	4
Chapter 2 Back Ground Concepts.....	6
2.1 Wireless Revisers	6
2.1.1 Classical Heterodyne and Super Heterodyne Architectures.....	9
2.1.2 Homodyne Architectures	15
2.1.3 Ultra Low IF Architectures.....	20
2.2 IEEE 802.15 WBAN and MBAN	20
2.2.1 WBAN Applications.....	23
2.2.2 Network Architecture	23
2.2.3 Frequency Allocation	23
2.3 Low Noise Amplifier (LNA).....	25
2.3.1 LNA Gain	26
2.3.2 Noise Sources	26
2.3.3 Noise Factor (F) and Noise Figure (NF)	29
2.3.4 S-Parameter	32
2.3.5 Nonlinearity and large signal behavior.....	35

2.4 Optimization Techniques	38
2.4.1 Classical Noise Matching (CNM)	39
2.4.2 Simultaneous Noise and Input Matching (SNIM)	42
2.4.3 Power-Constrained Noise Optimization (PCNO).....	44
2.4.4 Power-Constrained Simultaneous Noise and Input Matching (PCSNIM)	46
2.5 Noise Cancelation Techniques	49
2.5.1 Active noise cancellation.....	49
2.5.2 Passive Noise Cancelation.....	53
2.6 Non-linearity Neutralization	54
2.6.1 Feedback.....	56
2.6.2 Derivative Supersession (DS).....	57
2.6.3 Noise and distortion cancelation.....	66
2.7 Summery	67
Chapter 3 High Gain, Low Power, CMOS Current Reused LNA with Noise Optimization	69
3.1 Analytical Approach	71
3.2 Simulation and Discussion.....	82
3.2.1 Noise Figure and Transistor's Size.....	82
3.3 Summery	85
Chapter 4 Feedback and Nonlinearity.....	87
4.1 Introduction	87
4.2 Nonlinear Analyses of Feedback.....	87
4.2.1 Volterra kernels	89
4.2.2 IIP3	94
4.3 Power series vs. Volterra Series.....	95
Chapter 5 A Novel CMOS 65 nm Low Noise Amplifier for WBAN application with Nonlinearity Neutralization	97
5.1 Introduction	97
5.2 LNA Core Design.....	99
5.3 Feedback and Nonlinearity Neutralization.....	99

5.3.1 CC-LNA Close Loop Gain	99
5.3.2 IIP3 Enhancement.....	101
5.3.3 Noise Cancelation.....	115
5.4 Simulation and Results.....	118
5.5 Conclusion.....	122
Chapter 6 Conclusion and Future work	123
6.1 Conclusion.....	123
6.2 Future work	123
Appendix A Volterra Series Tutorial.....	125
Bibliography	132

List of Tables

Table 2.1: Frequency allocation for NB-WBAN.....	24
Table 3.1: Technology dependent variables' value.	73
Table 3.2: PVT Test Result at 2.4 GHz	85

List of Figures

Figure 2.1: Block diagram of baseband tuned RF architecture.	6
Figure 2.2: BPF and image rejection.	7
Figure 2.3: Block diagram of Armstrong’s original heterodyne receiver.....	8
Figure 2.4: Block diagram of the super-heterodyne receiver.	9
Figure 2.5: The frequency scheme of a super-heterodyne receiver with; (a) high IF, (b) low IF high IF.....	10
Figure 2.6: Block diagram of a single conversion super-heterodyne receiver.	11
Figure 2.7: Block diagram of a single conversion super-heterodyne receiver with preselect tracking.	12
Figure 2.8: Block diagram of a multiple conversion super-heterodyne receiver.....	12
Figure 2.9: Block diagram of; (a) and (b) Hartley’s, (c) Weaver’s image reject receivers.	13
Figure 2.10: Mixing operation of image rejects recovers.	14
Figure 2.11: Block diagram of a homodyne receiver.	15
Figure 2.12: DC offset due to; (a) LO leakage, (b) strong interfere, (c) time-varying offset, (d) even order distortion in LNA.....	16
Figure 2.13: I/Q mismatch problem in a direct conversion receiver.	18
Figure 2.14: Block diagram of an ultra-low IF receiver.	20
Figure 2.15: WBAN applications [31].....	21
Figure 2.16: (a) Patient vital signs monitoring’s sensors in WBAN [33], (b) A three-tier architecture based on a BAN communications system [34].	22
Figure 2.17: Frequency bands for WBAN [31].	24
Figure 2.18: Power Gain.	25
Figure 2.19: Equivalent model of a resistor thermal noise.	27
Figure 2.20: Equivalent model of a substrate resistance.....	28
Figure 2.21: Induced gate noise and channel fluctuation.	28
Figure 2.22: Noise sources in typical CS LNA.....	30
Figure 2.23: Two-port noiseless network representation; (a) Z- parameters, (b) Y- parameters.	30

Figure 2.24: Equivalent noise model for noise factor calculation.	31
Figure 2.25: S-parameter representation of Two-port noiseless network.....	32
Figure 2.26: Second and third intercept point.....	35
Figure 2.27: Fundamental and higher order products of a nonlinear system.....	36
Figure 2.28: The Spurious Free Dynamic Range (SFDR) demonstration.	37
Figure 2.29: Equivalent input referred noise model for 2 pole network.....	38
Figure 2.30: SNIM optimization technique [3, 49].....	42
Figure 2.31: PCSNIM optimization technique [6, 49].....	45
Figure 2.32: Feedback and thermal noise cancellation.	48
Figure 2.33: Simple implementation of thermal noise canceller with feedback.....	49
Figure 2.34: Typical common-gate (CG) amplifier.....	50
Figure 2.35: Typical forward noise cancelation; (a) block diagram, (b) simple implementation.	51
Figure 2.36: Typical capacitor cross coupled (CCC) common-gate (CG) amplifier.....	53
Figure 2.37: Typical passive noise canceler amplifier[72].	54
Figure 2.38: Nonlinear block.	55
Figure 2.39: Block diagram of linear feedback with nonlinear forward block.....	56
Figure 2.40: NMOS current and transconductances curves.....	59
Figure 2.41: Block diagram of feedforward linearization technique.....	61
Figure 2.42: Schematic demonstration of DS method.	62
Figure 2.43: The third derivative of main and auxiliary currents.	63
Figure 2.44: Different realizations of MDS method.	64
Figure 2.45: The distortion components (a) DS (b) MDS	64
Figure 2.46: The IM3 neutralization presented by noise cancelation feedback method.	66
Figure 3.1: Flowchart of CICR Optimization.	70
Figure 3.2: (a) Schematic of a CICR LNA, (b) Small signal equivalent circuit with noise sources.	71
Figure 3.3: The CICR's forward gain in low frequency versus the ratio of inverter.....	74
Figure 3.4: Variation of A_v and NF as function of: (a) transistor width, (b) number of fingers, (c) DC biasing.	83

Figure 3.5: Variation of A_v and NF as function of: (a) degeneration inductors, (b) compensation capacitors.	84
Figure 3.6: CICR LNA with L matching at input results: (a) Forward gain, Noise Figure, and input reflection, (b) third-order intercept point (IIP3).	85
Figure 3.7: PVT test results, (a) voltage gain, (b) noise figure, (c) input matching (S_{11}).....	86
Figure 4.1: Typical CMOS LNA with negative feedback: (a) schematics' presentation, (b) equivalent block diagram.	88
Figure 5.1: Proposed NF-IMS method over optimized CC-LNA: (a) main circuit and additional blocks, (b) full schematic's presentation.	98
Figure 5.2: Equivalent block diagram of CC-LNA with NF-IMS method.	101
Figure 5.3: The S-parameters and NF result of CC-LNA with and without nonlinearity enhancement.	117
Figure 5.4: IIP3 result of CC-LNA with and without nonlinearity enhancement.	118
Figure 5.5: IIP3 as function of PMOS's width for auxiliary biasing equals to 0V.....	119
Figure 5.6: IIP3 as function of PMOS's width for auxiliary biasing equals to 0V.....	119
Figure 5.7: IIP3 and dissipation power as function of the auxiliary transistor; (a) and (b) width and biasing, (c) and (d) number of fingers and biasing	121

List of Appendices

Appendix A: Volterra Series Tutorial.....	125
---	-----

.

List of Symbols and Abbreviations

AGC	Automatic Gain Control
AM	Amplitude Modulation
A_v	Voltage Gain
BAW	Bulk Acoustic Filter
<i>BNL</i>	Background Noise Level
BPF	Band Pass Filter
<i>BW</i>	Band Width
CCC	Capacitor Cross Coupled
CE	Consumer Electronics
CFDR	Compression-Free Dynamic Range
CG	Common-Gate
C_{gb}	Gate-Body Capacitor
CICR	CMOS inverter current reused
CNM	Classical Noise Matching
C_{ox}	Gate Oxide capacitance per unit area
CS	Common Source
DSM	Deep Submicron
DSP	Digital Signal Processing
DUT	Device Under Test
ECG	Electrocardiogram
EEG	Electroencephalography

EFC	Electric Field Communication
EMG	Electromyography
f	Frequency
FM	Frequency Modulation
FM-UWB	Wideband Frequency Modulation
FSK	Frequency Shift Keying
G_A	Available Gain
G_C	Conversion Gain
g_{d0}	Drain-Source Conductance @ $V_{DS} = 0$
g_{mb}	Back Gate Transconductance
G_p	Operating Gain
G_T	Transducer Gain
HBC	Human Body Communication
HPF	High Pass Filter
IIP2	Second-Order Intermodulation Intercept Point
IIP3	Third-Order Intermodulation Intercept Point
IM	Image Signal
IM3	Third-Order Inter-Modulation
IM2	Second-Order Inter-Modulation
IMD	Intermodulation Distortion
ISM	Industrial, Scientific, and Medical

$\overline{i_n^2}$	Current Noise Source
$\overline{i_{nd}^2}$	Drain Current Noise
IP2	Second Order Intercept Point
IP3	Third Order Intercept Point
I/Q	In-phase/Quadrature
IRF	Image Rejection Filter
IRR	Image Rejection Ratio
IR-UWB	Impulse Radio UWB
k	Boltzmann's Constant
LNA	Low Noise Amplifier
LO	Local Oscillation
MAC	Medium Access Control
MICS	Medical Implant Communications Service
NB	Narrow Band
NF	Noise Figure
OIP2	Output Second-Order Intercept Point
OIP3	Output Third-Order Intercept Point
O.S	Open Circuit test
P_{1-dB}	1-dB Compression Point
P_{Avn}	Available Power from Network
P_{Avs}	Power Available from Source
PCNO	Power-Constrained Noise Optimization

PCSNIM	Power-Constrained Simultaneous Noise and Input Matching
PHY	Physical
P_{in}	Delivered Power to the Input
P_L	Delivered Power to the Load
PS	Personal Server
R	Resistance
RF	Radio Frequency
R_{sub}	Substrate Resistance
SAW	Surface Acoustic Filter
S.C	Short Circuit test
SFDR	Spurious Free Dynamic Range
S_{i_n}	Noise Density as Current
SNIM	Simultaneous Noise and Input Matching
SNR	Signal-to-Noise Ratio
S_{v_n}	Noise Density as Voltage
T	Absolute Temperature
TDMA	Time Division Multiple Access
UWB	Ultra Wideband
V_{DS}	Drain-Source Voltage
V_{in}	Input Signal Voltage

$\overline{v_n^2}$	Voltage Noise Source
V_{out}	Output Signal Voltage
WBAN	Wireless Body Area Networks
WMTS	Wireless Medical Telemetry Services
ω	Angular Frequency
Z_o	Transmission line characteristic

Chapter 1

Introduction

The increasing number of wireless application products necessitates and integrable transceivers realization. Recent achievements in microelectronics, CMOS technology and wireless communications systems pave the way for system-on-chip (SOC) applications, due to the technology scaling, low-cost, and high level of integration [1].

In every radio receivers, the low noise amplifiers (LNA) are one of the most important stages, due to their dominating role in the transceiver's sensitivity. There are several tradeoffs involved in LNA design including noise figure (NF), forward gain, power dissipation, impedance matching, and linearity.

Considering the critical importance of LNA design, various techniques have been reported to satisfy the gain, noise figure, and other requirements simultaneously. Namely, classical noise matching (CNM) [2], simultaneously noise and input matching (SNIM) [3], power-constrained noise optimization (PCNO) [4], and power-constrained simultaneously noise and input matching (PCSNIM) [5, 6] techniques are the practical strategies. However, these techniques mainly suffered from several issues that prevent their application for highly integrated requirement. For example, these methods are only investigated for common source and cascade topologies and single-transistor LNA circuits. In addition, the complicated optimization of the CMOS inverter current reused (CICR), which generally provide higher gain without sacrificing other features, are missed. These methods are merely accounting the transistor noise source and neglecting the significant effect of other ones, the obtained NF is not the optimum value.

Facing with these challenges demands new techniques to come up with a practical solution for designing optimum LNAs. With the objective to design an LNA of higher performance and finding a solution for the above issues, a new optimization method is derived. This method is based on the noise parameter equations and clear understanding of the principal and concepts. The provided CICR LNA demonstrated a 28.5 dB gain, 2.4 dB noise figures, -18 dB impedance matching and dissipating 1mW at the 2.4 GHz frequency.

Moreover, in this thesis a novel linearization method for gateway applications is discussed using Cascaded-LNA (CC-LNA) design. Acceptable gain, linearity improvement, adding no more elements to the former structures, and having no side effect on NF and gain set this technique apart from previous ones. As a result, based on the proposed method we design a practical LNA for gateway applications with more than 15dB gain and 2dBm IIP3.

1.1 Motivation

With recent advances in wireless communication, CMOS integrated circuits, radio frequency CMOS technology and system-on-chip design, the envisioned goal of wireless systems to achieve the unlimited connection for everyone at any time is going to be realized. These achievements allow the implementation of the wireless body area networks (WBAN) as a collection of sensor nodes for human body monitoring and the surrounding environment control.

According to the elderly population growth and the increasing rate of healthcare expenditure, non-intrusive ambulatory WBAN is become necessary to remotely monitor the body status and vital signs.

Due to the fact that these applications demand for lightweight compact package, there is an urgent need for highly integrable ICs for transceivers and system-on-chip technologies. The performance of such transceivers is consequently depended on that of each individual stage, especially the low noise amplifier (LNA) block as a critical block of the radio receiver due to its dominating noise characteristics in determining the total noise figure of the device.

This thesis focused on designing and optimizing a low power, low-cost, and highly integrated LNA topology that can meet IEEE 802.15.6 protocol, as WBAN application's standard. Having high voltage gain, minimum noise figure, and low power dissipation as well as being highly integrable are targeted as the design's achievements.

Our significant incentive for developing the presented LNA optimization technique was the ubiquitous demand for an economical low-power high-gain wireless device that could operate effectively beyond 10-meter distances. We choose the CMOS inverter structures from the current reused families owing to their high gain amplification that provide long distance

transmissions. However, in contrary to the similar topologies such as common-source noise optimizations that have been fully discussed in the recent decades, there was no attempt for CICR investigation due to its analytical complexities.

The other goal that we were seeking for was attaining gateway design with acceptable gain, greater than 15dB, and high linearity. With this aim in mind, we establish a novel linearization technique employing Cascaded-LNA (CC-LNA). Compared to the previous methods, this technique provides a 1.5dB linearity improvement without any side effect, such as NF degradation or gain reduction. The importance of the suggested method will be more evident when one considers that all these advantages are obtained with no additive element, either transistor or capacitor/inductor.

1.2 Applications

The demand for RF wireless transceiver that can meet the WBAN requirements has been in the center of attention, due to the impending health crisis regarding growing elderly population and health financial problems. It is predicted that the world elderly population will be doubled by the year 2025 while their healthcare expenses will be tripled [7]. This new challenge urges researchers, industrialists, and governments toward prompt and operational health solutions.

One promising and economical solution for this problem is remote health monitoring of patient's vital signs and real-time updating of the records through wireless systems. The advances of this continuous body functions' monitoring over traditional method is providing a complete picture of the patient's medical condition without being affected by disturbing factors like abrupt anxiety or elevated pressure.

The most appealing application area of the suggested LNA optimization is wireless sensor and gateway designs. In fact, one of the marketable advantages of this design is cost-efficiency and low power consumption. To illustrate, on-body wireless sensors are portable and must operate properly with limited power batteries. In addition, they should be economical enough for the patient to easily afford alternative ones in case of their lost, which often occurs due to their portability. These requirements could be well-implemented using the presented ultra-

low power inexpensive devices. In the case of gateway applications, however, there is no need to a low-power performance since they are directly connected to the power line. Instead, the high interference of numerous systems operating in the same frequency range as WPAN, such as WBAN, Bluetooth, and ZigBee applications are a serious challenge that necessitate high level of linearity.

To implement these applications, the compact, low-power, and lightweight system-on-chip tend to be unavoidable. As the key component of every RF wireless transceiver is LNA, the demand for highly integrated, low power, optimal designs is of great importance.

To achieve these required characteristics, this dissertation explores different receiver and LNA topologies and suggests a proper solution to minimize power dissipation, lower the size, and enhance gain and noise figure parameters.

1.3 Organization of Thesis

The first part of this dissertation explores different receiver topologies and describes IEEE 802.15.6, the WBAN standard. The LNA characteristics such as gain, noise figure, are briefly introduced. In addition, noise optimization, noise cancelation, and nonlinearity neutralization techniques are investigated.

Chapter 3 of the dissertation focused on the CMOS inverter LNAs. For the first time, a new method of optimization method for this family of LNA is introduced. Furthermore, the designed CMOS inverter current reused (CICR) LNA based on this optimization presents for the WBAN on-body wireless sensors. The introduced design optimization methodology attains gain and noise match concurrently.

In Chapter 4, a comprehensive nonlinearity calculation methodology is introduced based on the Volterra series. Based on this method, the nonlinearity behavior of a circuit that suffers from the nonlinear amplifier and memory effects is investigated. Besides, a comprehensive comparison is conducted between the results of this method and previous published ones in order to demonstrate the precision and performance of the Volterra series.

Chapter 5 mainly discusses about a novel linearization method. The negative feedback intermodulation sink (NF-IMS) nonlinearity neutralization technique is a new method that

benefits from the derivation superposition and intermodulation sink method simultaneously by employing a negative feedback. Based on this method, a cascade LNA is designed for the WBAN gateway applications.

Chapter 6 reflects the conclusion and future works of this research.

Chapter 2

Back Ground Concepts

2.1 Wireless Revisers

At the latest of 19th century the first wireless architecture was introduced by H. Hertz [8]. The aim of Hertz's research was to justify the Maxwell's equation radio wave. Later on, the first radio receiver was established by G. Marconi. Simultaneously to Marconi, Sir O. J. Lodge developed the theory of the tunable radio receivers. Later in 1898 and 1899, Lodge and Marconi patented their receivers that are identified as begging of commercial wireless communication age [9, 10]. The band selectivity and signal detection for all of these receivers were processed at the transmitting frequency which was few Mega Hertz. These types of receivers are identified under the baseband tuned RF architecture (Figure 2.1).

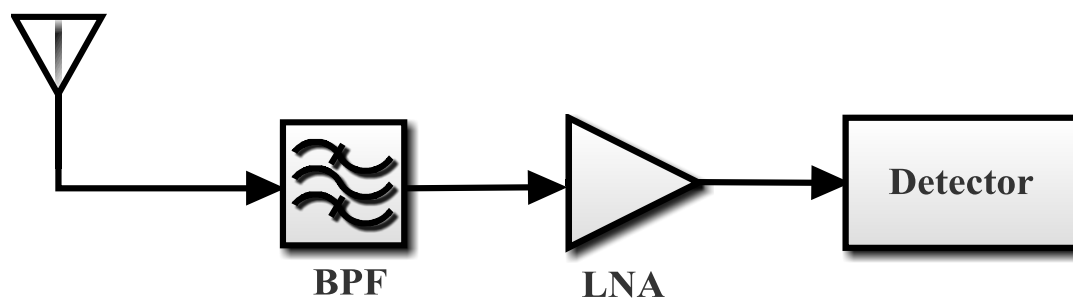


Figure 2.1: Block diagram of baseband tuned RF architecture.

The proposed receivers with the principal of the baseband RF tuned architecture were suffered from different issues; like high order band pass filter, high level of complexity, and production cost. However, along with all of these issues, the most sophisticated problem was sharing the spectrum with other transmission's stations. Due to the growing in the number of the transmitters, the limitations of using the baseband architecture were rapidly raised up.

To solve channel problem, the new architectures like classical Heterodyne were introduced in [11]. These new classes have been able to modulate and demodulate the signal's spectrum to and from the higher frequency, respectively. In other words, they made a bridge to the higher channel by translating the signal's spectrum. However, before intending to discuss

about the different architectures, it is necessary to study the two major issues that all the transceivers are suffering from; the image rejection ratio and dynamic range of receiver.

The selectivity in receiver is defined as ability to pick up the desirable signal among other signals which lay in at spectrum. To achieve this goal at the theory of architectures, a very sharp band pass filter is employed. However, because of the limitations are faced in implementation of such high order filter with small fraction of bandwidth, designers are migrated to use other filters technology, like; Bulk Acoustic Filter (BAW), Surface Acoustic Filter (SAW), and other piezoelectric filters. Based on the topology of the filter, the tuning option would be available. To avoid reaching the image signal (IM) to the signal detector, this band pass filter should have a center frequency of RF signal and bandwidth smaller than 4 times of intermediated frequency (IF) (Figure 2.2). After demodulation, the IF signals includes both of the desirable and neighbor channels. To remove these intruder channels, the IF band pass filter is implemented with bandwidth that includes 0-IF interval.

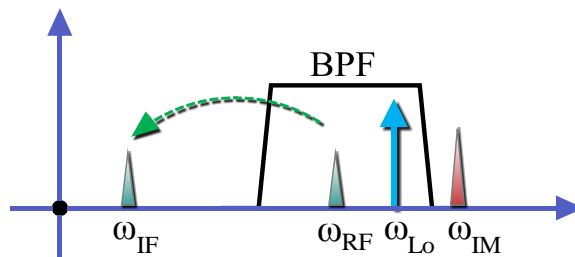


Figure 2.2: BPF and image rejection.

The value of intermediate frequency should be chosen by designer base on the trade of between the area and power. If a high value is assigned to the IF, the order of both filters would be dropped. At the same time, the signal detector, which usually is an analog to digital converter (ADC), consume more power in order to operate at the higher frequency. In the case of the lower IF, the power consumption of ADC decreased. On the other hand, the design of the band pass filter is an extremely tuff task. As a result of the smaller bandwidth, the order and complexity of the filters are dramatically increasing which is impossible to meet the on-chip design's requirement.

The dynamic range of a RF receiver is essentially defined as the range of the signal levels over which it can operate. This characteristic is considered when the ability of handling a strong signals as well as picking up a weak ones is studied. These two features are limited by the noise figures and the nonlinearity of low noise amplifier (LNA) and mixers. The bottoms and tops of this range are governed by the sensitivity to the weak signals and conductivity towards the strong signals and overloads. The value of dynamic range shows up when the receiver tries to hear a weak signal that is surrounded by strong neighbors. Under this circumstances, the capability of the pre-selection band pass filter, which stands before front-end blocks (LNA and mixer), could not make action against the strong interferes. At this point, the two new problems will stand out, the intermodulation distortions' productions of the interferes due to nonlinearity of the front end blocks, and its direct translation to the IF domain. Thus, the unwanted translated signal will add at the top of the IF signal and can led to the saturation in IF blocks and losing the data.

In the summary, a receiver with poor dynamic range which suffers from problems like intermodulation distortion, filtering and blocking may mask out the weak signal, regardless of the high level of sensitivity that receiver may have. On the other hand, the receivers with wide dynamic range but poor selectivity may lose the signal as well.

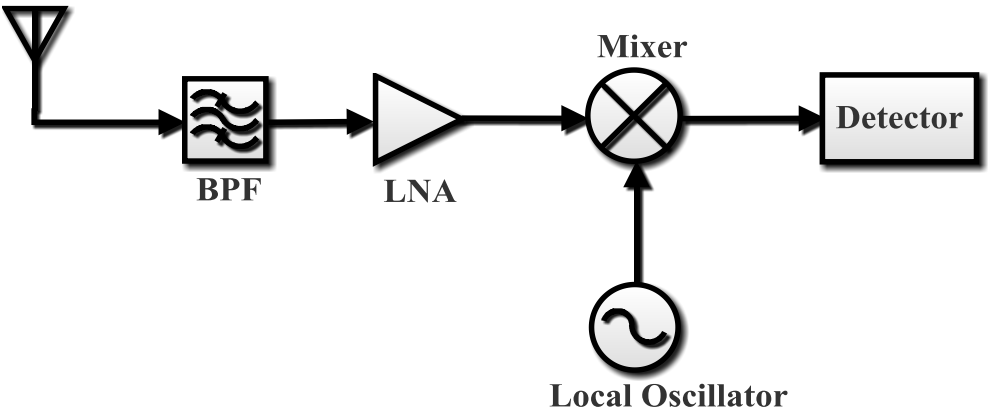


Figure 2.3: Block diagram of Armstrong's original heterodyne receiver.

2.1.1 Classical Heterodyne and Super Heterodyne Architectures

Converting an RF signal to a lower frequency by heterodyning was investigated in 1918 by Armstrong [11]. The Armstrong's receivers block diagram is depicted in Figure 2.3. The high sensitivity and selectivity made this architecture the best one for receivers that characterized by:

- Input signal amplification at low frequency, which is easier to attain high gain.
- Lower regenerate feedback and instability, owing to amplification at two different frequencies.
- Easier high order and narrow band filtering, due to the low frequency operation rather than RF.
- Ease of adjustment of low frequency IF pass band filter by tuning heterodyne oscillator frequency.

In super-heterodyne receivers, the signal is down converted from RF frequency to IF and then to pass band. As shown in Figure 2.4, the amplified RF signal is converted to a lower IF frequency and amplified again by a tuned IF stage including demodulating band pass filters. An inductor load is mostly used in low noise amplifiers to resonate with tank capacitor.

Due to the fact that RF filter's fractional bandwidth is not precise, the RF signal must be

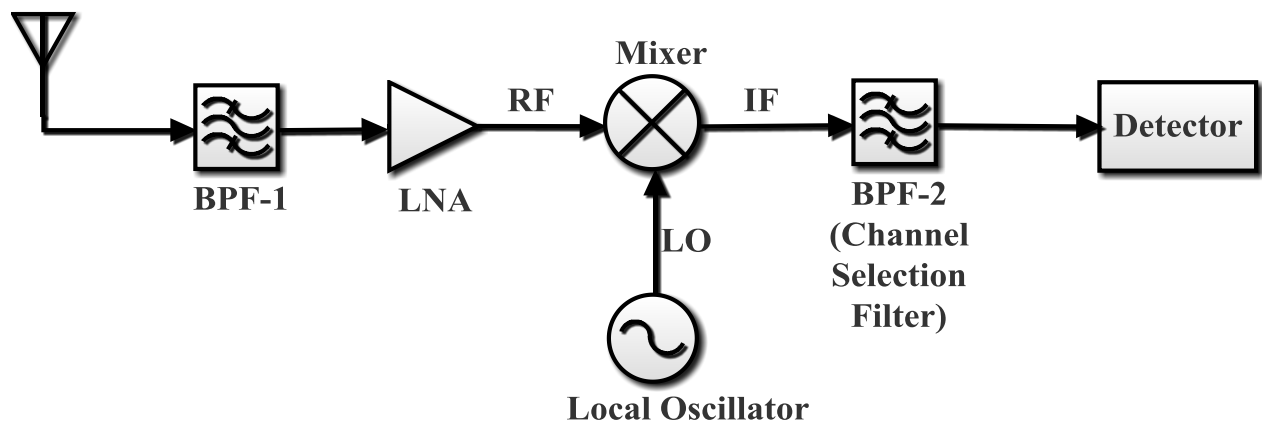
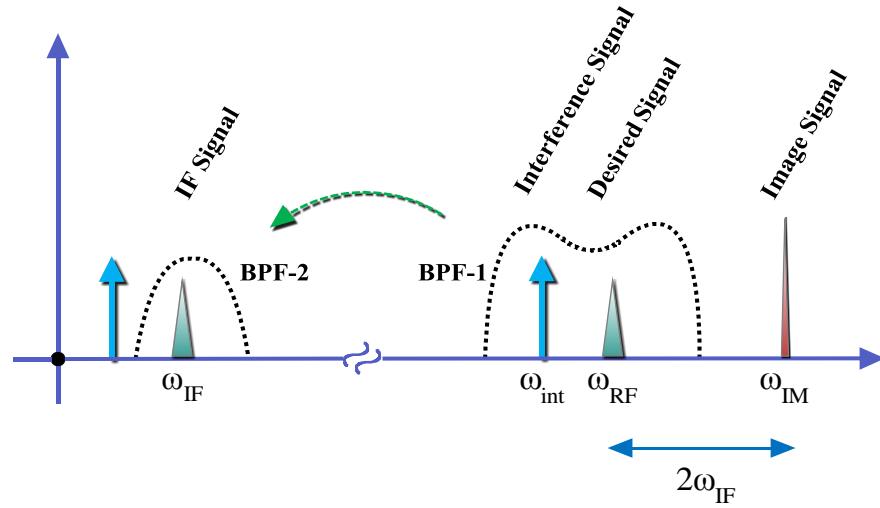
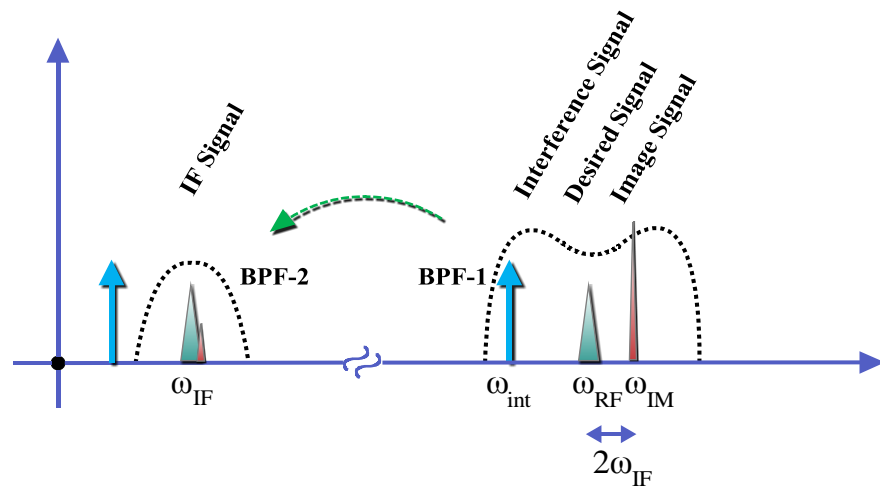


Figure 2.4: Block diagram of the super-heterodyne receiver.



(a)



(b)

Figure 2.5: The frequency scheme of a super-heterodyne receiver with; (a) high IF, (b) low IF high IF.

converted down to IF by variable frequency local oscillators. The image rejection filters remove the image signal and then, the desired channel is selected by fixed IF center frequency filters. In the heterodyne receivers, the frequency bands adjacent to local frequency are converted to the IF

frequency. As a result, if the signal with $\omega_{RF} = \omega_{LO} - \omega_{IF}$ is also converted to that same frequency, which must be suppressed before conversion. The high selective super heterodyne receiver's limitation emerged in low power wireless receivers which must usually select weak channels in the band including interferer channels side by side the desire ones. As a result, there is trade-off between image rejection (sensitivity) and interferer channel suppression (selectivity) [1].

Figure 2.5 depicts the two possible heterodyning. As depicted in Figure 2.5.a, high IF frequency selection results in great attenuation in the image signal without interferer signal suppression. In contrast, in low IF frequency heterodyning, the adjacent channel suppression is obtained while the mixed down signal is corrupted by the image, depicted in Figure 2.5.b. Thus, the IF stage must have a wide dynamic range in order to be not only sensitive to weak signals, but also selective in handling desired signal among interfering ones [12].

The high amplification and filtering, which used in analog cellular phones and television, leads to higher power dissipation and high Q filtering demanded for removing interferers. It also increases the number of passive components and as a result the receiver cost [13].

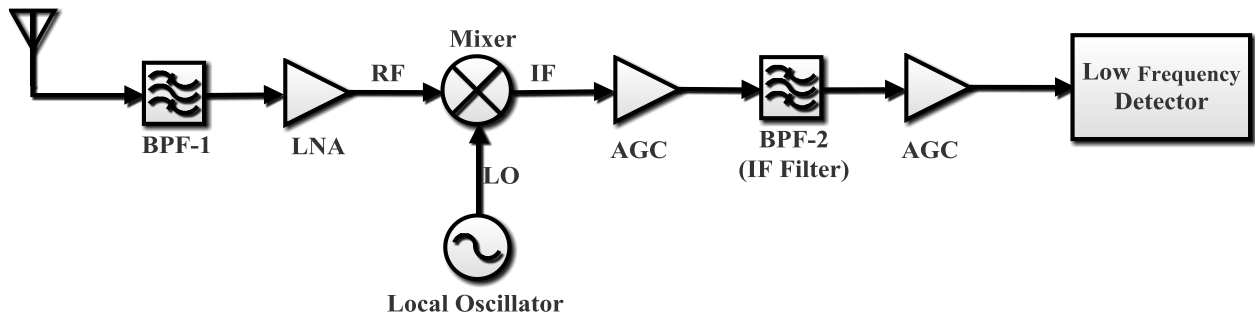


Figure 2.6: Block diagram of a single conversion super-heterodyne receiver.

2.1.1.1 Single and Multiple Conversion Technology

In a single conversion super-heterodyne receiver, a preselect filter is used for image rejecting and undesired band filtering [14]. Figure 2.6 depicts the block diagram of this structure. As the BPF is the first stage of the architecture, it needs to have a low noise figure and insertion

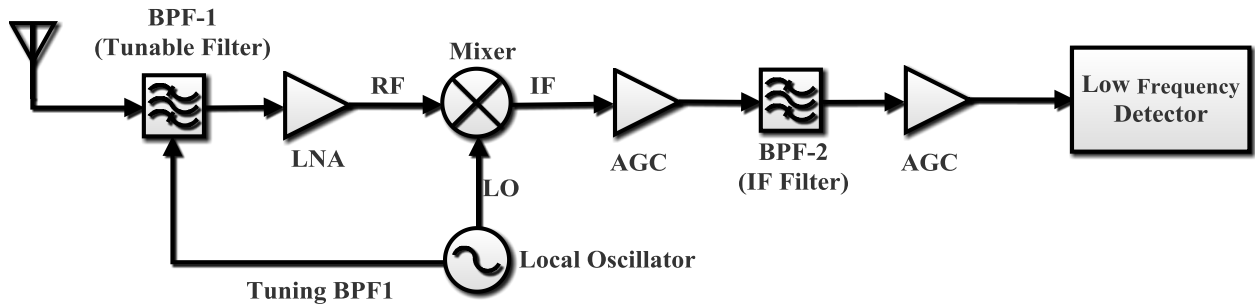


Figure 2.7: Block diagram of a single conversion super-heterodyne receiver with preselect tracking.

loss. Then, the selected signal is amplified by an LNA to guarantee the desired noise figure in the following stages including passive elements. The designed LNA must be such that no input dynamic range degradation occurs. In the next step, the amplified RF signal is converted to the IF by the mixer. Next, the out band IF signal suppression and further image rejection are provided by an image rejection filter (IRF). Following this step, an automatic gain controller (AGC) can be utilized to provide the demodulator's required gain [14].

A single conversion architecture with low order IF filter can only handle the narrowband RF input signals. Thus, a wideband RF input signal requires either a multiple conversion technique or a tracking filter design [15]. Figure 2.7 shows a single conversion topology using tracking preselect filter with a smaller bandwidth compared to the service band. However, the implementation of this topology is difficult due to its requirement such as preselected filter which is related with local oscillator, and narrowband tunable RF filter.

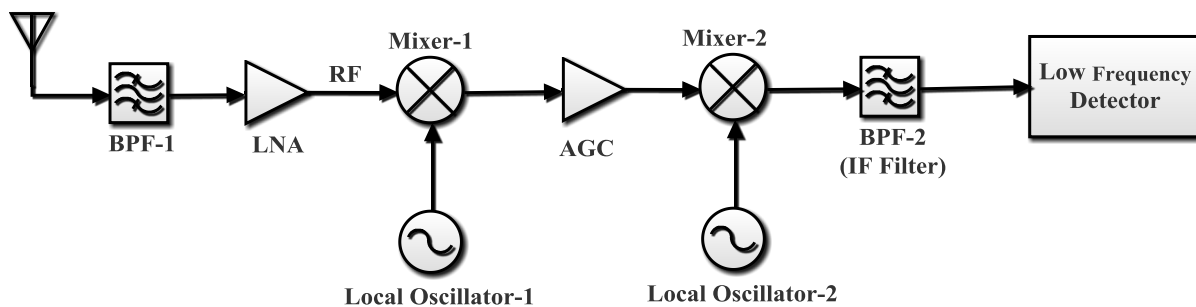


Figure 2.8: Block diagram of a multiple conversion super-heterodyne receiver.

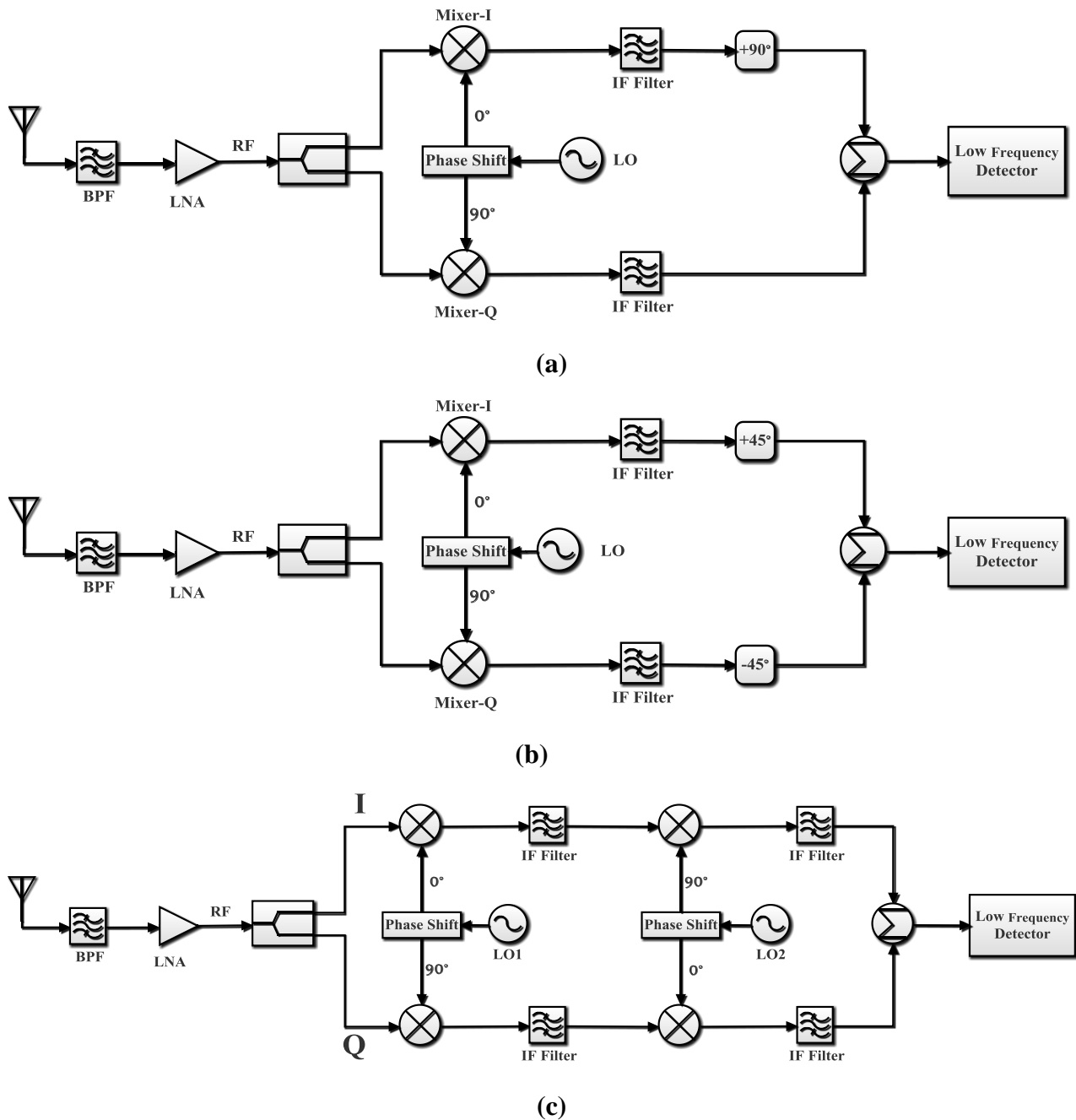


Figure 2.9: Block diagram of; (a) and (b) Hartley's, (c) Weaver's image reject receivers.

Figure 2.8 depicts a multiple conversion receiver as another approach, in which the input RF signal is down converted in two stages: first to a higher IF and then to the desire IF

frequency. By adopting technique the requirement of high Q filter is eliminate at the price of extra mixer, local oscillator, and filter [15].

2.1.1.2 Image Reject Receiver

A receiver with image rejection mixer can somewhat relax the IF filter requirements. Figure 2.9 shows the block diagram of Hartley [16] and Weaver [17] receivers, respectively. Using image rejection mixer, the outputs at point A and B of both structures are in phase for the desired signal, while they are out of phase for the image one. As a result, by summing them the image is removed [1]. The mixing operation of this receiver is illustrated in Figure 2.10.

In practice, the precision 90° phase is hard to achieve due to the mixers, mismatching, thus the rejection will be around 30-40 dB [15, 18]. The image rejection ratio (IRR) is defined as Eq. 2.1:

$$IRR = \frac{1 + (1 + \varepsilon)^2 - a(1 + \varepsilon) \cos(\theta)}{1 + (1 + \varepsilon)^2 + a(1 + \varepsilon) \cos(\theta)} \quad 2.1$$

where a is the LO amplitude, ε is the relative voltage gain mismatch, and θ is imbalance in radiation.

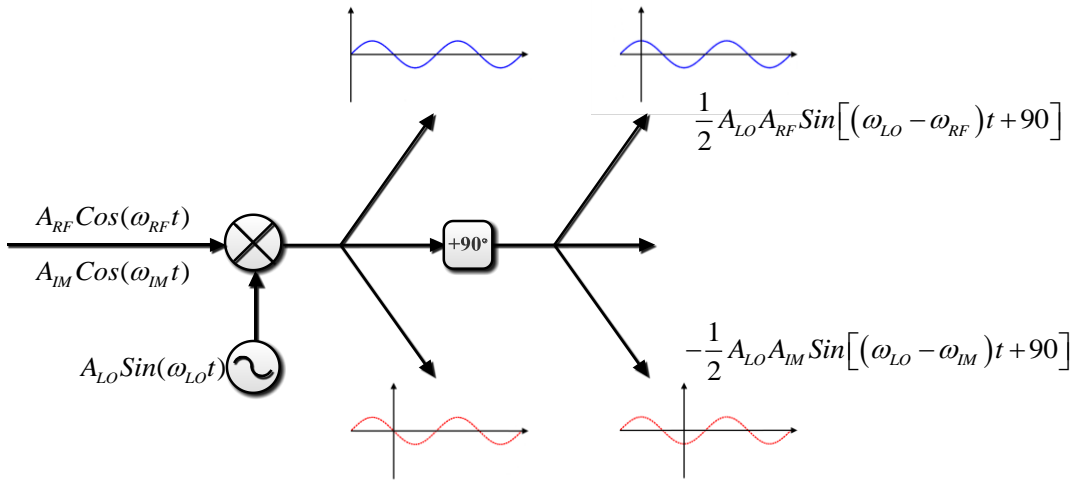


Figure 2.10: Mixing operation of image rejects receivers.

2.1.2 Homodyne Architectures

The Homodyne receiver, also called direct conversion or zero-IF receiver, is architecture that directly convert RF signal to base band ones [19, 20]. Figure 2.11 shows the block diagram of a homodyne receiver. In this receiver, first a pass band filter is employed to reject interferes and then, the RF signal is amplified by an LNA. As the conversion is in a single step, the carrier frequency is equal to LO frequency in mixing down process. In direct conversion there is no need to image rejection circuit as there is no image production. The remained interferers remained above and below the signal are eliminated by a low pass filter. As a result, this receiver is more promising for integrated circuits. Furthermore, it has lower power consumption as it has fewer blocks compared with heterodyne receivers.

However, there are some issues that limit the direct conversion applications. In fact, heterodyne receivers, despite their off-chip passive components, are more practical than homodyne receivers. Today, a lot of improvement in on-chip implementation of basic elements like spiral inductors with acceptable quality factor, symmetrical transformer and balun with high mutual inductance, and large MIM capacitance, make it possible to implementing the RF blocks in on-chip with smaller sizes. This significant improvement lead the RF signal receivers to be implemented based on heterodyne architecture. The main limitation factors of direct conversion receivers can be summarized as $1/f$ noise, DC offsets, I/Q mismatch, and even order distortion [21, 22].

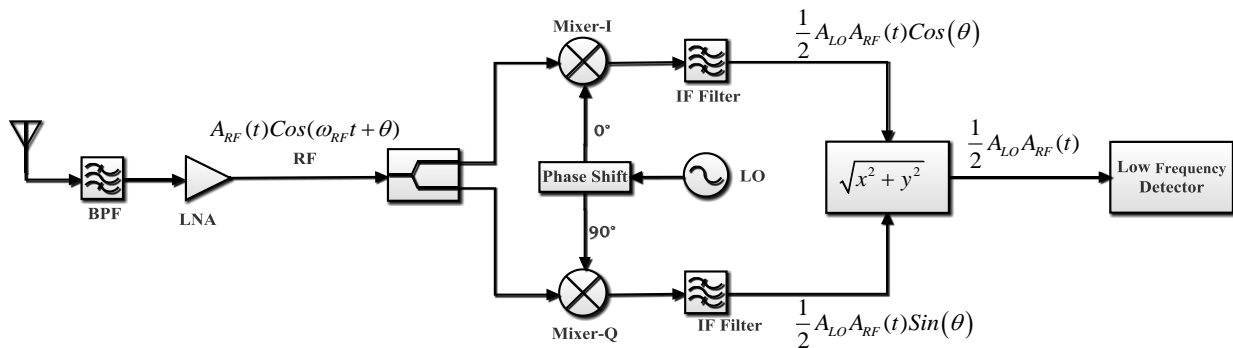
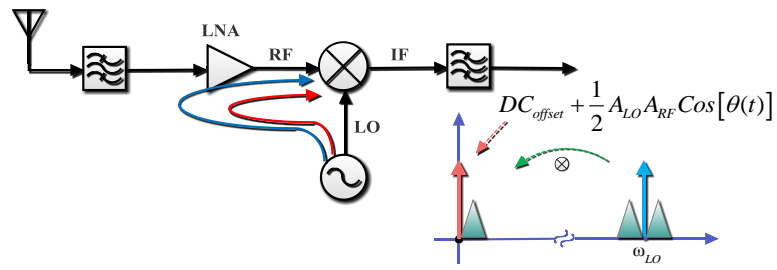
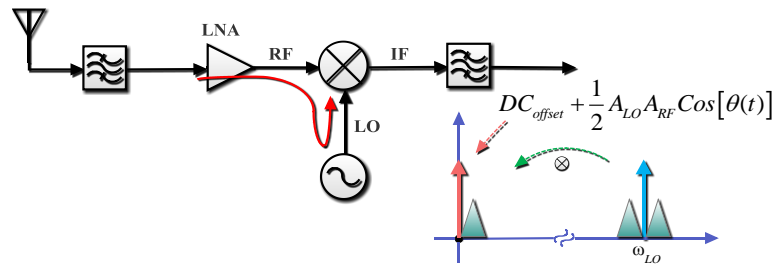


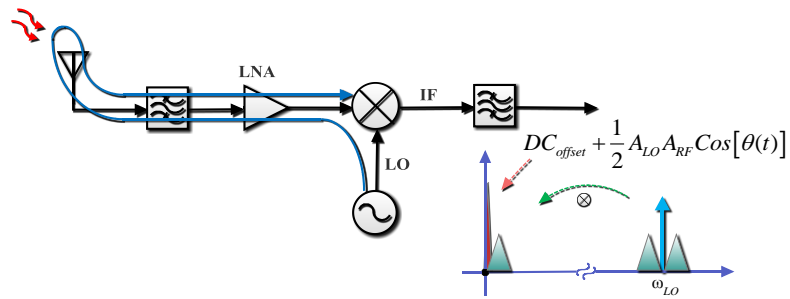
Figure 2.11: Block diagram of a homodyne receiver.



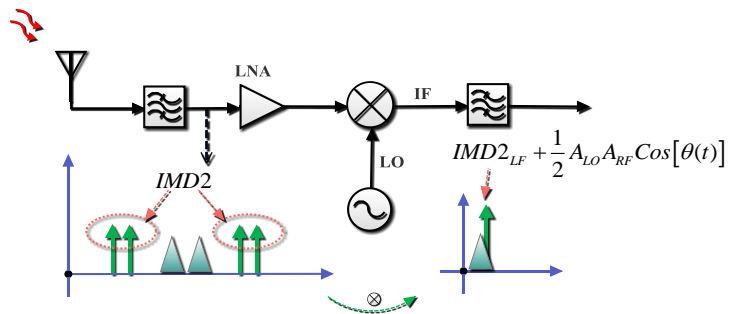
(a)



(b)



(c)



(d)

Figure 2.12: DC offset due to; (a) LO leakage, (b) strong interfere, (c) time-varying offset, (d) even order distortion in LNA

2.1.2.1 $1/f$ Noise

$1/f$ noise, also known as pink noise or flicker noise, originates from random charge carriers in low frequency devices that are intrinsically present in all devices. In homodyne receivers, $1/f$ noise of mixer is presented in the same spectra of the base band signal making the issue more severe. The gain of down converted signal is low after passing through the mixer, therefore, the flicker noise can significantly affect the signal to noise ratio (SNR). To suppress the effect of $1/f$ noise in homodyne receivers usually large devices are used.

2.1.2.2 DC offsets

DC offsets have the most destructive effects on direct conversion [23-26]. Zero frequency converted signal is very vulnerable to the large DC offsets which can be added to the desired signal due to LO leakage, strong interferers, time-varying offsets, and even order distortions in LNA. This amount of DC offsets can easily saturate some blocks which need an IF amplifier to provide the necessary input gain.

The finite isolation between the input and output of LNA, mixer, and LO can cause the leakage of signals to input of the LNA or mixer. DC offsets due to the LO leakage occur when parasitic coupling of LO signal and LNA (or mixer) input signal is self-mixed with the LO signal, as illustrated in Figure 2.12.a. Also, a strong interferer can leak from the RF input to the LO and cause self-mixing, as shown in Figure 2.12.b. Moreover, the LO signal can be coupled to the antenna and radiate in the air, reflect back to the RF input and mix with LO signal.

Figure 2.12.c depicts this phenomenon which is hard to be reduced as it has time-varying nature. A non-50% duty cycle local oscillators also have DC offsets in their outputs. The last issue that causes DC offset is LNA's even order distortion, as shown in Figure 2.12.d. Even order distortion, characterized by IIP2, appears when two interferers exist side by side at the input. As a result the different frequency will be at the LNA output, which can be directly fed through the mixer and cause signal corruption. To avoid such a problem, the LNA's IIP2 must be high as well as IIP3. Differential circuits also can reduce this phenomenon.

A possible solution to reducing DC offsets is AC coupling through a high pass filter. The required coupling capacitor for the filter is huge with very slow setting time and its implementation needs a large chip area. Another way of reducing DC offset is offset cancellation, usually employed in time division multiple access (TDMA) systems, as they have idle mode for the receiver. While the receiver is idle, the output DC voltage on the capacitor is accumulated, measured, and subtracted from the mixer output voltage. Two sets of mixers can alternatively result in offset cancellation. While one is receiving the signal, the other's offset is having cancelled.

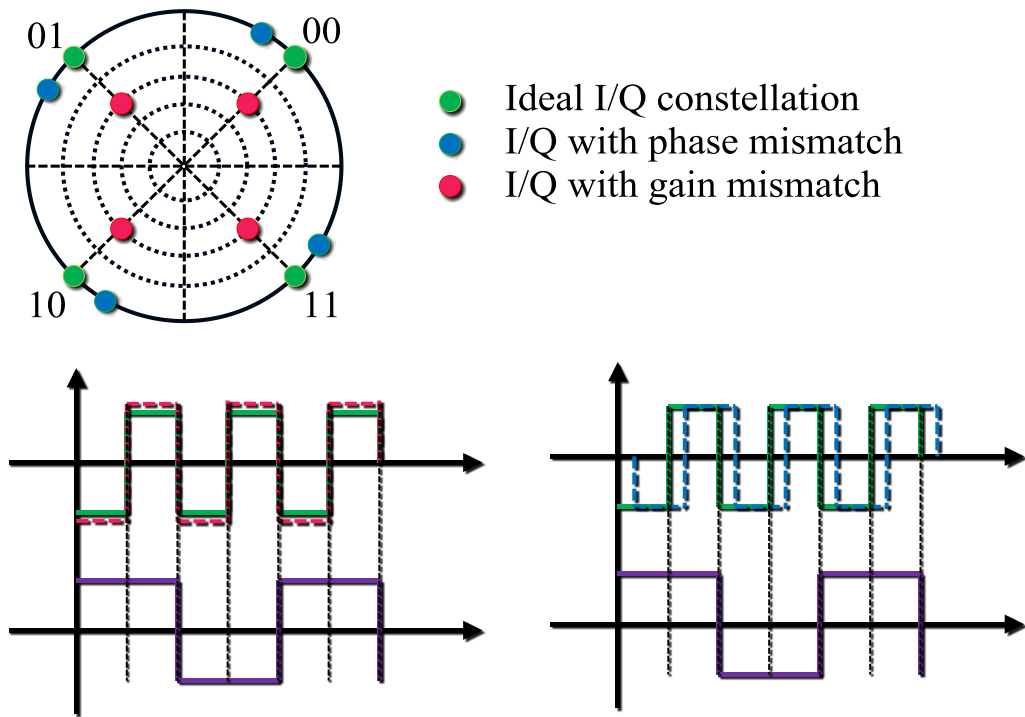


Figure 2.13: I/Q mismatch problem in a direct conversion receiver.

2.1.2.3 I/Q mismatch

As depicted in Figure 2.11 in double side band reception, in-phase (I) and quadrature (Q) phase channel conversion is needed. To avoid I/Q mismatch, the LO output in RF frequency must be in a 0° (I) and 90° (Q), as well as matching gain. If the quadrature phase difference is not satisfied, a portion of I (Q) signal will be presented in the Q (I) channel, which results in SNR

reduction. Thus, the phase mismatching is more challenging than gain mismatch. However, it can be compensated in a calibrating process with a known data. Figure 2.13 shows the I/Q mismatch problem. Furthermore, by utilizing variable IF gain amplifier for I/Q channels, the gain mismatch can be removed.

2.1.2.4 Even Order Distortion

In all real devices, non-linear behavior of the receivers causes intermodulation distortions of input signals of different tones. The high frequency terms of the output signal can be removed by an appropriate filter. However, if the input signals have frequencies close to each other, the intermodulation of their difference will be in the designed band. In a direct conversion having zero frequency center output, the DC components of the distortion result in DC offset in receivers output. Also, when the second harmonic of the RF signal is mixed with that of LO, an undesired distortion will be generated. Odd symmetry system can be a possible way to reduce even order harmonics. However, it comes with the cost of differential system implementation in RF frequencies. As an alternative way, digital signal processing (DSP) can be used to compensate this issue.

2.1.2.5 Homodyne Receiver Requirements

According to the previous subsections, a homodyne receiver needs the following requirements to work properly:

- Linear LNA (low second and third-order intercept point (IIP2 and IIP3))
- Linear mixer to reduce DC offset
- 50% duty cycle in LO
- Ultra low DC offsets
- Low flicker noise
- High isolation between input and output ports

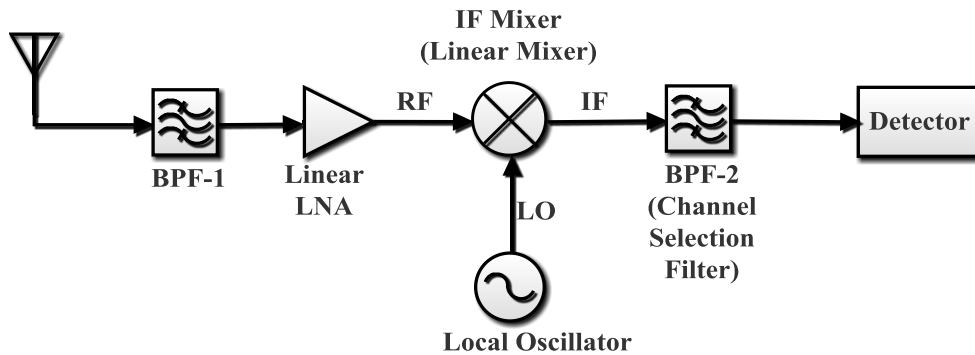


Figure 2.14: Block diagram of an ultra-low IF receiver.

2.1.3 Ultra Low IF Architectures

In systems that the adjacent channel signals are idle or sufficient guard bands are considered, we can choose LO and RF frequencies such that the image frequency coincides with unused spectrum. In low IF receivers the RF signal is mixed down to a low IF frequency, as depicted in Figure 2.14. As a result the channel selection can be applied by a low pass filter. In this architecture DC offset, $1/f$ noise, and LO leakage problem are eliminated as the frequency difference between LO and RF frequencies is small. However, image rejection issue limits this receiver's application [1, 27-29]. Hartley and Weaver image rejection circuits can be employed to attain image rejection about 35dB, which meets WBAN standards like IEEE 802.15.4 [29, 30]. Today, low power wireless receivers use the low IF topology to have low cost and efficient products.

2.2 IEEE 802.15 WBAN and MBAN

As a result of the growing of the elderly population and health care expenditure that is predicted to become triple by 2025, the healthcare systems are facing crisis which needs quick solutions [7]. One economical remedy is the remote health monitoring of the patient's vital signs and updating of the records at the real time via the internet. This process must be non-intrusive as well as ambulatory. This product, as a result, will be considered as a perfect alternative for the traditional monitoring in which body function records are separated by a significant time period

and can also lead to inaccurate diagnosis when they are monitored in a time that the vital signs are elevated from the normal condition, for example due to the instantaneous anxiety. This system also is important for emergency members and athletes. In order to monitoring body functions and movement, the required sensors and remote system must be lightweight and integrable into the clothing without restriction [31]. Wireless body area networks (WBAN), as a promising healthcare technology, can provide remote health monitoring with the above required features and support both medical and consumer electronics (CE) functions. Furthermore, a standard model for addressing these applications is established in the task group of IEEE 802.15.6 [31, 32].

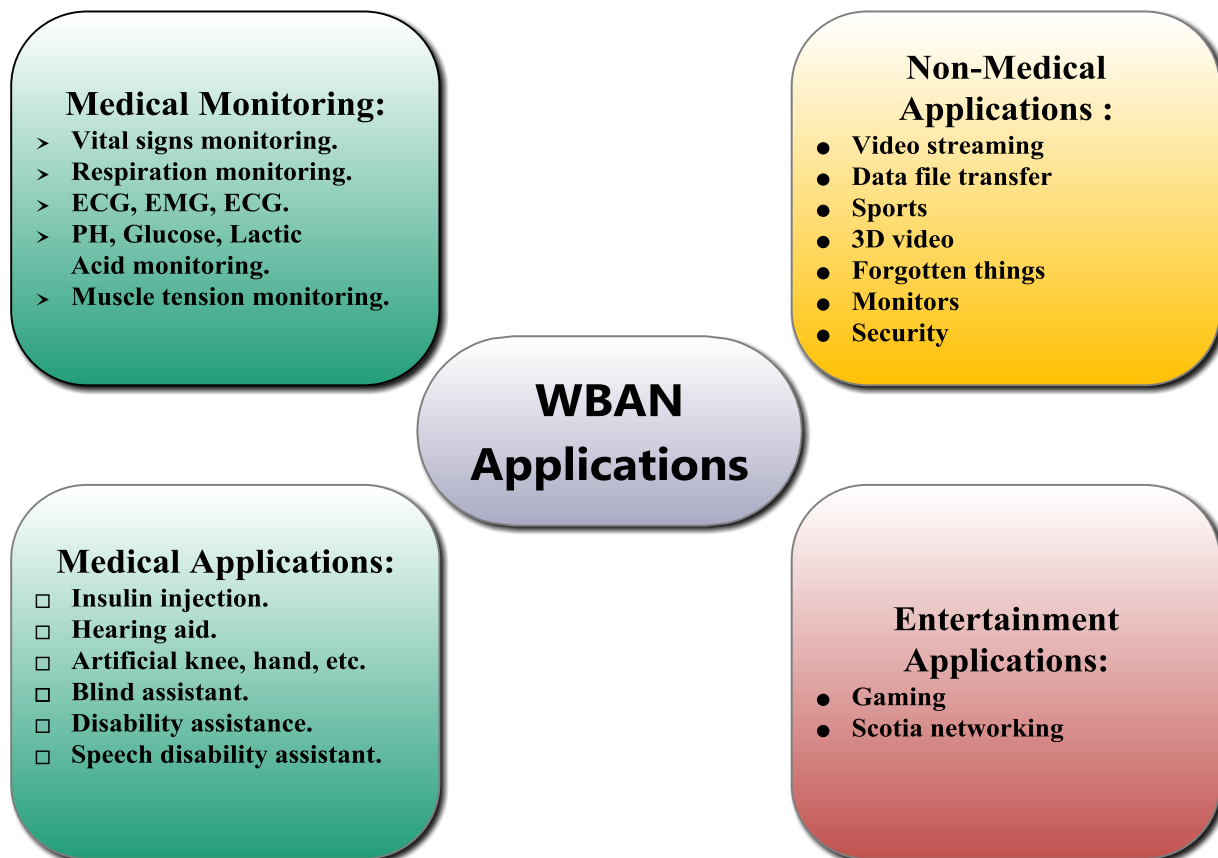
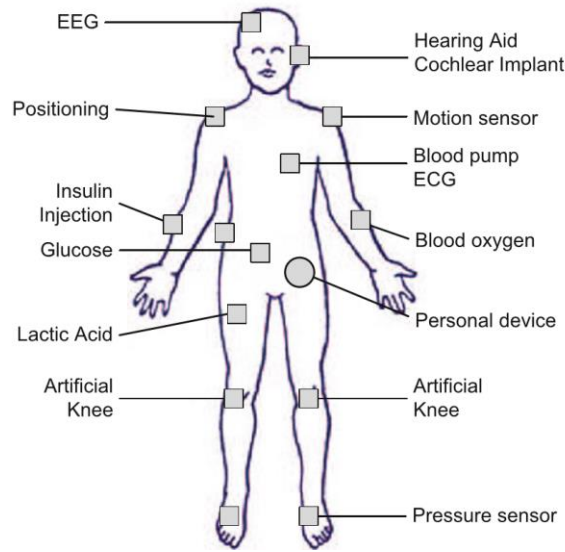
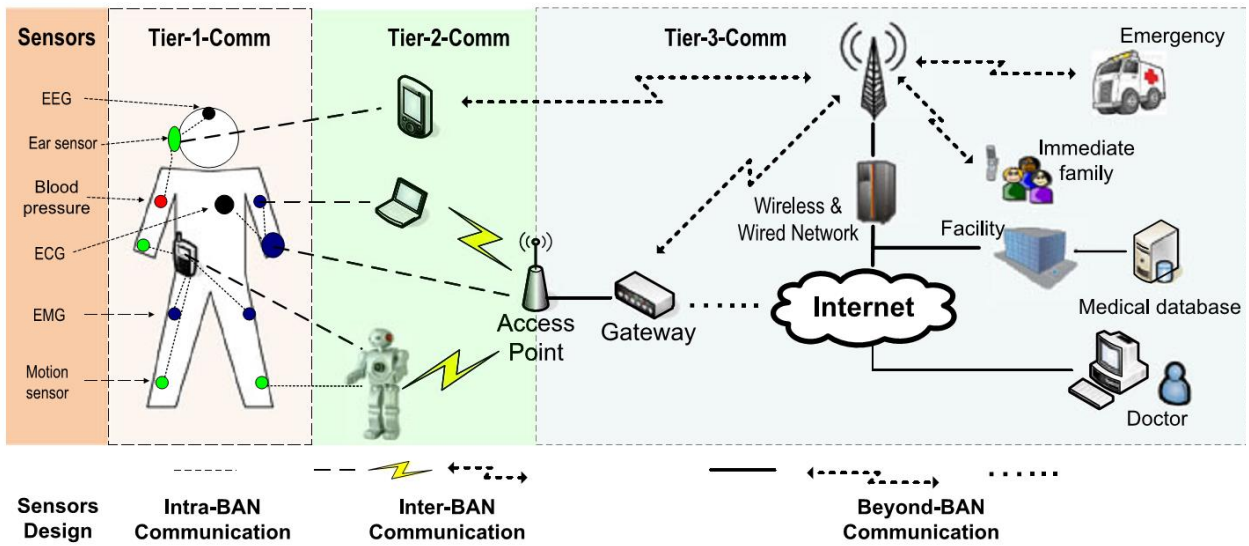


Figure 2.15: WBAN applications [31].



(a)



(b)

Figure 2.16: (a) Patient vital signs monitoring's sensors in WBAN [33], (b) A three-tier architecture based on a BAN communications system [34].

2.2.1 WBAN Applications

Long term health monitoring through WBAN which is smart, low power and miniaturized sensing in, on, and around the body, can be an affordable system for all diagnostic process, chronic condition control, surgical recovery procedure, and emergency event handling [7]. IEEE 802.15.6 standard for WBAN applications support medical and non-medical systems as depicted in Figure 2.15. In the medical applications, a continues records of the patient's vital signs are collected and sent to a monitoring station to be analyzed. These comprehensive information, then is applied to minimized of the myocardial infraction events and provide various disease treatment. Moreover, people with disabilities are helped using WBAN. On the other side, non-medical applications involve social networking, data file transferring, gaming, and forgotten things monitoring. For example, one can exchange business card or digital profile simple by shaking hand [31].

2.2.2 Network Architecture

WBAN applications include in-body and on-body area networks. Invasive/implanted device and the base station connections are supported by in-body area network, while, the non-invasive/wearable device and base station connections are included in on-body area network [7]. The WBAN health monitoring architecture is given in Figure 2.16.a, in which electroencephalography (EEG), electromyography (EMG), electrocardiogram (ECG), and motion and blood pressure sensors send the records to the adjacent personal server (PS) systems. These information then are sent to the medical station using a Bluetooth/WLAN connection for real time diagnosis, record keeping, or emergency alert. There are three components in a WBAN topology, as depicted in Figure 2.16.b [34]. Tire-1-Comm, Tier-2-Comm, and Tire-3-Comm designs support intra-WBAN, inter-WBAN, and beyond-WBAN communications.

2.2.3 Frequency Allocation

The physical (PHY) and medium access control (MAC) layers of WBAN standardization is defined in the IEEE 802.15.6 [31]. The frequency band selection (PHY) is based on available frequencies for the WBANs and is depended on the communication authority of each country, as

shown in Figure 2.17. In most of the countries, medical implant communications service (MICS), the implant communication licensed band, is in the identical frequency range of 402-405MHz. The licensed band for medical telemetry system is wireless medical telemetry services (WMTS), which like MICS bandwidth do not established for high rate applications. In the case of high data rate requirement, the industrial, scientific, and medical (ISM) band is defined, although, it's interference problem with IEEE 802.1and IEEE 802.15.4 may become challenging.

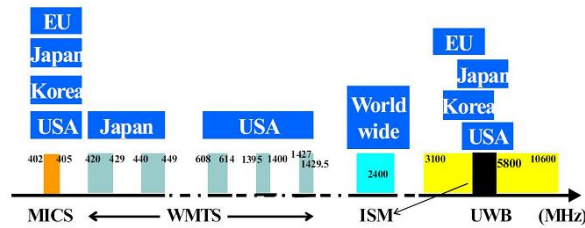


Figure 2.17: Frequency bands for WBAN [31].

On body wearable nodes as well as in-body implementation ones are licensed by narrow band (NB) PHY that operates through three aspects: radio transceiver activation/deactivation, clear channel assessment (CCA) in the current channel, and transmission/reception of data [35]. Table 2.1 shows 230 physical channels operating in seven standard bands. The transmission/reception of any WBAN device must be in one of the frequency bands mentioned in Table 2.1.

Table 2.1: Frequency allocation for NB-WBAN

Frequency Band (MHz)	402~405	420~450	863~570	902~928	950~958	2360~2400
Number of channels	10	12	14	60	16	79

Ultra wideband (UWB) PHY is designed to be more robust than WBAN and providing higher performance, lower complexity and lower power consumption. Impulse radio UWB (IR-

UWB) and wideband frequency modulation (FM-UWB) are two technologies of UWB [35]. 11 channels with numbers from 0 to 10 each having 499.2MHz bandwidth are defined for UWB. The channels are considered of two band group of low band and high band. Three channels of numbers 0~2 with center frequencies 3494.4MHz, 4492.8MHz are included in low band channels. The channel 1 is obligatory, while, the other are not. On the other hand, the eight channels of 3~10 with center frequencies of 6489.6MHz, 6988.8MHz, 7488.0MHz, 7987.2MHz, 8486.4MHz, 8985.6MHz, 9484.8 MHz, and 9984.0MHz are reserved for high band channels.

Human body communication (HBC), also named electric field communication (EFC), employs only digital circuits for its transmitter and uses only one electrode rather than an antenna [35]. Furthermore, as there is no RF module in implementation of the receiver, the devices are lightweight and have low power consumption.

2.3 Low Noise Amplifier (LNA)

Low noise amplifier (LNA), the first stage of most radio receivers system, mainly is used to minimize noise figure (NF) and amplifies the output signal of antenna. It must fulfill system, requirements, such as input matching, noise figure, linearity, and gain. Low DC power supply, low power dissipation, small area size, and costly efficiency are other parameters of interest [36, 37]. The requirements are expressed in more detail in following sections.

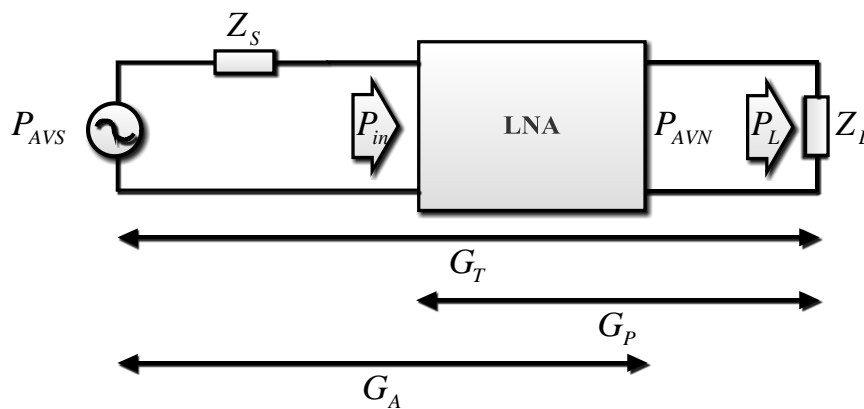


Figure 2.18: Power Gain.

2.3.1 LNA Gain

The ratio between the output and input signals is often defined as voltage gain, power gain, and conversion gain. The voltage gain, usually measured in logarithmic scale (dB), can be expressed as:

$$A_v = 20 \log \left(\frac{V_{out}}{V_{in}} \right) \quad 2.2$$

where V_{in} and V_{out} represent the amplitude of input and output signals, respectively. Power gain, as illustrated in Figure 2.18, is defined by three definitions, using in RF application [1]:

$$\text{Transducer gain} = G_T = \frac{P_L}{P_{in}} \quad 2.3$$

$$\text{Operating gain} = G_p = \frac{P_L}{P_{Avs}} \quad 2.4$$

$$\text{Available gain} = G_A = \frac{P_{Avn}}{P_{Avs}} \quad 2.5$$

where, P_{Avs} , P_{in} , P_{Avn} , and P_L present the power available from source, delivered power to the input, available power from network, and delivered power to the load, respectively. Also, the ratio between the IF power at the mixer output and the RF receiver input is known as conversion gain:

$$\text{Conversion gain} = G_C = \frac{P_{out,mix}}{P_{in,mix}} \quad 2.6$$

2.3.2 Noise Sources

All interference signals rather than desired signal can be a source of noise. Among the numerous type of noise, one known as fundamental noise, is the most challenging issue and hard to be suppressed. Despite the random nature of these noises, they still follow statistical rules. Thermal noise and quantum noise are the most important fundamental noises.

2.3.2.1 Thermal Noise

The conductor's temperature and electrical resistance are the main factor in determining the noise properties [38, 39]. The thermal noise of a resistor can be modeled as shown in Figure 2.19. $\overline{v_n^2}$ and $\overline{i_n^2}$ are defined through thermal equilibriums as bellow:

$$\overline{v_n^2} = S_{v_n} \Delta f = 4kT \Delta f R \quad 2.7$$

$$\overline{i_n^2} = S_{i_n} \Delta f = \frac{4kT \Delta f}{R} \quad 2.8$$

where k , T , Δf , and R are representing Boltzmann's constant, absolute temperature, noise band width, and conductor's resistance, respectively. Keeping the temperature low, the thermal noise can be reduced in the resistance.

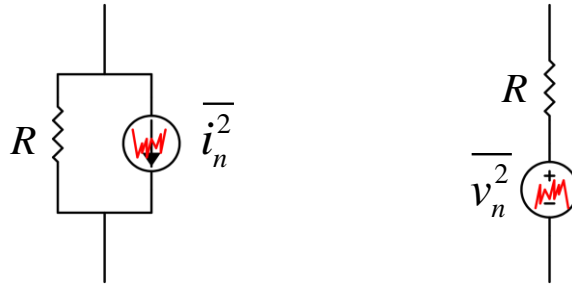


Figure 2.19: Equivalent model of a resistor thermal noise.

2.3.2.2 Drain Current Noise

Drain current noise can be contributed to the substrate resistance of FETs, as they are in the triode region. It can be expressed as [40]:

$$\overline{i_{nd}^2} = 4kT \gamma g_{d0} \Delta f \quad 2.9$$

where γ , which is process dependence variable, is one at zero drain-source voltage (V_{DS}) and equals to $2/3$ at saturation region for a long-channel transistor. g_{d0} represents the drain-source conductance at zero V_{DS} . The other important thermal noise source is presented by

substrate resistance (R_{sub}). Figure 2.20 shows the manner in which substrate resistance noise emerges at the device terminals. However, this noise source is not effective at RF frequency. Beyond the pole frequency of gate-body capacitor (C_{gb}) and substrate resistance (R_{sub}), the drain current noise due to substrate resistance ($\overline{i_{nd,sub}^2}$) could be ignored, as can be inferred from noise frequency dependent expression [41]:

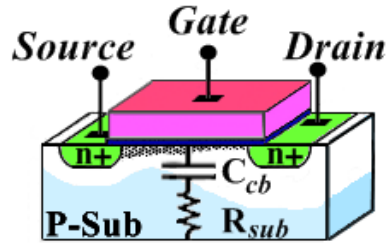


Figure 2.20: Equivalent model of a substrate resistance.

$$\overline{i_{nd,sub}^2} = \frac{4kT R_{sub} g_{mb}^2}{1 + (\omega R_{sub} C_{gb})^2} \Delta f \quad 2.10$$

where g_{mb} is the back gate transconductance due to the body effects.

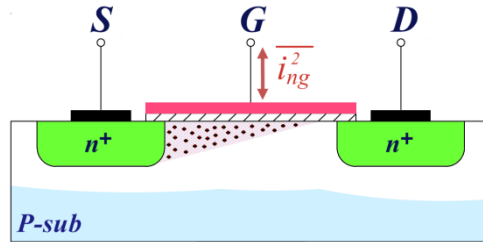


Figure 2.21: Induced gate noise and channel fluctuation.

2.3.2.3 Induced Gate Current Noise

The high capacitive coupling between the channel and gate at high frequency causes noise flow to the gate. Also, a thermal noise is generated as result of resistive material between

the gate and channel. This phenomena is known as channel fluctuation noise as well [41-43]. The induced gate noise is shown in Figure 2.21. The spectral density of this noise described as:

$$\overline{i_{ng}^2} = 4kT \delta g_g \Delta f \quad 2.11$$

$$g_g = \frac{\omega^2 C_{gs}^2}{5g_{d0}} \quad 2.12$$

where δ is the process dependence variable and equals to $4/3$ for long channel devices, which is twist the value of γ . To extend and apply this expression for the short channel devices, it is reasonable to keep this ration. Therefore, as γ typically is between 1 and 2 for the short channel, δ would be between 2 to 4 [44-46]. The gate induced noise is categorized as a blue noise rather than white noise as it increase with ω . Furthermore, according to the above expression, this noise is negligible at low frequencies; while at radio frequencies become dominate.

2.3.3 Noise Factor (F) and Noise Figure (NF)

The noise performance if a circuit can be expressed by its noise factor or noise figure. By defining the signal to noise ratio (SNR) as:

$$SNR = \frac{\text{Power of Signal}}{\text{Power of Nosie}} \quad 2.13$$

The noise factor and noise figure can be attained by Eq.2.14 and Eq.2.15, respectively.

$$F = \frac{SNR_{in}}{SNR_{out}} \quad 2.14$$

$$NF = 10\log(F) \quad 2.15$$

The total noise factor of a multi series cascaded stage circuit can be described by Friis' formula as [1]:

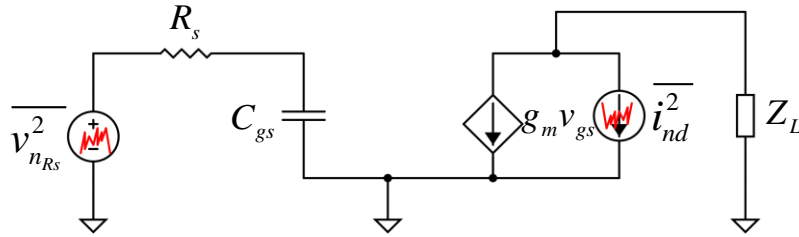


Figure 2.22: Noise sources in typical CS LNA.

$$F_{total} = F_1 + \frac{F_2 - 1}{G_1} + \frac{F_3 - 1}{G_1 G_2} + \dots = F_1 + \sum_{i=1}^n \frac{F_i - 1}{\prod_{j=1}^{i-1} G_j} \quad 2.16$$

where G_i is the power gain (linear, not in dB) of the i -th stage. Since, LNA is usually the first stage in a communication system, for a receiver this expression can be written as:

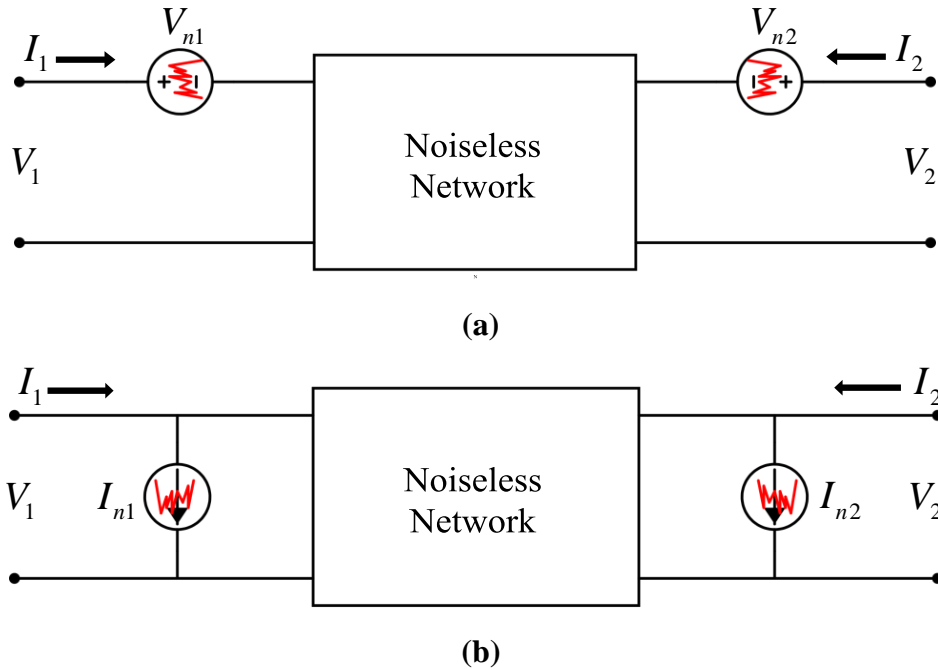


Figure 2.23: Two-port noiseless network representation; (a) Z- parameters, (b) Y- parameters.

$$F_{receiver} = F_{LNA} + \frac{F_{rest} - 1}{G_{LNA}} \quad 2.17$$

The Eq.2.17 indicates the key role of the LNA, as its noise factor directly contributed to the total noise and the rest stages' noise factor are reduced by its gain. Figure 2.22 depicts a typical common source (CS) LNA noise source, in which, $\overline{v_{nr_s}^2}$ is contributed by the real part of signal source impedance while $\overline{i_{nd}^2}$ represent the thermal noise of the transistor.

To avoid a complex analysis of a transistor's equivalent noise circuit, one can consider the two-port network model in which the circuit is assumed to be noiseless and the internal noises are modeled by external noise sources at the either input or output terminals of the network. As a result, the voltage-current relationship of the network can be represented by its Z- or Y-parameters, as depicted by Figure 2.23. Thus, the equivalent noise source can be measured by the open circuit (O.S) and short circuit tests (S.C), which result the Z- and Y-parameters, respectively.

$$\text{For Z-parameters} \quad \begin{cases} V_1 = Z_{11}I_1 + Z_{12}I_2 + V_{n1} \\ V_2 = Z_{21}I_1 + Z_{22}I_2 + V_{n2} \end{cases} \quad 2.18$$

$$\text{For Y-parameters} \quad \begin{cases} I_1 = Y_{11}V_1 + Y_{12}V_2 + I_{n1} \\ I_2 = Y_{21}V_1 + Y_{22}V_2 + I_{n2} \end{cases} \quad 2.19$$

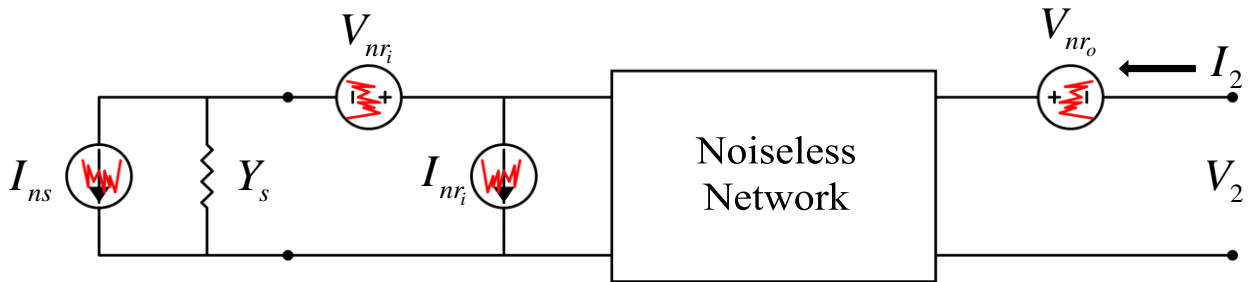


Figure 2.24: Equivalent noise model for noise factor calculation.

If all noise sources are referred to the input port, the noise factor was defined in Eq. 2.14 would be rewritten as the total output noise power which is proportional to the mean square

value of the short circuit current and the output noise power due to the input noise source (Figure 2.24).

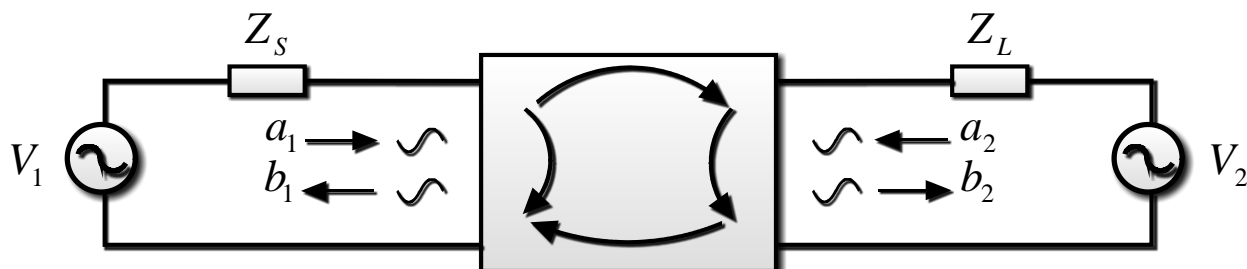


Figure 2.25: S-parameter representation of Two-port noiseless network.

2.3.4 S-Parameter

As mentioned before, it is common to model LNA circuits with two-port network to determine feature such as gain, noise, and linearity. The LNA can be characterized by its S -parameters, which can describe the impedance matching of the circuit. Traveling waves on transmission lines of the terminals are related to each other through the scattering (S) matrix. In this method, the input and output signal waves will be as depicted in Figure 2.25 and can be expressed as:

$$\begin{cases} b_1 = S_{11}a_1 + S_{12}a_2 \\ b_2 = S_{21}a_1 + S_{22}a_2 \end{cases} \quad 2.20$$

where a_1 and a_2 are the powers incident at the input and reflected from the load, respectively. The b_1 and b_2 represent the powers which are reflected from the input port of two pole network to the source and the output port to the load, respectively. The relation between incident and reflection waves and voltage-current at the ports of network can be expressed as [47]:

$$a_1 = \frac{V_1 + I_1 Z_o}{2\sqrt{Z_o}} \quad 2.21$$

$$a_2 = \frac{V_2 + I_2 Z_s}{2\sqrt{Z_s}} \quad 2.22$$

$$b_1 = \frac{V_1 - I_1 Z_o}{2\sqrt{Z_o}} \quad 2.23$$

$$b_2 = \frac{V_2 - I_2 Z_s}{2\sqrt{Z_s}} \quad 2.24$$

The S_{11} and S_{21} are determined at the output port when it is terminated to matching load, i.e. $Z_L = Z_o$, where Z_o represents the characteristic impedance. As a result, there will be no reflection ($a_2 = 0$) and we have:

$$\left\{ \begin{array}{l} S_{11} = \frac{b_1}{a_1} \Big|_{a_2=0} \\ S_{21} = \frac{b_2}{a_1} \Big|_{a_2=0} \end{array} \right. \quad 2.25$$

In a same manner, the S_{12} and S_{22} can be measure at the input terminal when the source impedance is matched, $Z_s = Z_o$, and we obtain:

$$\left\{ \begin{array}{l} S_{12} = \frac{b_1}{a_2} \Big|_{a_1=0} \\ S_{22} = \frac{b_2}{a_2} \Big|_{a_1=0} \end{array} \right. \quad 2.26$$

In the LNA design, the input impedance must be matched with antenna impedance that usually equals to 50Ω . The forward and revers voltage gain is represented by S_{21} and S_{12} , respectively, S_{11} and S_{22} are input and output voltage reflection coefficient, respectively.

2.3.4.1 Matching

Based on the circuit theories, to achieve the maximum power, voltage, or current transferred in multi stage circuits, the load impedance must be appropriately designed. If the source or load impedance are not matched with the transmission line characteristic impedance, they will cause discontinuities in the propagation that result in reflection of a portion of the incident signal wave. The ratio of the reflected wave to the incident wave known as reflection coefficient and for the input and output can be expressed in terms of S-parameters as follow:

$$\Gamma_{in} = \frac{b_1}{a_1} = S_{11} + \frac{S_{12}S_{21}\Gamma_L}{1 - S_{22}\Gamma_L} \quad 2.27$$

$$\Gamma_{out} = \frac{b_2}{a_2} = S_{22} + \frac{S_{12}S_{21}\Gamma_S}{1 - S_{11}\Gamma_S} \quad 2.28$$

where

$$\Gamma_L = \frac{Z_S - Z_o}{Z_S + Z_o} \quad 2.29$$

$$\Gamma_S = \frac{Z_L - Z_o}{Z_L + Z_o} \quad 2.30$$

2.3.4.2 LNA gain in terms of S-parameters

The amplifier maximum power transferred is attained when input and output are complex conjugate matched, which means $\Gamma_L = \Gamma_S^*$ and $\Gamma_{out} = \Gamma_{in}^*$. The voltage gain, the ratio of the output voltage to the input voltage, can be written as [48]:

$$A_v = \frac{V_2}{V_1} = \frac{S_{21}(1 + \Gamma_L)}{(1 - S_{22}\Gamma_L)(1 + \Gamma_{in})} \quad 2.31$$

Furthermore, the transducer gain, the ratio of the load delivered power to the source available power, will be:

$$G_T = \frac{P_L}{P_{Avs}} \quad 2.32$$

where

$$P_L = |b_2|^2 (1 - |\Gamma_L|^2) \quad 2.33$$

2.3.5 Nonlinearity and large signal behavior

Active elements distortion causes nonlinearities in a RF system. Therefore, in an LNA, large input signals can change the dynamic operation point. Even in the case of small signal, interferers may appear in the LNA input and increase the level of the operation point. According to the Tailors' expansion, a nonlinear system output can be expressed by:

$$y = a_0 + a_1x^1 + a_2x^2 + \dots = \sum_{i=1}^n a_i x^i \quad 2.34$$

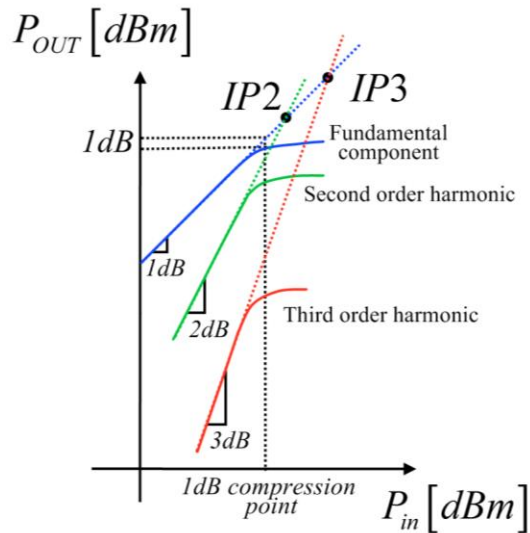


Figure 2.26: Second and third intercept point.

where n represents the nonlinearity degree of a system. In the real world, the number of term in Eq. 2.34 is infinity, however due to limitation of calculation; the polynomial is limited to the first

three ones. For a sinusoidal input signal of amplitude A and frequency f_i , this polynomial results in harmonic distortion of the input [36]:

$$y \approx a_0 + \frac{a_1 A}{2} \sin(2\pi f_i) + \frac{a_2 A^2}{4} \sin(2\pi f_i) + \frac{a_3 A^3}{8} \sin(3\pi f_i) \quad 2.35$$

Figure 2.26 depicts these harmonics as a function of the input and output power. The slope of fundamental frequency, second and third order harmonics equal to one, two, and three, respectively. Due to nonlinearity and loss, these slopes are saturated, however, the intersections of the extra plotted slopes between fundamental and second or third harmonic determine as intercept point two (IP2) or three (IP3), respectively. Another challenging issue in LNA design is the intermodulation distortion (IMD) occur when two signals with same amplitude and small frequency separation is presented at the input of nonlinear system, as shown in Figure 2.27. By f_1 and f_2 representing the input signal frequencies, second order harmonics at $2f_1$ and $2f_2$ and third order harmonics at $3f_1$ and $3f_2$ will be produced. Furthermore, second order intermodulation (IM2) at $f_1 + f_2$ and $f_1 - f_2$ as well as third order intermodulation (IM3) at $2f_1 - f_2$ and $2f_2 - f_1$ are generated. Considering these intermodulation terms that falls in desired band, it's hard to reduce them by filtering.

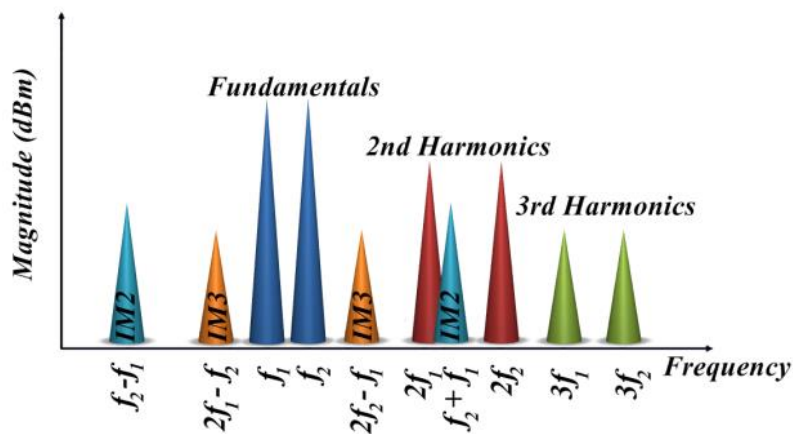


Figure 2.27: Fundamental and higher order products of a nonlinear system.

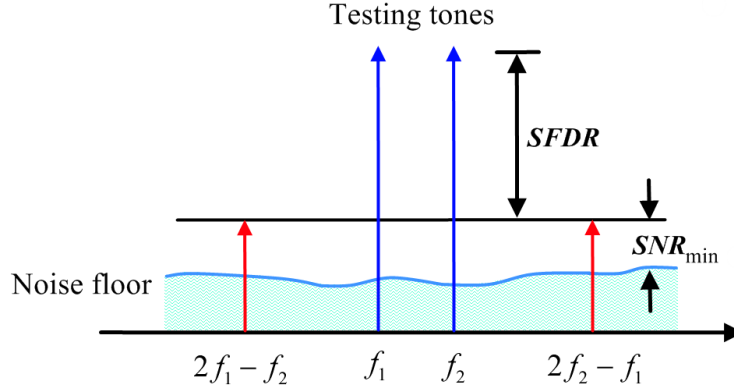


Figure 2.28: The Spurious Free Dynamic Range (SFDR) demonstration.

To measure the effects of intermodulation, 1-dB compression point (P_{1-dB}) is defined as the point where there is 1dB reduction in fundamental signal at a certain frequency. As a result, it can be approximated in terms of Taylor expression as [1]:

$$P_{1-dB} = \sqrt{0.145 \frac{a_1}{a_3}} \quad 2.36$$

Moreover, the input-referred IP3 (IIP3) and output-referred IP3 (OIP3) is calculated by:

$$IIP3 = \sqrt{\frac{4 a_1}{3 a_3}} \quad 2.37$$

$$OIP3 = IIP3 + Gain(dB) \quad 2.38$$

Having OIP3 and gain value (G) of each stage of a cascade system, the total OIP3 can be calculated as:

$$\begin{aligned} \frac{1}{OIP3_{tot}} &= \frac{1}{OIP3_1 \cdot G_2 \cdot G_3 \cdot \dots \cdot G_n} + \frac{1}{OIP3_2 \cdot G_3 \cdot G_4 \cdot \dots \cdot G_n} + \dots + \frac{1}{OIP3_{n-1} G_n} + \frac{1}{OIP3_n} \\ &= \frac{1}{OIP3_n} + \sum_{i=1}^{n-1} \frac{1}{OIP3_i \prod_{j=i+1}^{n-1} G_j} \end{aligned} \quad 2.39$$

The total IIP3 is resulted by applying above results and total gain of system to the Eq. 2.38. The maximum to minimum input levels ratio that circuit still operates reasonable determines dynamic

range. With spurious free dynamic range (SFDR) definition, as depicted in Figure 2.28, we obtain:

$$SFDR = \frac{2}{3} \left[IIP3 - NF - BNL - 10 \log(BW) \right] - SNR_{\min} \quad 2.40$$

where BW , SNR_{\min} , and BNL represent the band width of system, the minimum SNR for a desired signal quality, and background noise level, respectively. The BNL at the input equals to -174 dBm/Hz . The other expression for dynamic range is compression-free dynamic range (CFDR) that is defined as the difference between the inputs referred 1-dB compression point and noise floor (N_{floor}), in dB.

$$CFDR = P_{1\text{-dB}} - N_{\text{floor}} \quad 2.41$$

where N_{floor} is expressed as:

$$N_{\text{floor}} = NF - BNL - 10 \log(BW) \quad 2.42$$

2.4 Optimization Techniques

In designing LNA, there are many tradeoffs between gain, NF , linearity, impedance matching, and power consumption. To attain simultaneous noise and input matching ($SNIM$), several techniques are investigated such as: classical noise matching (CNM) [2], $SNIM$ [3], power constrained noise optimization ($PCNO$) [4], and power-constrained simultaneous noise and input matching ($PCSNIM$) [5, 6, 49] techniques. In the following discussion, we will report these four LNA design optimization techniques in more details.

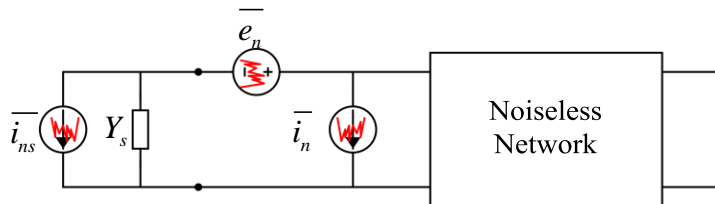


Figure 2.29: Equivalent input referred noise model for 2 pole network.

2.4.1 Classical Noise Matching (CNM)

First, to simplify analysis of noise in two port network introduced in section 2.3.3, we put all of the noise sources in the input of the noiseless network, as shown in Figure 2.29. However, there is a problem in combining noise sources correlated with each other with varying degrees. In the case of zero correlation between the noise powers of the source and that of the ports, the noise figure will be as:

$$F = \frac{\overline{i_{ns}^2} + \overline{|i_n + Y_s v_n|^2}}{\overline{i_{ns}^2}} \quad 2.43$$

However, there are some limitations in the classical theory. First, power consumption is not optimized in this method. Besides, the device size for a minimum noise figure is not considered. According to the MOSFET noise model, the mean square drain and gate current noise were written in Eq. 2.9 and Eq. 2.11, respectively. The gate noise is correlated with the drain noise by correlation coefficient:

$$c = \frac{\overline{i_{ng} \cdot i_{nd}^*}}{\sqrt{\overline{i_{ng}^2} \overline{i_{nd}^2}}} \quad 2.44$$

which its long-channel value is theoretically $-j0.395$ [44, 45]. To simplify the analysis, the thermal noise due to the resistive gate is neglected. The output noise at short-circuit noise input port represents the equivalent input noise voltage by reflecting the drain current noise back to the input. By neglecting channel-length modulation and assuming the ratio between the drain current noise and its reflected value to the input as voltage noise to be g_m , we will attain:

$$\overline{v_n^2} = \frac{\overline{i_{nd}^2}}{g_m^2} = \frac{4kT \gamma g_{d0} \Delta f}{g_m^2} \quad 2.45$$

Under open circuit condition, the value of the equivalent input current noise will be:

$$\overline{i_{n1}^2} = \frac{\overline{i_{nd}^2} (j\omega C_{gs})^2}{g_m^2} = \frac{4kT \gamma g_{d0} \Delta f (j\omega C_{gs})^2}{g_m^2} \quad 2.46$$

and substituting Eq. 2.45 in Eq. 2.46:

$$\overline{i_{n1}^2} = \overline{v_n^2} (j\omega C_{gs})^2 \quad 2.47$$

Thus, the sum of the reflected drain noise and the induced gate current noise built the total input current noise. In Eq. 2.47, the two ports can be correlated with each other, therefore, we can assume i_n to be the sum of two components, i_c that is correlated with v_n , and i_u that is uncorrelated with v_n .

$$i_n = i_c + i_u \quad 2.48$$

i_c correlation with v_n will be through the admittance Y_c as:

$$i_c = Y_c v_n \quad 2.49$$

Applying Eq. 2.48 and Eq. 2.49 in Eq. 2.43 results in:

$$F = \frac{\overline{i_{ns}^2} + \overline{|i_u + (Y_c + Y_s)v_n|^2}}{\overline{i_{ns}^2}} = 1 + \frac{\overline{i_u^2} + |(Y_c + Y_s)|^2 \overline{v_n^2}}{\overline{i_{ns}^2}} \quad 2.50$$

The equivalent noise resistance/conductance of above three independent noise sources are:

$$R_n = \frac{\overline{v_n^2}}{4kT\Delta f} \quad 2.51$$

$$G_u = \frac{\overline{i_u^2}}{4kT\Delta f} \quad 2.52$$

$$G_{ns} = \frac{\overline{i_{ns}^2}}{4kT\Delta f} \quad 2.53$$

therefore the noise factor can be written as:

$$F = 1 + \frac{G_u + |(Y_c + Y_s)|^2 R_n}{G_s} = 1 + \frac{G_u + |(G_c + G_s) + j(B_c + B_s)|^2 R_u}{G_s} \quad 2.54$$

By taking derivative of Eq. 2.54 with respects to the source admittance and setting it equals to zero, the general condition for optimizing the noise factor is obtained as [41]:

$$B_{opt} = B_s = -B_c \quad 2.55$$

$$G_{opt} = G_s = \sqrt{\frac{G_u}{R_u} + G_c^2} \quad 2.56$$

$$F_{min} = 1 + 2R_u [G_{opt} + G_c] = 1 + 2R_u \left[\sqrt{\frac{G_u}{R_u} + G_c^2} + G_c \right] \quad 2.57$$

Assuming the induced gate noise current to have correlated, i_{ng_c} , and uncorrelated, i_{ng_u} , components with the drain current noise, the correlation admittance will be obtained as:

$$Y_c = \frac{i_{n1} + i_{ng_c}}{v_n} = j\omega C_{gs} \left(1 - \alpha |c| \sqrt{\frac{\delta}{5\gamma}} \right) \quad 2.58$$

where:

$$\alpha = \frac{g_m}{g_{d0}} \quad 2.59$$

The optimal condition for minimum noise figure will be as:

$$B_{opt} = B_s = -j\omega C_{gs} \left(1 - \alpha |c| \sqrt{\frac{\delta}{5\gamma}} \right) \quad 2.60$$

$$G_{opt} = \sqrt{\frac{G_u}{R_u} + G_c^2} = \alpha \omega C_{gs} \sqrt{\frac{\delta}{5\gamma} (1 - |c|^2)} \quad 2.61$$

And finally, the minimum noise figure is approximated as:

$$F_{min} = 1 + 2R_u [G_{opt} + G_c] \approx 1 + \frac{2}{\sqrt{5}} \frac{\omega}{\omega_T} \sqrt{\gamma \delta (1 - |c|^2)} \quad 2.62$$

The above approximation is exact in the case of regarding ω_T as ratio of g_m to C_{gs} .

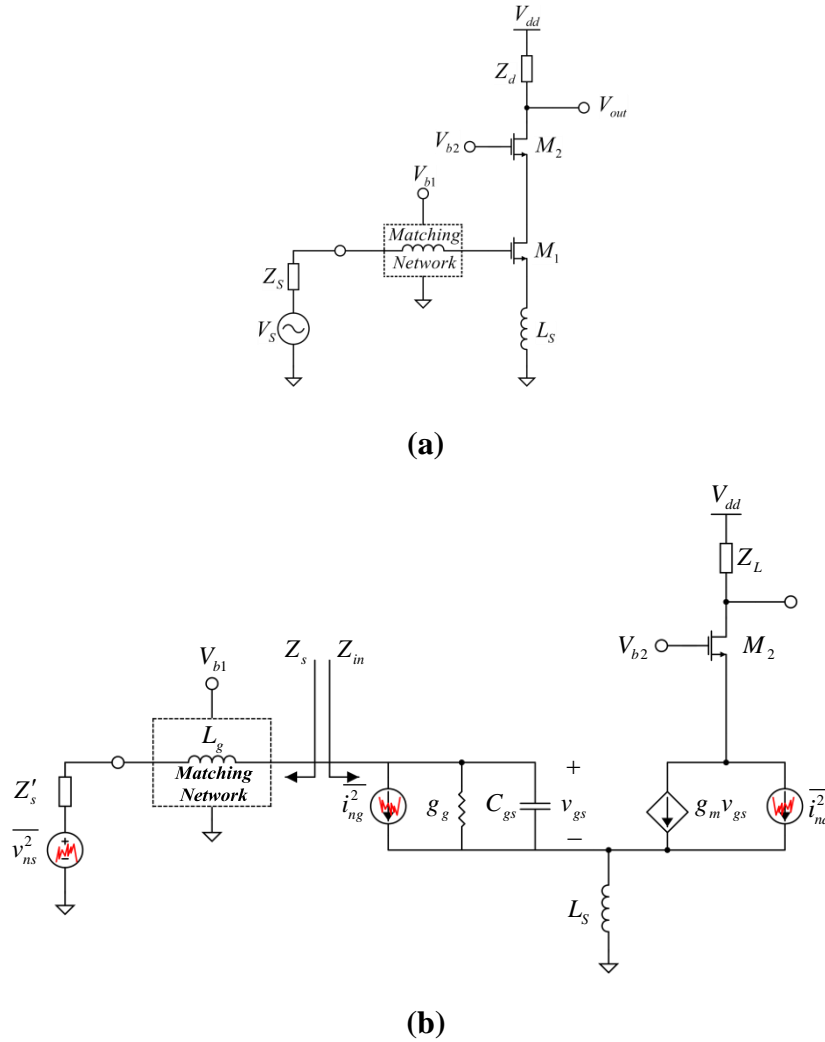


Figure 2.30: SNIM optimization technique [3, 49].

2.4.2 Simultaneous Noise and Input Matching (SNIM)

Shifting the optimum noise impedance Z_{opt} to desired value can be achieved through feedback techniques [50-53]. Figure 2.30 depicts the cascade LNA including inductive source degeneration and its small-signal equivalent circuit. A series inductor L_g is applied as matching

network and $Z'_s = R_s$. Adopting a similar procedure leads to the noise factor and noise parameters as [54, 55]:

$$R_n = \frac{\gamma}{\alpha g_m} \quad 2.63$$

$$Z_{opt} = \frac{\alpha \sqrt{\frac{\delta}{5\gamma}} (1 - |c|^2) + j \left(1 + \alpha |c| \sqrt{\frac{\delta}{5\gamma}} \right)}{\omega C_{gs} \left[\frac{\alpha^2 \delta}{5\gamma} (1 - |c|^2) + \left(1 + \alpha |c| \sqrt{\frac{\delta}{5\gamma}} \right)^2 \right]} - sL_s \quad 2.64$$

$$F_{min} = 1 + \frac{2}{\sqrt{5}} \frac{\omega}{\omega_T} \sqrt{\gamma \delta (1 - |c|^2)} \quad 2.65$$

As can be seen from the above equations, R_n and F_{min} are not changed while there is a shift in Z_{opt} . Furthermore, the input impedance of Z_{in} can be written as:

$$Z_{in} = sL_s + \frac{1}{sC_{gs}} + \frac{g_m L_s}{C_{gs}} \quad 2.66$$

As a result, although Z_{in} without degeneration does not have any real part, the source degeneration adds real part into the input impedance. In addition, its imaginary part is shifted by sL_s . Eq. 2.66 also can be written in the form of:

$$Z_{opt} = \frac{\alpha \sqrt{\frac{\delta}{5\gamma}} (1 - |c|^2)}{\omega C_{gs} \left[\frac{\alpha^2 \delta}{5\gamma} (1 - |c|^2) + \left(1 + \alpha |c| \sqrt{\frac{\delta}{5\gamma}} \right)^2 \right]} - sL_s - m \frac{1}{sC_{gs}} \quad 2.67$$

For a long-channel MOSFET, m is near 0.6, while with technology scaling it must be closer to 1. To apply SNIM, following condition must be satisfied:

$$Z_{opt} = Z_{in}^* \quad 2.68$$

which leads to:

$$\Re\{Z_{in}\} = \Re\{Z_s\} \quad 2.69$$

$$\Re\{Z_{opt}\} = \Re\{Z_s\} \quad 2.70$$

$$\Im\{Z_{in}\} = -\Im\{Z_s\} \quad 2.71$$

$$\Im\{Z_{opt}\} = \Im\{Z_s\} \quad 2.72$$

As Eq. 2.71 and Eq. 2.72 are the same, we can drop Eq. 2.72. In fact, the input mismatching slightly affects the LNA operation, however, Z_{opt} directly changes the noise figure. For a given value of Z_s , the transistor size (C_{gs}) can be determined by following Eq. 2.64, 2.66, and 2.70. The value of degeneration inductor L_s can be found through Eq. 2.72. finally, having C_{gs} and L_s , the value of V_{gs} is obtained by Eq. 2.69.

The SNIM technique allows any value of Z_s by changing L_s value. However, there is a limitation in optimization for small size transistor where cause a confliction between the low power dissipation and operation frequency of LNA. According to Eq.2.64, these conditions eventuates in high $\Re\{Z_{opt}\}$, and thus large L_s , in which Eq. 2.65 is invalid due to neglection of C_{gd} . Large L_s causes the common-source gate transconductance to be degraded. In this regim, the feedback through C_{gd} can not be ignored any more.

2.4.3 Power-Constrained Noise Optimization (PCNO)

As mentioned previously, proper value of L_s allows the satisfactions of Eq. 2.69 and 2.71 under only conditions of power dissipation. The matching circuit of Figure 2.30 helps to reach desire optimization with employing a series inductance L_g . In power constrained technique, the transistor size is set to the value in which the NF will be minimum, calculated as [41]:

$$W_{opt} \approx \frac{1}{3\omega C_{ox} R_s Q_{in,opt}} \quad 2.73$$

where:

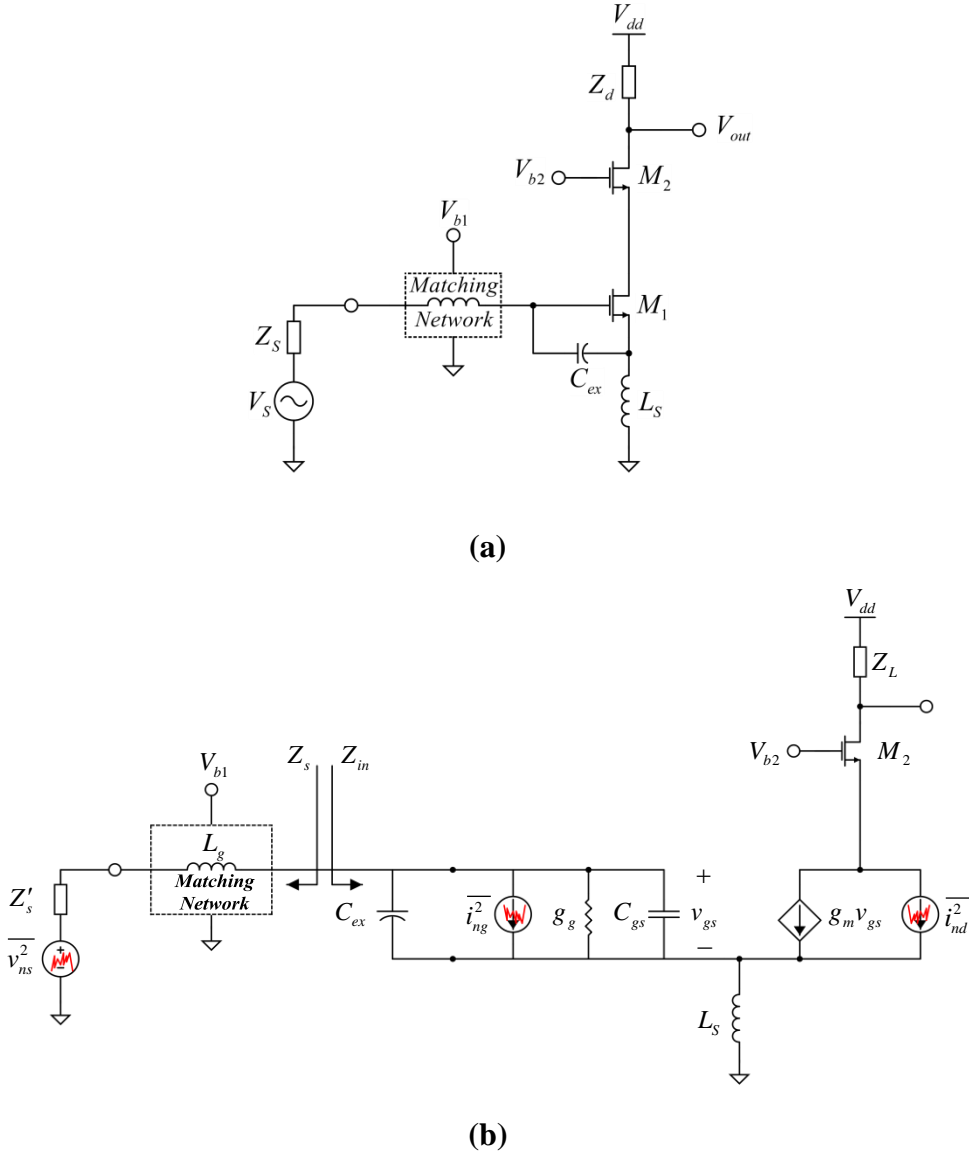


Figure 2.31: PCSNIM optimization technique [6, 49].

$$Q_{in,opt} = |c| \sqrt{\frac{5\gamma}{\delta}} \left[1 + \sqrt{1 + \frac{3}{|c|^2} \left(1 + \frac{\delta}{5\gamma} \right)} \right] \quad 2.74$$

C_{ox} accounts for gate-oxide capacitance per unit area. As a result, the minimum NF will be as [41, 49]:

$$F_{min,P} \approx 1 + 2.4 \frac{\gamma}{\alpha} \frac{\omega}{\omega_T} \quad 2.75$$

In this case, $F_{min,P}$ is higher than F_{min} of the common-source transistor, as either there is mismatch between Z_s and Z_{opt} or L_s is too large.

2.4.4 Power-Constrained Simultaneous Noise and Input Matching (PCSNIM)

Low power implementation, as an inevitable design requirement, can be attained by inserting capacitor C_{ex} , as depicted in Figure 2.31. Adopting a similar analysis and modifying gate induced noise current by:

$$\overline{i_{ng}^2} = 4kT \delta_{eff} \frac{\omega^2 C_t^2}{5g_{d0}} \Delta f \quad 2.76$$

where:

$$\delta_{eff} = \delta \frac{C_{gs}^2}{C_t^2} \quad 2.77$$

$$C_t = C_{gs} + C_{ex} \quad 2.78$$

The noise parameter obtained as [49, 54, 55]:

$$Z_{in} = sL_s + \frac{1}{sC_t} + \frac{g_m L_s}{C_t} \quad 2.79$$

$$R_n = \frac{\gamma}{\alpha g_m} \quad 2.80$$

$$Z_{opt} = \frac{\alpha \sqrt{\frac{\delta}{5\gamma} (1 - |c|^2)} + j \left(\frac{C_t}{C_{gs}} + \alpha |c| \sqrt{\frac{\delta}{5\gamma}} \right)}{\omega C_{gs} \left[\frac{\alpha^2 \delta}{5\gamma} (1 - |c|^2) + \left(\frac{C_t}{C_{gs}} + \alpha |c| \sqrt{\frac{\delta}{5\gamma}} \right)^2 \right]} - sL_s \quad 2.81$$

$$F_{\min} = 1 + \frac{2}{\sqrt{5}} \frac{\omega}{\omega_T} \sqrt{\gamma \delta (1 - |c|^2)} \quad 2.82$$

As it is clear, inserting C_{ex} has no influence on R_n and F_{\min} . These set of parameters, like *SNIM* parameters, are valid for small L_s . To fulfill $Z_{opt} = Z_{in}^*$, as was explained in Eq. 2.69, 2.70, 2.71, and 2.72, we must have:

$$\frac{g_m L_s}{C_t} = \Re\{Z_{in}\} = \Re\{Z_s\} \quad 2.83$$

$$\frac{\alpha \sqrt{\frac{\delta}{5\gamma} (1 - |c|^2)}}{\omega C_{gs} \left[\frac{\alpha^2 \delta}{5\gamma} (1 - |c|^2) + \left(\frac{C_t}{C_{gs}} + \alpha |c| \sqrt{\frac{\delta}{5\gamma}} \right)^2 \right]} = \Re\{Z_{opt}\} = \Re\{Z_s\} \quad 2.84$$

$$sL_s + \frac{1}{sC_t} = \Im\{Z_{in}\} = -\Im\{Z_s\} \quad 2.85$$

$$\frac{j \left(\frac{C_t}{C_{gs}} + \alpha |c| \sqrt{\frac{\delta}{5\gamma}} \right)}{\omega C_{gs} \left[\frac{\alpha^2 \delta}{5\gamma} (1 - |c|^2) + \left(\frac{C_t}{C_{gs}} + \alpha |c| \sqrt{\frac{\delta}{5\gamma}} \right)^2 \right]} - sL_s = \Im\{Z_{opt}\} = \Im\{Z_s\} \quad 2.86$$

Eq. 2.85 can be neglected since it is approximately equal to Eq. 2.86, as previously mentioned. Therefore, we will have three equation and four unknowns: gate biasing voltage (V_{GS}), transistor size (C_{gs}), addition capacitor (C_{ex}), and degeneration inductor (L_s). Thus, arbitrary value of Z_s can be adopted, that leads to *SNIM* with any low power dissipation. Eq. 2.87, derived from Eq. 2.83 and 2.84, verifies the fact that L_s is small:

$$L_s \approx \frac{\alpha \sqrt{\frac{\delta}{5\gamma} (1 - |c|^2)}}{\omega \omega_T C_t} \quad 2.87$$

In contrast, in *SNIM* technique, this value can be achieved as:

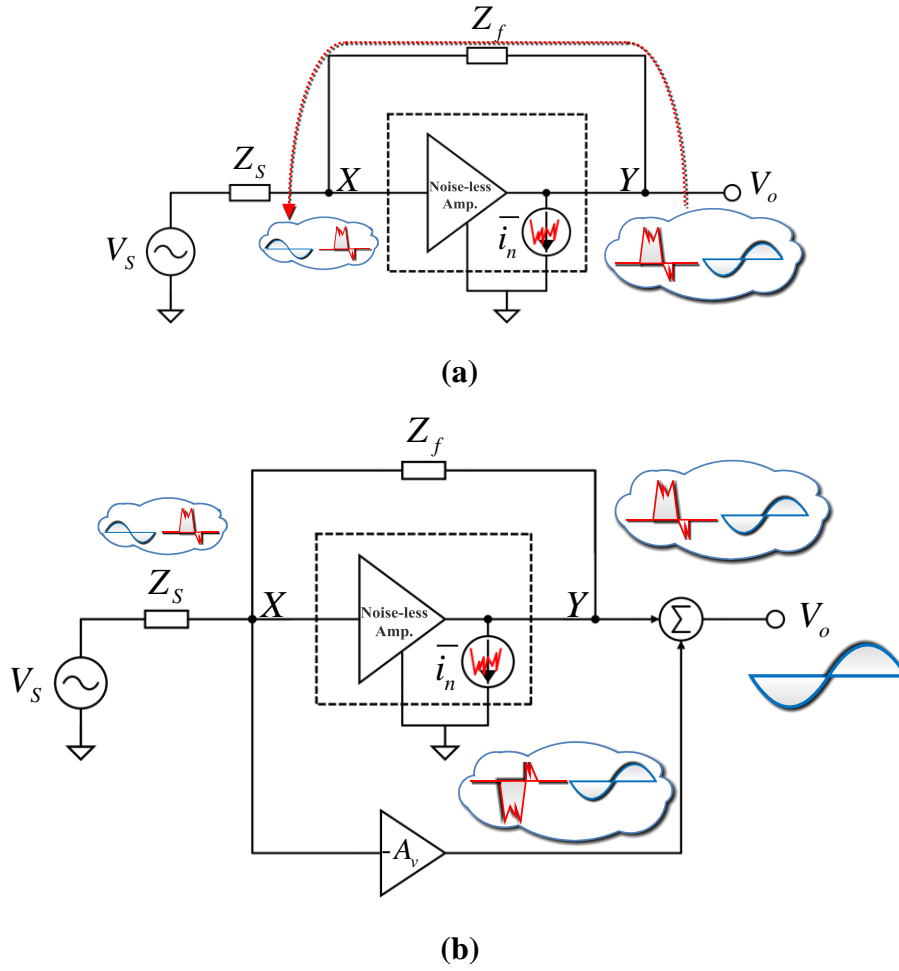


Figure 2.32: Feedback and thermal noise cancellation.

$$L_s \approx \frac{\alpha \sqrt{\frac{\delta}{5\gamma} (1 - |c|^2)}}{\omega \omega_T C_{gs}} \quad 2.88$$

As can be inferred from Eq. 2.87 and 2.88, in *PCSNIM* L_s is reduced by addition of C_{ex} . The common-source LNA with an external gate-source capacitor is discussed in [6] with more details.

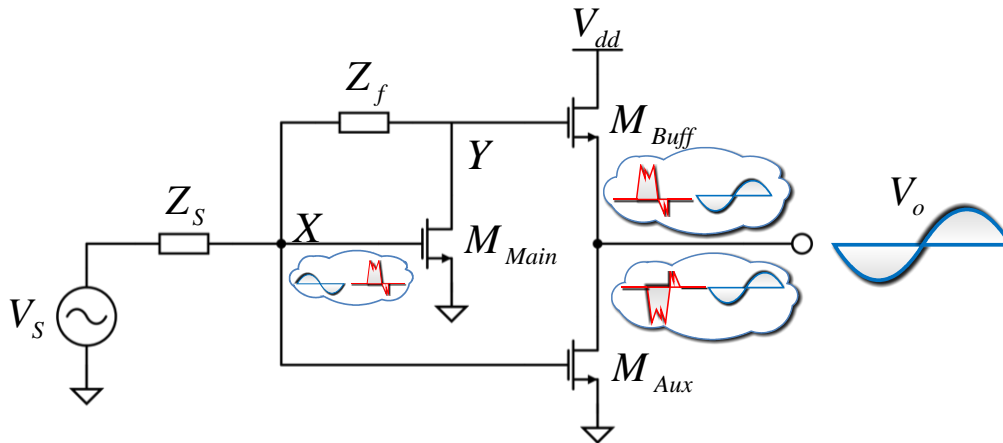


Figure 2.33: Simple implementation of thermal noise canceller with feedback.

2.5 Noise Cancellation Techniques

The noise signals of the circuit elements cannot be removed once they are generated. However, they can be cancelled out each other through noise cancellation techniques. In the case of having two nodes in which the signal is in phase and the noise is out of phase, the noise cancellation is possible [56]. In this section, the noise cancellation techniques will be examined.

2.5.1 Active noise cancellation

By considering a noiseless two-port circuit, as depicted in Figure 2.32.a, and assuming all the noise to be modeled as a current source, the noise cancelling method with common-source (CS) input stage can be applied as follow [37, 56, 57]. The current merely can flows either through R_f or the source through ground. Therefore, at the point X and Y, there will be two noise voltage having same phase but different amplification. However, the signal voltage of these points is out of phase, as a result of an inverting amplifier between two points, and different amplitude. To fulfill the noise cancellation condition, an inverting amplifier must be inserted from point X. Besides, an adder will be needed as depicted in Figure 2.32.b. The inverting amplifier's gain can be calculated by considering the fact that the noise output voltage must be zero that results in:

$$A_{v,noise} = 1 + \frac{R_f}{R_s} \quad 2.89$$

Figure 2.33 shows the simple implementation of this technique with a source follower (CS) as the negative amplifier [58-61]. Thus, the inverting amplifiers' gain and the signal total gain at the output will be as:

$$A_{v,noise} = 1 + \frac{R_f}{R_s} = \frac{g_{m,CS}}{g_{m,Buffer}} \quad 2.90$$

$$A_{v,signal} = 1 - g_{m,Main} R_f - \frac{g_{m,CS}}{g_{m,Buffer}} \quad 2.91$$

The thermal noise cancellation technique also could be applied with common-gate (CG) input stage. This technique is well known as active balun [62]. As depicted in Figure 2.34, the small signal current (i_{in}) is equal to drain current (i_{ds}) since there is no way to ground current but through the input signal path. Therefore, the gain and input impedance can be written as:

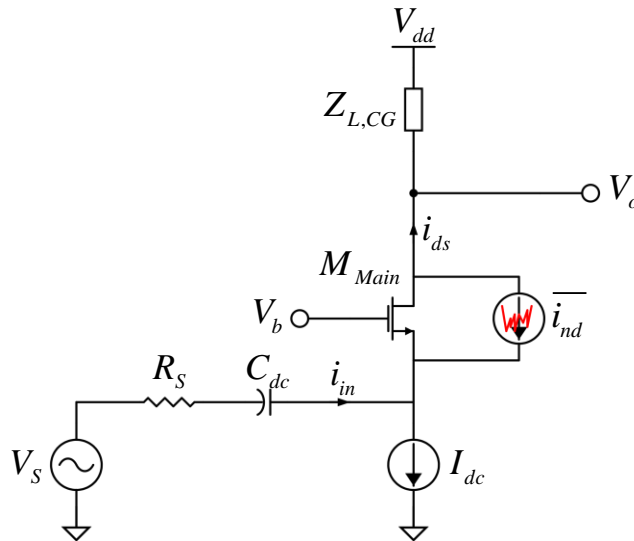


Figure 2.34: Typical common-gate (CG) amplifier.

$$Z_{in} = \frac{1}{g_{m,Main}} \quad 2.92$$

$$A_{v,CG} = g_{m,Main} Z_{L,CG} \quad 2.93$$

On the other hand, to have high input matching:

$$Z_{in} = R_s \quad 2.94$$

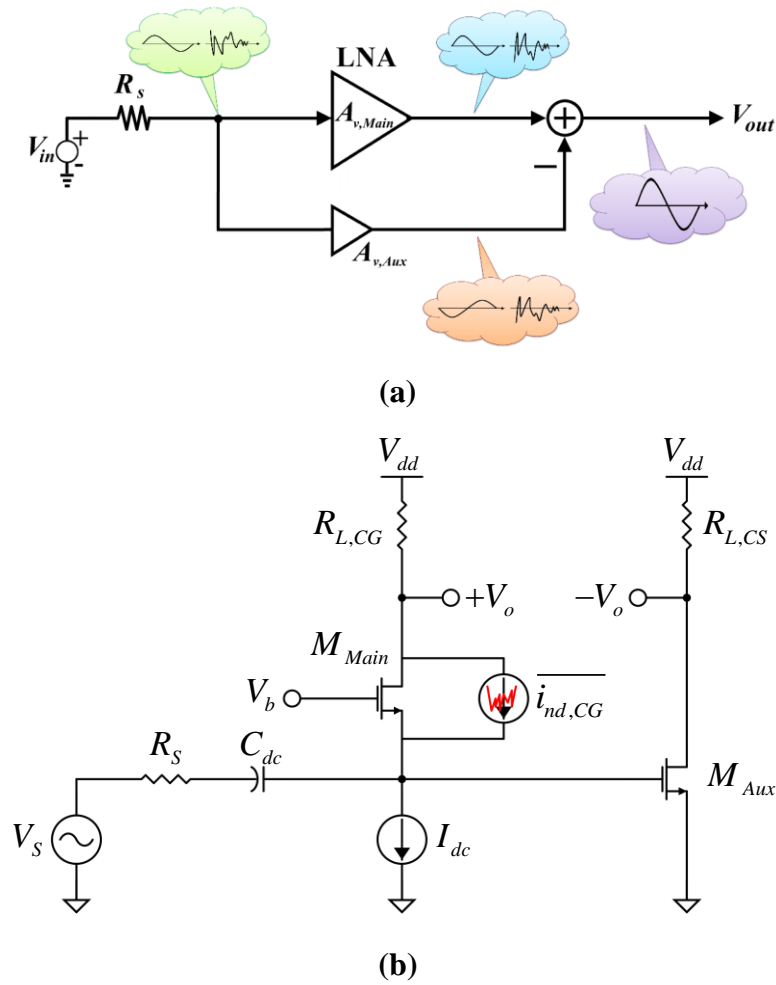


Figure 2.35: Typical forward noise cancellation; (a) block diagram, (b) simple implementation.

Substitute Eq. 2.93 in Eq. 2.94 leads to:

$$A_{v,CG} = \frac{Z_{L,CG}}{R_s} \quad 2.95$$

Considering the fact that the input and output noise voltage of CG is fully correlated with anti-phase with each other makes this case an ideal case of main amplifier for forward thermal noise cancelation technique which is depicted in Figure 2.35.a. Basically, the negative gain booster is presented by a CS stage. As Figure 2.35.b depicts, the channel thermal noise current of CG stage ($i_{nd,CG}$) generated the following two voltages at input and output of CG stage, respectively [62].

$$v_{n,in} = \beta i_{nd,CG} R_s \quad 2.96$$

$$v_{n,o+} = -\beta i_{nd,CG} R_{L,CG} \quad 2.97$$

where

$$\beta = \frac{Z_{in}}{Z_{in} + R_s} \quad 2.98$$

The Eq. 2.98 shows that β is the voltage dividing ratio between the input impedance (Z_{in}) and the source ones (R_s). The β would be 1/2 in case of impedance matching at input. To make sure that the noise of both side of balun will cancel out each other, the CS gain ($A_{v,CS}$) should be equals with posit sign to the CG ones ($A_{v,CG}$).

$$A_{v,CS} = -A_{v,CG} = -\frac{R_{L,CG}}{R_s} \quad 2.99$$

The above equivalency could be achieved by adjusting the size and load of the CS stage. Although, this technique is improving the noise feature by cancelling the CG noise, it is still suffering from the noise that introduced to circuit by CS amplifier. One possible solution for this problem is the capacitor cross coupled (CCC) common gate technique which provides a simultaneous doula way the noise cancellation for both stage [63-67]. In this configuration, respect to the positive input, M_1 works as CG amplifier. At same time, M_2 plays the CS stage role and transfers the M_1 's reversed channel noise as well as positive input signal to the negative

output (Figure 2.36). The same scenario is applied to the negative input and M_2 . Finally, the differential outputs of CCC would be clear from the channel noise of both transistors.

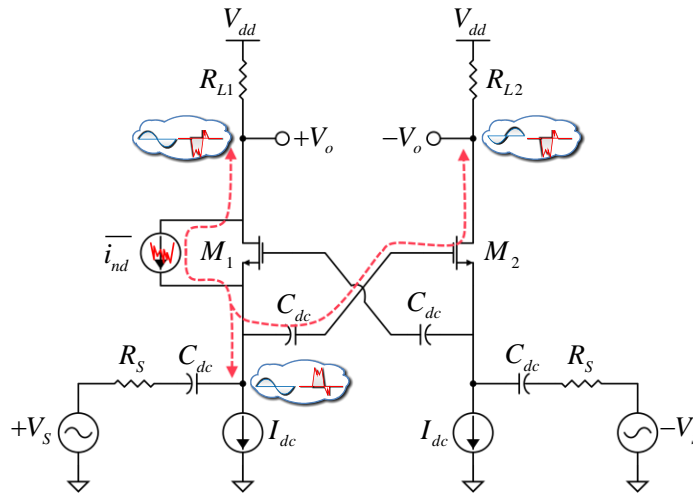


Figure 2.36: Typical capacitor cross coupled (CCC) common-gate (CG) amplifier.

2.5.2 Passive Noise Cancellation

The passive noise cancellation is almost following the same principal of the active ones that was introduced in section 2.5.1. The differences between these two techniques come from applying either passive or active balun [68, 69]. Moreover, recent publication shows that the combination of the passive and active techniques can be count as an alternative to rich even better noise performance [70, 71]. Figure 2.37 shows schematically the method that can be adopted for low power and low noise figure configuration. The transformer is employed to cancel the noise voltage created by the CG transistor drain current. As a result, there is no need to additional negative amplifier that consumes power. Considering the noise source in Figure 2.37, it will be found that the noise voltages $v_{n,in}$ and $v_{n,out}$ are generated by current flowing, one through the L_s and R_L , and the other through L_p and R_s . The transformer produces $v_{n,x}$ having apposite phase and correlated with $v_{n,out}$, so, it can partly cancel $v_{n,in}$. However, the high frequency power will be reduced.

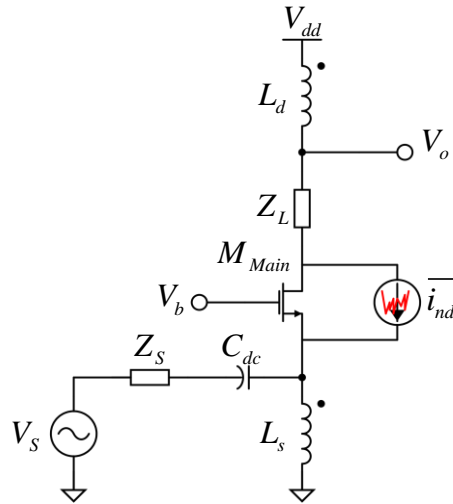


Figure 2.37: Typical passive noise canceler amplifier[72].

2.6 Non-linearity Neutralization

RF-system linearity is highly constrained by occupied narrow frequency bands and wireless communication standards. Besides, LNA, as a first stage of a RF receiver, must be adequately linear to avoid interferences as it deeply studied in sections 2.1 and 2.2. In addition, LNA linearization techniques are more challenging compared with base band circuit, as they must guarantee low noise figure, input matching, gain, and low power consumption. Consequently, traditional linearization methods employed in low frequencies cannot be applied for LNAs. It is worth pointing out that despite the narrowband linearization approaches, the broadband techniques not only should improve the third- order intercept point (IIP3), but also they must modified the second-order intercept point (IIP2) and 1dB compression point (P_{1dB}) as well. As a result, the effect of two-tone frequency and frequency spacing on IIP2/IIP3 should be discussed.

We can consider an LNA as a weakly nonlinear system due to the fact that the inputs are usually high frequency and low amplitude. Therefore, its frequency-dependent distortion and the possible compensation methods can be studied by Volterra-series analysis [73-75].

Although CMOS technology is the first choice for on-chip circuit, there are some issues in implementation of deep-submicron (DSM) systems such as mobility degradation, nonlinear output conductance, poly-gate depletion, and velocity saturation [44, 46, 76]. Moreover, since the adequate transconductance and linearity in MOSFETs need high DC current, the DC power reduction should also be considered in LNA's linearization techniques.

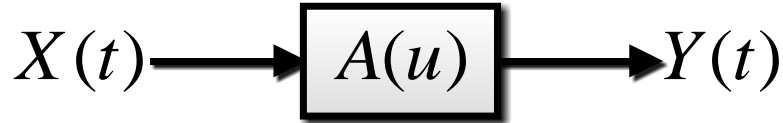


Figure 2.38: Nonlinear block.

Figure 2.38 represents a weakly nonlinear amplifier without memory effects. This system can be approximated by the first three power series term as:

$$Y(t) = A(X(t)) = a_1X(t) + a_2X^2(t) + a_3X^3(t) \quad 2.100$$

where a_1 , a_2 , a_3 denote the linear gain and second and third order nonlinearities coefficients, respectively. If we make a_2 and a_3 so small that can be neglected, the term a_1 will be remained and will have:

$$Y(t) \approx a_1X(t) \quad 2.101$$

The following discussion devoted to the LNA linearization methods. The main LNA nonlinearity causes are nonlinear transconductance g_m and nonlinear output conductance g_{ds} . The former turns the linear input voltage to nonlinear drain current, known as “input limitation”, while the latter is swing, called also “output limitation.” Under the saturation condition and for the frequencies under $f_T/10$, the CMOS parasitic capacitances, C_{gs} , C_{gd} , C_{sb} , and C_{db} are almost linear and bring distortion less than g_m/g_{ds} . Albeit, the effect of C_{gd} via the feedback should be observed. The only factor involved in IIP2 is intrinsic second-order distortion, however, the IIP3 originates from two defects: the intrinsic third-order distortion and the intrinsic second-order distortion compounded with feedback, known as “second-order interaction.”

2.6.1 Feedback

The negative feedback circuit with a nonlinear amplifier A and linear feedback β without memory effects is schematically shown in Figure 2.39. $X(t)$ and $Y_{CL}(t)$ are the input and output signals, respectively, x_f is the feedback signal, and x_e is the X and x_f difference.

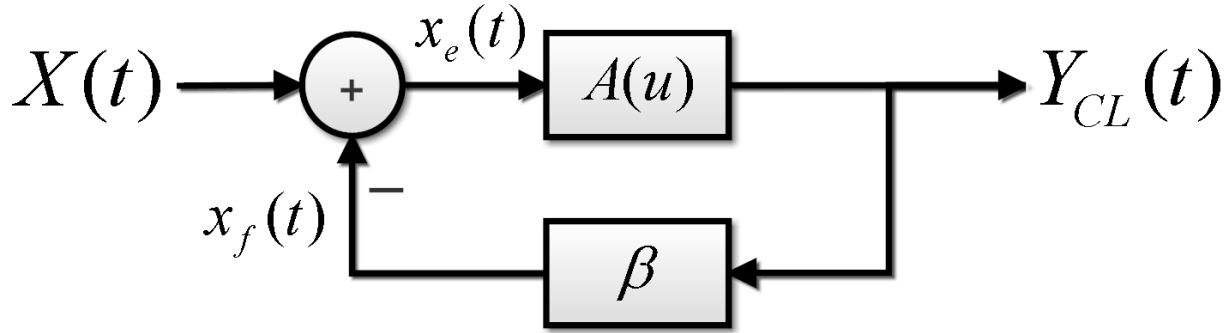


Figure 2.39: Block diagram of linear feedback with nonlinear forward block.

The third order closed-loop power series for Y_{CL} can be obtained as [77]:

$$Y_{CL}(t) = A_{CL}(X(t)) = b_1 X(t) + b_2 X^2(t) + b_3 X^3(t) \quad 2.102$$

We can derive the closed-loop linear gain b_1 and second/ third-order nonlinearity b_2 and b_3 , respectively, as:

$$b_1 = \frac{a_1}{1 + A_{OL}} \quad 2.103$$

$$b_2 = \frac{a_2}{(1 + A_{OL})^3} \quad 2.104$$

$$b_3 = \frac{1}{(1 + A_{OL})^4} \left[a_3 - \frac{2a_2^2}{a_1} \frac{A_{OL}}{1 + A_{OL}} \right] \quad 2.105$$

Where $A_{OL} = a_1 \beta$ denotes the linear open-loop gain. Furthermore, the *IIP3* of the closed-loop circuit and amplifier A can be attained as:

$$A_{IIP2,Amp} = \sqrt{\frac{|a_1|}{|a_2|}} \quad 2.106$$

$$A_{IIP3,CL} = \sqrt{\frac{|b_1|}{|b_2|}} = \sqrt{\frac{|a_1|}{|a_2|} |(1 + A_{OL})^2|} \quad 2.107$$

$$A_{IIP3,Amp} = \sqrt{\frac{4|a_1|}{3|a_3|}} \quad 2.108$$

$$A_{IIP3,CL} = \sqrt{\frac{4|b_1|}{3|b_3|}} = \sqrt{\frac{4|a_1|}{3|a_3|} \frac{|(1 + A_{OL})^3|}{\left|1 - \frac{2a_2^2}{a_1 a_3} \frac{A_{OL}}{1 + A_{OL}}\right|}} \quad 2.109$$

As can be inferred, A_{IIP2} is improved by a factor of $(1 + A_{OL})$ in the negative feedback. In addition, when $a_2 \approx 0$, $A_{IIP3,CL}$ is also increased by a factor of $(1 + A_{OL})$. For ordinary biasing in which g_1 and g_3 is out of phase, nonzero g_2 decrease $IIP3$. As mentioned previously, this phenomenon cause second-order interaction [73, 78] which degrades $IIP3$.

However, based on the literatures, the feedback linearity modification in LNAs cannot solve the problem since the conditions on gain, noise figure, and power consumption prevent the open-loop gain, A_{OL} , to be large. Moreover, the second-order non-linearity contribution in $IM3$ restricts the application of this technique in LNAs rather than baseband circuits. We will investigate this technique and its issue with more details later.

2.6.2 Derivative Supersession (DS)

The derivative supersession (DS) technique is well known method for nonlinearity cancelation. This method is widely applied in designing of LNAs and mixer in previous years studies [79-82]. The DS technique is also known as multi gate transistor (MGT) due to its multi transistor configurations [79]. This method is basically laid over the nonlinearity behavior of transistor and directly works with biasing point. To explain this subject more deeply it is

necessary to study the effect of biasing point and feedforward effect over the transistor nonlinearity.

2.6.2.1 Optimum Gate Biasing

As discussed before, the most effective source of nonlinear harmonics in CMOS technology is the transconductance g_m . In very simple format, the drain-source current (I_{ds}) can be expressed as follow:

$$I_{ds} = I_{DS} + i_{ds} \quad 2.110$$

where the first and second terms represent the DC and the AC currents, respectively. The AC part of current is a function of gate-source voltage (v_{gs}). By the aim of power series, the AC term would be:

$$i_{ds} = f(v_{gs}) = g_1 v_{gs} + g_2 v_{gs}^2 + g_3 v_{gs}^3 \quad 2.111$$

where g_1 , g_2 , and g_3 are the coefficient of power series and defined as follow:

$$g_1 = \frac{\partial I_{ds}}{\partial v_{gs}}, g_2 = \frac{1}{2!} \frac{\partial^2 I_{ds}}{\partial v_{gs}^2}, g_3 = \frac{1}{3!} \frac{\partial^3 I_{ds}}{\partial v_{gs}^3} \quad 2.112$$

The g_1 is the linear part of the transconductance and the other coefficients are present the higher order of nonlinear harmonics. It is essential to mention here that, although, the power series of I_{ds} is not finished with these three sentences, the higher order sentences are very weak in term of the power compare to the first 3 ones. By this assumption, only the characterizations of the first three coefficients are taken into account in continues. To extract their curves as function of gate-source voltage, first, the drain-source voltage (v_{DS}) is fixed at supply voltage (V_{dd}) which in this case is 1.2V. The I_{ds} is extracted for the v_{gs} which is swept between 0 and V_{dd} (Figure 2.40.a). After all, the coefficients' curves are available by getting first, second, and third derivation from current ones (Figure 2.40.b, c, and d).

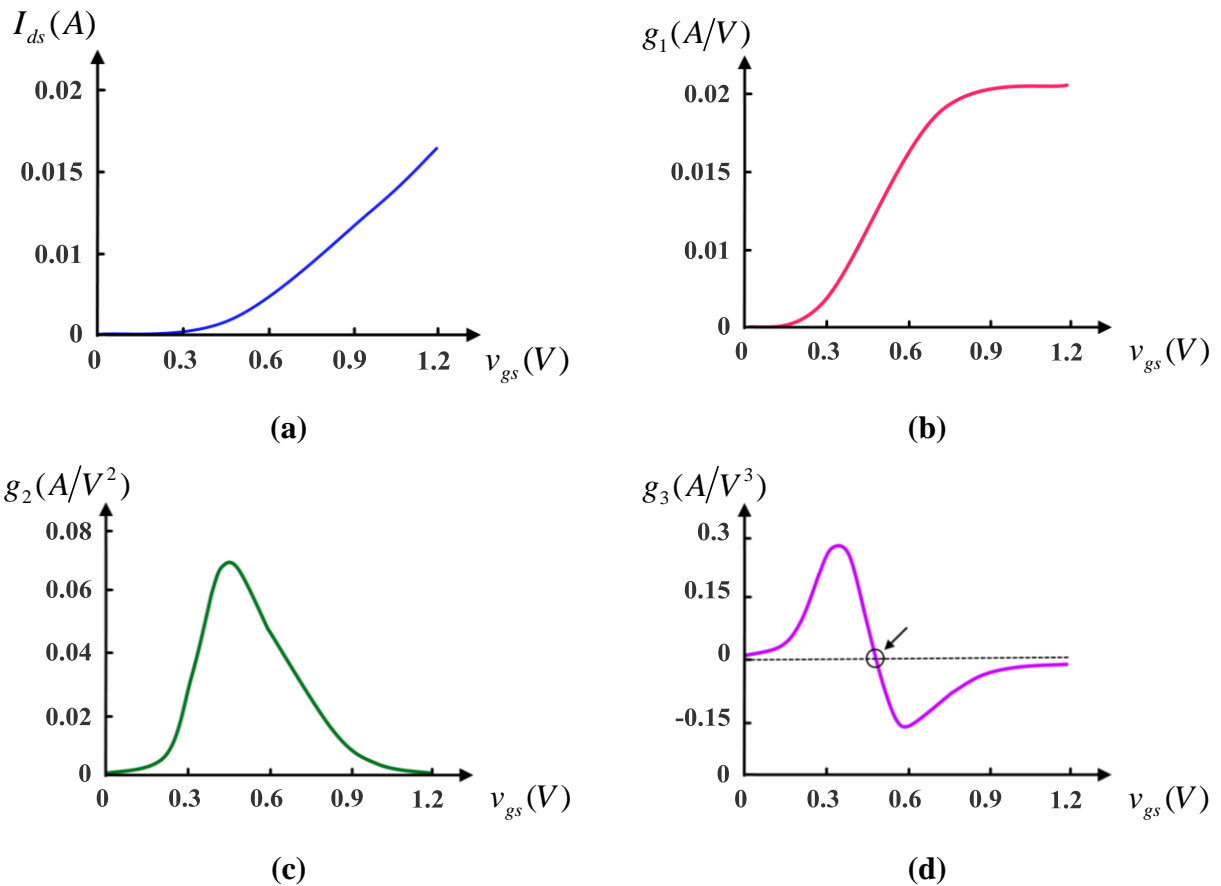


Figure 2.40: NMOS current and transconductances curves.

The first important point about all the Figure 2.40 is the linear behavior of these curves versus the variation of transistor width. These figures depict the fact that the drain-source current as well as its derivatives are linearly related to the size of transistor. We will back to this result later.

Another important point is the sign and value of the coefficients. The g_1 and g_2 are demonstrating positive sign. However, the g_3 illustrates 3 different regions in its curve.

- $g_3 > 0$ indicating the region which transistor works in deep triodes.
- $|g_3| \approx 0$ indicating a neighborhood which velocity saturation takes place.
- $g_3 < 0$ indicating the strong saturation region which square law is applied.

Through all of these three regions, the second one is most interesting ones for harmonic cancelation, which is also known as “moderate inversion” region [83]. One way to terminate a specific harmonic is to decrease its amplitude in power series. The “optimum sweet spot” of IIP3 is defined as the operation point which is the zero crossing of g_3 [83]. The third harmonic products of $g_3 v_{gs}^3$ would be determined by adjusting the operation point near the sweet spot. This technique is known as “optimum gate biasing” [84]. While this technique comes with a very simple criteria, it also requires a lot of challenging conditions which counts as its draw backs. The high sensitivity to biasing point, operation frequency, and manufacturing process are some of it as toughest conditions. In spite of all these problems, almost same principal of optimum gate biasing is developed in the derivative supersession.

2.6.2.2 Feedforward

To perfectly neutralize the nonlinearity of amplifier with minimum effect over the linear coefficient (g_1) is demanding more degree of freedom. Usually, the second nonlinearity coefficient is assumed to cancel out by differential configurations. Neutralization of the third order products could be accomplished by subtracting additional nonlinear signal. This technique is known as feedforward neutralization [85]. As illustrated in Figure 2.41, the output of the feedforward (Y_{Tot}) is presented by the subtracting of the outputs of main path (Y_{Main}) from that of the auxiliary path (Y_{Aux}). The main and auxiliary paths are basically consisted of two identical main amplifiers. In addition, the auxiliary past is involving b and $1/b^n$ ($b < 1$) scaling amplifiers at the input and output, respectively. The n could be allocated either as 2 or 3 for canceling out the IM2 or IM3, respectively. However, as discussed above, the neutralization IM3 is the goal of feedforward technique. By considering all of these facts, the equation hold the relation between the input and output will be:

$$Y_{Main} = g_1 X + g_2 X^2 + g_3 X^3 \quad 2.113$$

$$Y_{Aux} = \frac{g_1}{b^{n-1}} X + \frac{g_2}{b^{n-2}} X^2 + \frac{g_3}{b^{n-3}} X^3 \quad 2.114$$

$$Y_{Tot} = Y_{Main} - Y_{Aux} = g_1 \left(1 - \frac{1}{b^{n-1}}\right) X + g_2 \left(1 - \frac{1}{b^{n-2}}\right) X^2 + g_3 \left(1 - \frac{1}{b^{n-3}}\right) X^3 \quad 2.115$$

Although, the third harmonic can be canceled to obtain high IIP3 by applying $n=3$, this technique suffering from several problems. Due to degradation in linear coefficient (Eq. 2.115), a reduction in linear gain is predictable. Also, as reverse relation between the noise figure (NF) and gain of amplifier, it would be increased as well. Furthermore, as a result of the extra active devices, more noise would be presented to the output.

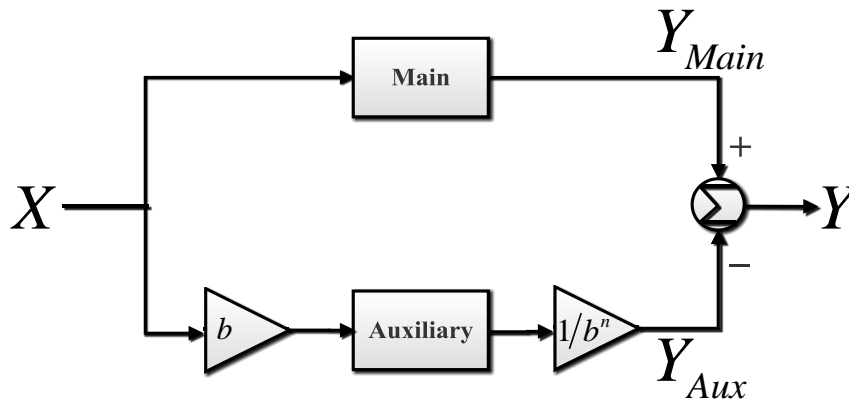


Figure 2.41: Block diagram of feedforward linearization technique.

2.6.2.3 DS method

As it illustrated before, the alternative method that is resulted from combination of the optimum gate biasing and feedforward method is derivative suppression method (DS). This method is specific case of feedforward technique and obtained for $b=1$. This technique presents a practical solution for problems which were discussed above; the short range of high value IIP3 concerned in optimum gate biasing technique and the gain reduction in feedforward technique.

The combination between feedforward and optimum gate biasing eventuate to a noticeable expansion in zero crossing of the third order coefficient ($g_{3,tot}$). As discussed before, the third order coefficient (g_3) of drain-source current (I_{ds}) is experiencing a sign change around the optimum sweet spot due to transition between the moderate to strong inversion (Figure 2.41). Assuming the case that the main amplifiers of the feedforward technique are replaced with two

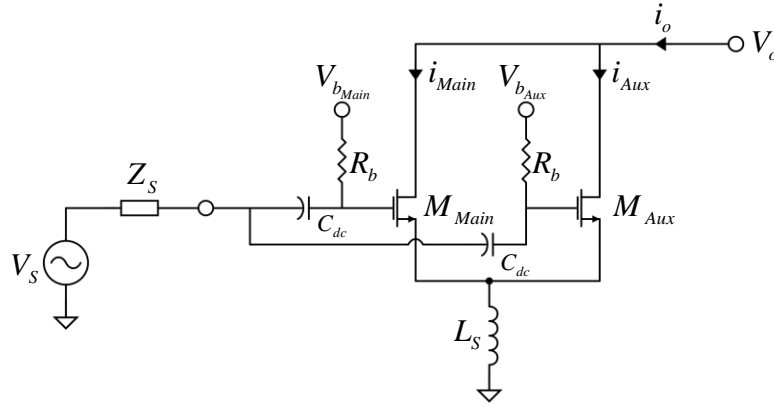


Figure 2.42: Schematic demonstration of DS method.

MOSFETs are biased at the picks of two sides of the optimum sweet spot (Figure 2.42). When the currents of both main and auxiliary path are added up together, the third harmonic components are canceled out each other. Compare to the optimum biasing technique, this method present a window of cancelation instate of a very tiny interval. The DS method takes advantages from multiple gate connected transistors structure, it is also known as the “multiple gate transistor technique” (MGTR) [86, 87]. In Figure 2.42, the main and auxiliary paths are utilized by transistors M_A and M_B which are biased at strong inversion and moderate, respectively. The main and auxiliary transistors represent the negative and positive peaks, respectively. Figure 2.43 depicts the maximum width of window is obtained when the positive peak is equaled to the negative ones which is usually achieved by scaling up the auxiliary transistor compare to the main ones.

The DS method comes with its own price. The most important issue with DS method is its pure frequency robustness. In other words, although it provides a good degree of cancelation, these results are just valid in low frequency. This issue rises up due to the feedback that is held by the source degeneration inductance. As discussed previously in feedback section, the nonlinear systems with feedback are suffered from the 2nd-order interaction. In the DS method, this feedback path connects the drain current (I_{ds}) to the gate-source voltage (v_{gs}) of the M_B . The IIP3 expression for DS method is calculated in [84] for the RF frequency with aid of Volterra series.

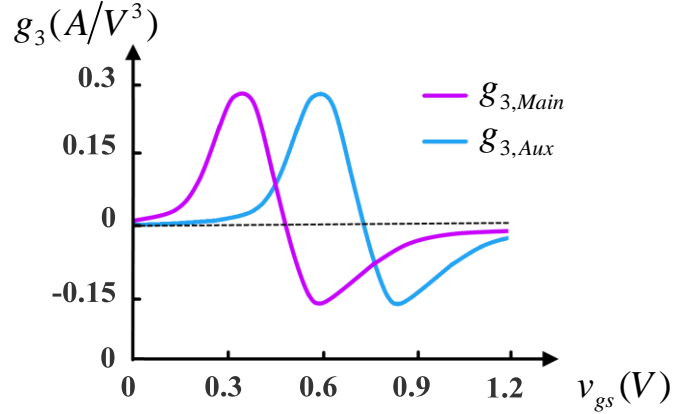


Figure 2.43: The third derivative of main and auxiliary currents.

$$IIP3 = \frac{4g_{1,tot}^2 \omega^2 LC_{gs,tot}}{3|\epsilon_{Con}|} \quad 2.116$$

where

$$\epsilon_{Con} = g_{3,tot} - \frac{2}{3} \frac{g_{2,tot}^2}{g_{1,tot} + \frac{1}{2j\omega L} + 2j\omega C_{gs,tot} + 2Z_s \omega \frac{C_{gs,tot}}{L}} \quad 2.117$$

The “tot” index in Eq. 2.116 and Eq. 2.117 is representing the total summation of the same term of main and auxiliary transistors; for example $C_{gs,tot} = C_{gs,Main} + C_{gs,Aux}$. From Eq. 2.117, it is obvious that the smaller ϵ_{Con} will result the better IIP3. The first term of ϵ_{Con} , represents the third order coefficient which is degraded off by the DS method. The second term is product of the feedback and indicates the 2nd-order interaction effects over IM3. This term is function of the second order coefficient, $g_{2,tot}$, and frequency. Therefore, the limitation and range of IIP3 will be determined by this term at the high frequency.

2.6.2.4 Modified Derivative Supersession Technique (MDS)

The modified derivative supersession method (MDS) was founded as on-chip solution for 2nd-order interaction in derivation supersession method (DS) [88-90]. As shown in Figure 2.44, the MDS method was implemented with two semi-different circuits that follow same concept as

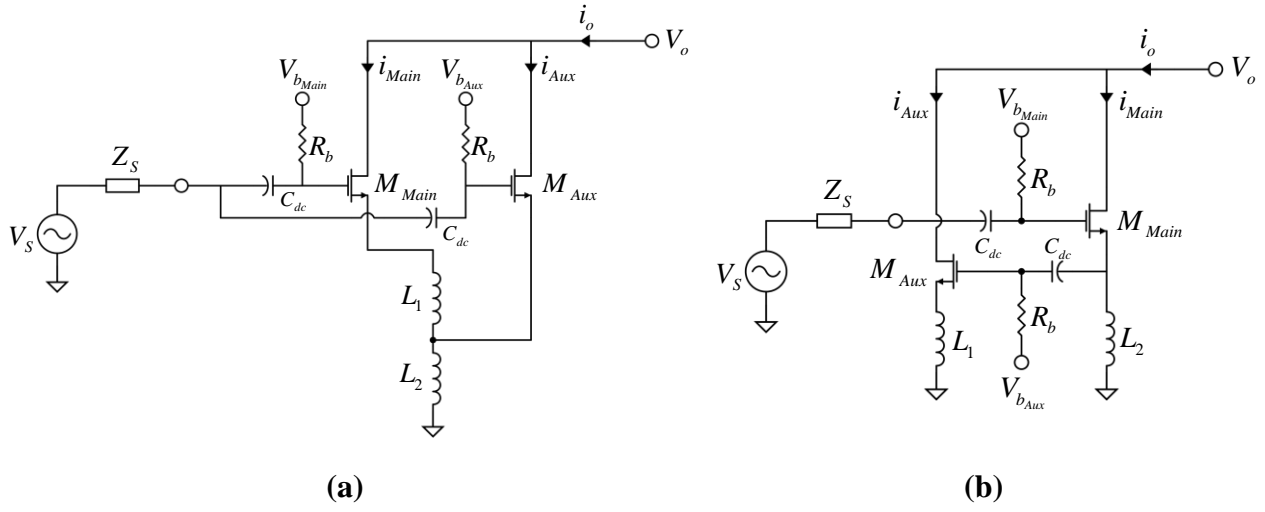


Figure 2.44: Different realizations of MDS method.

explain below. In this method, the vector of 3rd order nonlinearity contributed by the auxiliary path ($g_{3,Aux}v_{gs,Aux}^3$) will be turned in with aid of addition phase from inductor L_2 . In other words, the angle of $g_{3,Aux}v_{gs,Aux}^3$ is controlled through the size of this inductor (Figure 2.45). So, the vector of $g_{3,Aux}v_{gs,Aux}^3$ could be spilt out to the two different vectors in the opposite directions of the 2nd-order interaction ($g_{2,Main}v_{gs,Main}^2$) as well as the 3rd order nonlinearity of the main path ($g_{3,Main}v_{gs,Main}^3$). Considering this fact, the residual part of IM3 due to the 2nd-order interaction in conventional DS method is eliminated now in the MDS method. The IIP3 expression for MDS method is derived in [89] and [90] at the RF frequency by the aid of the Volterra series.

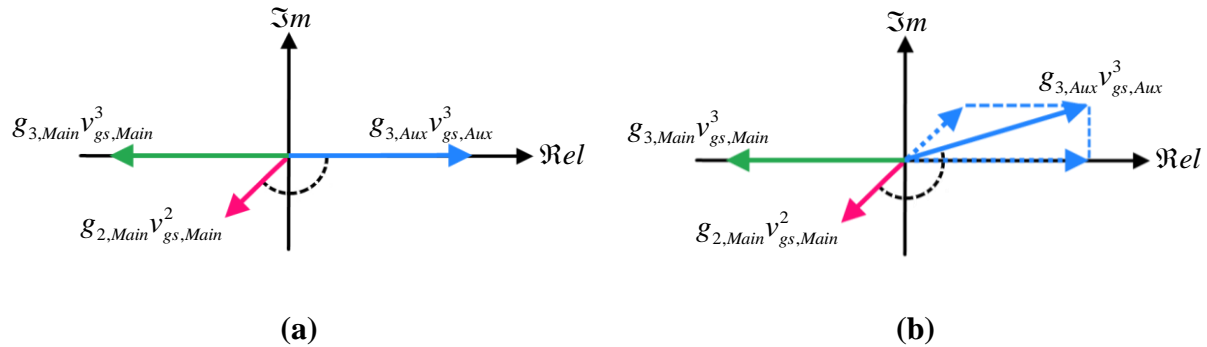


Figure 2.45: The distortion components (a) DS (b) MDS

$$IIP3 = \frac{4g_{1,Main}^2 \omega^2 \left[L_1 (C_{gs,Main} + C_{gs,Aux}) + L_2 C_{gs,Main} \right]}{3 |\mathcal{E}_{Mod,1}|} \quad 2.118$$

where

$$\mathcal{E}_{Mod,1} = g_{3,Aux} (1 + j\omega L_2 g_{1,Main}) \left[1 + (\omega L_2 g_{1,Main})^2 \right].$$

$$\left\{ 1 + \frac{L_2 C_{gs,Main}}{L_1 (C_{gs,Main} + C_{gs,Aux}) + L_2 C_{gs,Main}} \right\} + g_{3,Main} - \frac{2}{3} \frac{g_{2,Main}^2}{g_{1,Main}} \frac{1}{1 + \frac{1}{j2\omega(L_1 + L_2)g_{1,Aux}}} \quad 2.119$$

$$IIP3 = \frac{1}{|A_1(j\omega)|^2} \frac{g_{1,Main}^2}{\mathcal{E}_{Mod,2}} \quad 2.120$$

where

$$A(s) = \frac{1 + s^2 C_{gs,Aux} (L_1 + L_2)}{Z_o(s) + s g_{1,Main} L_1 (1 + s^2 L_2 C_{gs,Aux})} \quad 2.121$$

$$\mathcal{E}_{Mod,1} = g_{3,Main} - \frac{g_{2,Main}^2}{3g_{1,Main}} + g_{3,Aux} n(j\omega) |n(j\omega)|^2 \frac{2 + \omega^2 L_2 C_{gs,Aux}}{2(1 + \omega^2 L_2 C_{gs,Aux})} \quad 2.122$$

$$Z_o(s) = (1 + s C_{gs,Aux} Z_s) \left[1 + s^2 C_{gs,Aux} (L_1 + L_2) \right] + s^2 L_1 C_{gs,Main} (1 + s^2 L_2 C_{gs,Aux}) \quad 2.123$$

$$n(j\omega) = \frac{j\omega L_1 (g_{1,Main} + j\omega C_{gs,Main})}{1 - \omega^2 C_{gs,Aux} (L_1 + L_2)} \quad 2.124$$

The Eq. 2.118 and 2.120 show the IIP3 expression for circuit represented in [89] and [90], respectively. Although, the Modified DS solve the 2nd-order interaction problem, its drawback should be considered carefully. Most of the difficulties of this method are referred to the auxiliary transistor which is listed below.

- Due to the large gate parasitic capacitance at weak inversion and triode region, the operating frequency should not be chosen arbitrary high.
- Due to the auxiliary biasing issue, the input swing cannot be allocated the large values.

- Due to the sensitivity of auxiliary transistor to the scaling as well as the difficulty of matching between two transistors under the PVT variations, to catch good results, the manual biasing adjustment is strongly recommended.

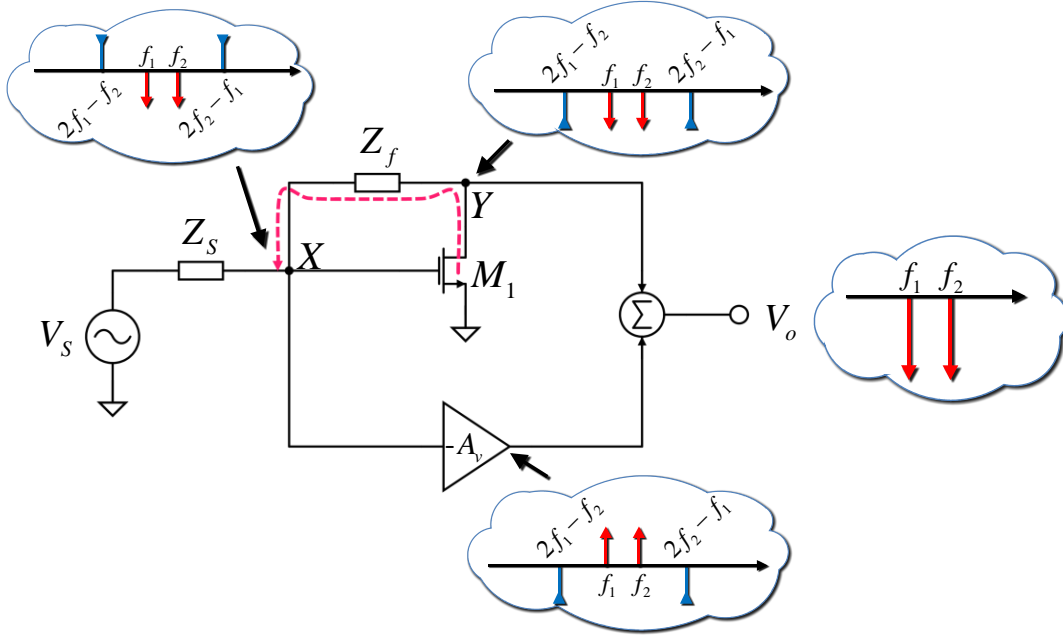


Figure 2.46: The IM3 neutralization presented by noise cancellation feedback method.

2.6.3 Noise and distortion cancellation

Distortion cancellation can be obtained using the same technique employed for noise cancellation. The drain current of the matching device based on the Taylor approximation is derived as [58]:

$$I_{ds} = g_{Main} V_X + I_{NL} \quad 2.125$$

where NL depicts the high order nonlinearity terms. According to Figure 2.46, the voltage of node X and Y can be expressed as:

$$V_X = V_S - R_S (g_{Main} V_X + I_{NL}) \quad 2.126$$

$$V_Y = V_S - (R_S + R_f)(g_{Main}V_X + I_{NL}) \quad 2.127$$

In fact, the similarity between distortion cancellation and noise cancellation comes from the same relation between node X and Y in Eq. 2.126 and Eq. 2.127 and in noise cancellation equations, in which, the voltage amplitude of the node Y is $1 + R_f/R_S$ times greater than that of node X .

Similarly as the noise cancellation, in the distortion cancellation the feed forward gain of $A_v = 1 + R_f/R_S$ can cancel the matching stage's nonlinearity terms. However, the distortion of the noise cancellation stage will remain.

The noise and distortion cancellation technique is schematically depicted in Figure 2.46 for a CS stage. At the input, the same amplitude tones of f_1 and f_2 produce the 3rd intermodulation distortion factor of $2f_1 - f_2$ and $2f_2 - f_1$. As the distortion products in the node X and Y are in phase and the fundamental signals are in anti-phase, the distortion cancellation can be obtained by inserting a feedforward path of gain A_v to the output that cancels out the distortion products at the output. The same scenario and explanation with a little difference could apply to active balun noise cancellation (Figure 2.35).

2.7 Summery

Just to review what was brought up in this chapter, we started from various wireless receivers including classical and super heterodyne architectures, homodyne technology, and ultra-low power design. Then, frequency allocation spectrum, network architecture, and specifically WBAN application and IEEE 802.15 standardization were discussed to provide a better context for the necessity and importance of a high gain, low noise, low weight and cost-efficiently LNA. LNA's gain, noise sources, noise figure and S-parameter description of its gain were introduced in order to pave the way for argue on different noise optimization techniques such as CNM, SNIM, PCNO, and PCSNIM. Active and passive noise cancelation techniques, non-linearity neutralization including feedback effects and DS method were debated. In the next

section, these foundations will be applied to bring forward a novel LNA optimization method and demonstrate its superiority over the aforementioned techniques.

Chapter 3

High Gain, Low Power, CMOS Current Reused LNA with Noise Optimization

CMOS technology has been widely investigated in wireless communication systems due to its compactness and low cost manufacturing [1]. The low noise amplifiers (LNA) play a significant role in the transceiver blocks at the radio frequencies because of its improvement of the signal to noise ratio characteristics. Upon the noise critical situation at the input transducer systems, these families of CMOS amplifiers are reserved mainly as the first stage in the most of the architectures. Furthermore, low cost and compactness, low power consumption, high linearity in the pass band, and acceptable stability increase its practical importance. In order to enhance the quality of front-end amplifiers' operation, they should be considered as a complete rather than a single block. That is, all of the elements included in the structure must be studied, designed, and optimized simultaneously. Among the various possible topologies for the LNA structures, those front end amplifiers which have CMOS inverter current reused (CICR) as their core are outstanding owing to the wideband, high gain, and low power consumptions characteristics. However, the complicated optimization of the CICR category has not been analyzed yet. The published optimization techniques are mostly applied to either common source (CS) or cascade LNAs [6, 49]. These methods, consequently, are omitting the important effects of other noise sources, such as stacking an additional transistor; the obtained noise figure (NF) is not optimum value. In this work, by developing and modifying the previous methods for CICR, we achieve a more accurate procedure for stacked transistors. This chapter is organized as follows: in Section 3.10 the fundamental optimization analysis technique of CICR is discussed and Section 3.2 presents the proposed CICR optimized LNA and simulation results.

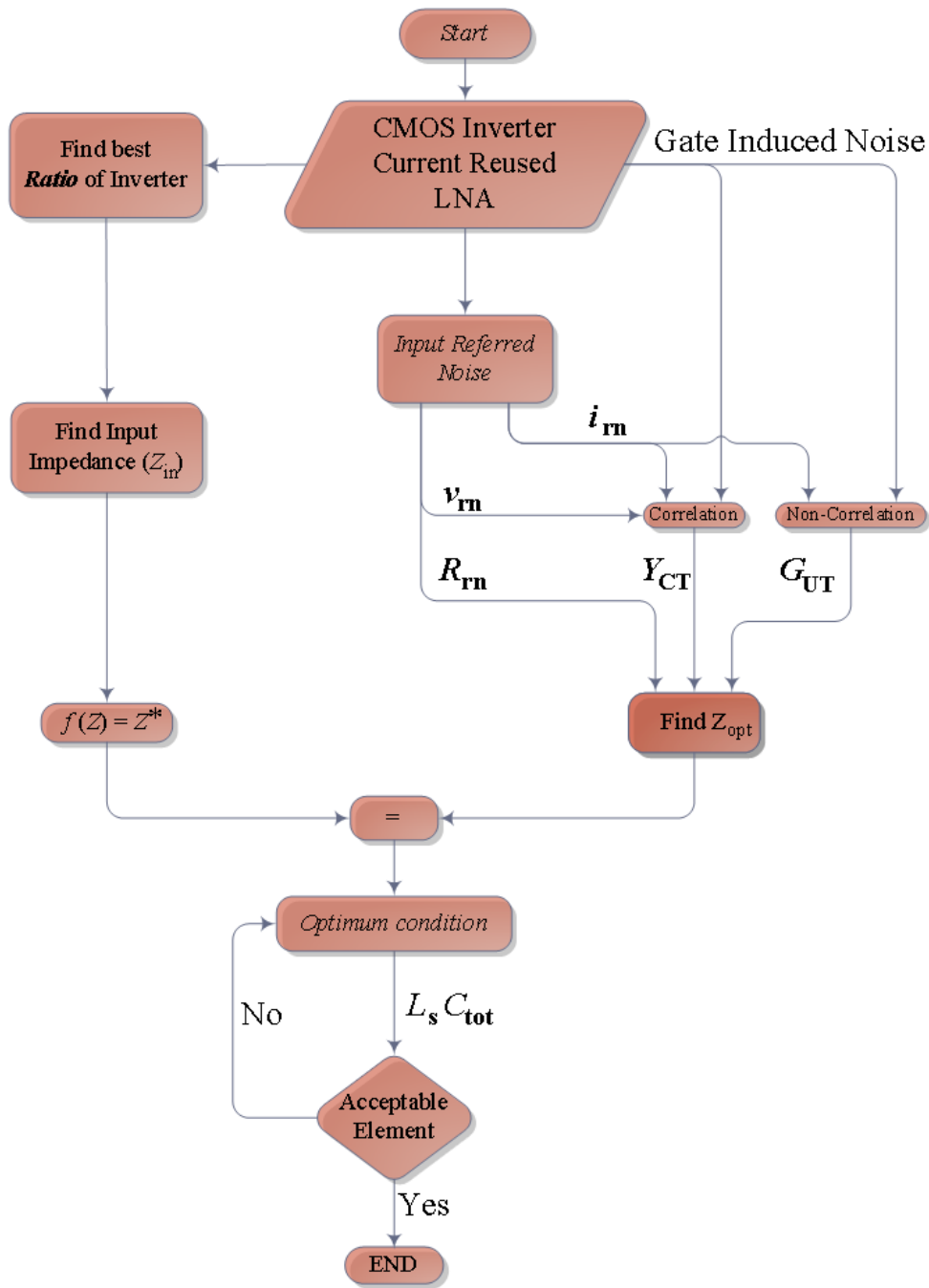


Figure 3.1: Flowchart of CICR Optimization.

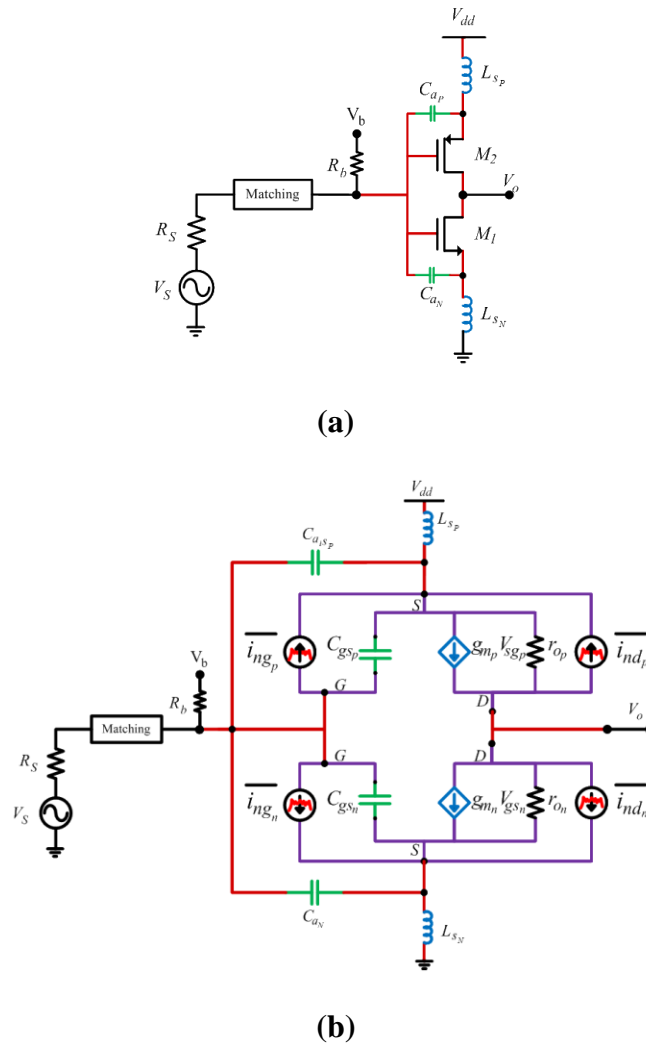


Figure 3.2: (a) Schematic of a CICR LNA, (b) Small signal equivalent circuit with noise sources.

3.1 Analytical Approach

To provide the essential background of CICR optimization, a theoretical procedure must be considered preliminarily. For this reason, the optimization procedure is explained as a flowchart (Figure 3.1). As can be seen, the first step in designing the CICR LNA is calculating the optimal size for inverter's transistors. This procedure leads to obtaining input impedance matching condition. Analysis of minimum noise figure then can provide the other essential

criteria for LNA's optimization. The Figure 3.2 depicts the schematic of a CICR LNA and its equivalent small circuit model including channel thermal noise sources ($\overline{i_{nd_n}^2}$ and $\overline{i_{nd_p}^2}$), the gate induced noise sources ($\overline{i_{ng_n}^2}$ and $\overline{i_{ng_p}^2}$), determined by Eqs. 2.9 and 2.10, respectively. The correlation coefficient (c) of the channel thermal and gate induced noise sources were defined as Eq. 2.44. In the suggested mathematical approach, the transistors' size, degeneration inductors (L_S), and gate source compensator capacitors (C_{a_n} and C_{a_p}) values are estimated.

3.1.1.1 Transistors' Size and CICR gain

Calculating the size of transistor in CMOS inverter offers an assumption that simplifies the complicated relationship between noise parameters and circuit elements, therefore, serves as an essential requirement to establish the final practical formulas. The drain current (I_{DS}) and drain-source saturation voltage (V_{Dsat_N}) of NMOS are given in Eqs. 3.1 and 3.2, respectively [46].

$$I_{DS} = \frac{\mu_N C_{ox}}{2 \left(1 + \frac{V_{OD_N}}{\varepsilon_{C_N} L_N} \right)} \left(\frac{W}{L} \right)_N V_{OD_N}^2 \quad 3.1$$

$$V_{Dsat_N} = \varepsilon_{C_N} L_N \left(\sqrt{1 + \frac{2V_{OD_N}}{\varepsilon_{C_N} L_N}} - 1 \right) \quad 3.2$$

where W and L are the channel width and length, respectively. C_{ox} is the gate oxide capacitance per unit area, and it is related to the oxide thickness T_{ox} by $C_{ox} = \varepsilon_{ox}/T_{ox}$. V_{OD_N} is the overdrive voltage and equals to $V_{OD} = V_{GS} - V_{th}$. After some manipulations one obtains:

$$I_{DS} = \frac{\mu_N C_{ox}}{2 \left[V_{Dsat_N}^2 - 2V_{ot_N} (V_{OD_N} - V_{Dsat_N}) \right]} \left(\frac{W}{L} \right)_N \frac{V_{OD_N}^2}{V_{Dsat_N}^2} \quad 3.3$$

Table 3.1: Technology dependent variables' value.

Variable	Mean Value			
	Total	$\Re = 2.5$	$\Re = 2.7$	$\Re = 3$
$\varepsilon_{C_N} L_N$	0.2654	0.2711	0.2661	0.2589
$\varepsilon_{C_P} L_P$	1.3926	1.4035	1.3937	1.3805
$\mu_N C_{ox} / 2L_N$	3363.0	3236.1	3351.3	3501.5
$\mu_P C_{ox} / 2L_P$	748.45	779.4750	754.2721	717.5927
V_{Dsat_N}	0.1404	0.1397	0.1403	0.1411
$ V_{Dsat_P} $	0.2024	0.2024	0.2024	0.2024
V_{th_N}	0.4224	0.4242	0.4226	0.4204
$ V_{th_P} $	0.4123	0.4122	0.4123	0.4124
g_{m_N} / g_{m_P}	1.0362	1.0630	1.0391	1.0065
$C_{gs_N} (fF)$	48.010	47.997	48.009	48.024
$C_{gs_P} (fF)$	116.99	106.69	115.56	128.42
$C_{gd_N} (fF)$	16.481	16.539	16.496	16.409
$C_{gd_P} (fF)$	42.851	38.404	42.223	47.927
C_{gs_N} / C_{gd_N}	2.9145	2.9033	2.9118	2.9285
C_{gs_P} / C_{gd_P}	2.7299	2.7791	2.7336	2.6770
C_{gs_P} / C_{gs_N}	2.4355	2.2279	2.4056	2.6729

Since both transistors operate at saturation region with the same current ($I_{DS_N} = I_{SD_P}$), equal biasing voltage ($V_{gs_N} = V_{sg_P} = V_{DD}/2$), and the drain current (I_{DS}) and drain-source of NMOS is given in Eq. 3.3, the inverter ratio would be defined as in Eq. 3.4.

$$\mathfrak{R} = \frac{W_P}{W_N} = \frac{\mu_P}{\mu_N} \frac{V_{Dsat_N}^2 + 2|V_{ot_P}(V_{OD_P} - V_{Dsat_P})|}{V_{Dsat_N}^2 + 2V_{ot_N}(V_{OD_N} - V_{Dsat_N})} \frac{V_{Dsat_N}^2 V_{OD_N}^2}{V_{Dsat_P}^2 V_{OD_P}^2} \quad 3.4$$

Due to the fact that the calculations of technology dependent constants lead to inaccurate values, we utilized the simulator's features to gain more precise values. Table 3.1 provides the details about the technology dependent variables which are required for the optimization numerical calculations. As a result, the optimum value of 2.7 for the ratio is attained by extracting the V_{OD} and V_{Dsat} directly from the simulator. In the best ratio NMOS and PMOS transistors operate almost equally in term of amplification and possess the same transconductance as in Eq. 3.5.

$$\frac{g_{m_n}}{g_{m_p}} = \frac{I_{DS_n}}{2V_{OD_n}} \times \frac{2V_{OD_p}}{I_{SD_p}} \approx 1 \quad 3.5$$

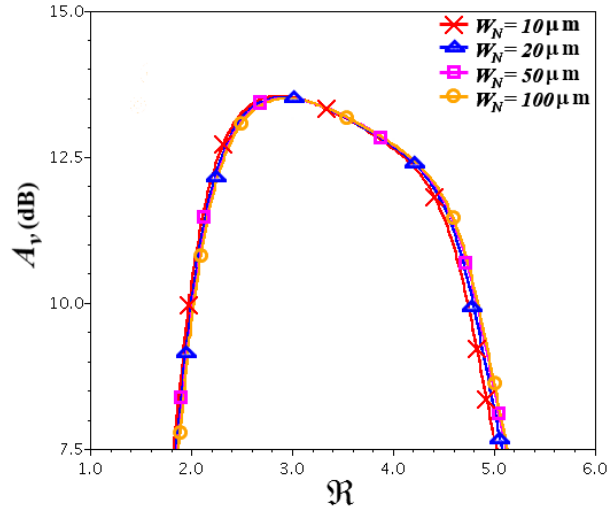


Figure 3.3: The CICR's forward gain in low frequency versus the ratio of inverter.

In determining the channel capacitances, C_{gs} , we should consider that if the thickness of oxide is assumed to be equaled for both of the PMOS and NMOS ($T_{ox_N} \approx T_{ox_P}$), the below equation could be driven:

$$\begin{cases} C_{gs_N} = \frac{2}{3} C'_{ox} (WL)_N \\ C_{gs_P} = \frac{2}{3} C'_{ox} (WL)_P \end{cases} \Rightarrow \frac{C_{gs_P}}{C_{gs_N}} = \frac{W_P}{W_N} = \mathfrak{R} \quad 3.6$$

Based on the assumptions and the equivalent circuit of Figure 3.2.b, the low frequency voltage gain is obtained as:

$$A_v = \frac{V_o}{V_{in}} = -g_m (r_{o_n} \parallel r_{o_p}) \quad 3.7$$

where g_m equals to summation of g_{m_N} and g_{m_P} . The relevance between the CICR's forward gain and the ratio of transistors is illustrated in Figure 3.3. It proves that that the $A_{v,max}$ occurs at calculated ratio from Eq. 3.4. In addition, the gain curves are extracted for a wide range of transistors' width. These results demonstrate the independency of optimum \mathfrak{R} to the size of the transistors. The input impedance of CICR can be expressed as:

$$Z_{in} \approx Z_{in_n} \parallel Z_{in_p} \quad 3.8$$

where Z_{in_n} and Z_{in_p} represent the input impedance of NMOS and PMOS transistors, respectively.

$$Z_{in_n} = L_s s + \frac{1}{\xi C_{tot} s} + \frac{g_{m_n} L_s}{\xi C_{tot}} \quad 3.9$$

$$Z_{in_p} = L_s s + \frac{1}{(1-\xi) C_{tot} s} + \frac{g_{m_p} L_s}{(1-\xi) C_{tot}} \quad 3.10$$

C_{tot} is the accumulation of the gate-source's parallel capacitors ($C_{tot} = C_{gs_n} + C_{gs_p} + C_{a_n} + C_{a_p}$).

$$(1-\xi)C_{tot} = C_{gs_p} + C_{a_p} \quad 3.11$$

$$\xi C_{tot} = C_{gs_n} + C_{a_n} \quad 3.12$$

C_{a_n} and C_{a_p} represent the gate-source compensator capacitors for NMOS and PMOS transistors, respectively. The ξ is the proportion ratio constant and $0 < \xi < 1$. In order to have better matching at input and decrease the input reflection (S_{11}), the Z_{in} can be minimized one step before starting actual optimization which is one of the advantage of this method. To do so, we can adjust ξ . The size of capacitors and inductors is lifted as freedom for the noise optimization calculations. Therefore, the optimum Z_{in} is achieved by $\xi = 1/2$. By substituting this condition and Eq. 3.5 into the Eq. 3.8, we have:

$$Z_{in} \approx \frac{L_s s}{2} + \frac{1}{C_{tot} s} + \frac{g_{m_n} L_s}{C_{tot}} \quad 3.13$$

The new condition guarantees the equivalency of input impedance of both transistors.

3.1.1.2 Noise Parameters

From the Eq. 2.43, the noise factor of CICR LNA can be described as:

$$F = \frac{\overline{i_{ns}^2} + \left| i_m + i_{ng_n} + i_{ng_p} + Y_s v_m \right|^2}{\overline{i_{ns}^2}} \quad 3.14$$

where $\overline{i_{nr}^2}$ and $\overline{v_{nr}^2}$ are the power of input referred noise as current and voltage which obtained from the open and short circuit analysis, respectively. The $\overline{i_{ns}^2}$ is attributed to the thermal noise of the source resistance R_s and Y_s represent source admittance. The referred noise as voltage source to the input of a CS amplifier with degeneration inductor is calculated from the short input test which results:

$$\overline{v_{o_n,SC1}^2} = \frac{R_d^2 r_o^2}{(R_d + r_o + L_S s(1 + g_m r_o))} \overline{i_{nd}^2} \quad 3.15$$

In case a voltage noise source is available at input, the output would be:

$$\overline{v_{o_n1}^2} = \frac{R_d^2 r_o^2}{(R_d + r_o + L_S s(1 + g_m r_o))} g_m^2 \overline{v_n^2} \quad 3.16$$

Now, putting the Eq. 3.14 equals to Eq. 3.15 result in the input referred noise as voltage.

$$\overline{v_{o_n,SC1}^2} = \overline{v_{o_n1}^2} \Rightarrow \overline{v_n^2} = \frac{1}{g_m^2} \overline{i_{nd}^2} \quad 3.17$$

The procedure of attaining the referred noise as current source is similar to the voltage ones except the open circuit at input instead of short circuit test.

$$\overline{v_{o_n,OC2}^2} = (r_o \parallel sL_S)^2 \overline{i_{nd}^2} \quad 3.18$$

In case of a current noise source is available at input, the output would be:

$$\overline{v_{o_n2}^2} = \frac{(r_o \parallel sL_S)^2 g_m^2}{\omega^2 C_{gs}^2} \overline{i_{n1}^2} \quad 3.19$$

Comparing the Eq. 3.18 and Eq. 3.19 results in the input referred noise as current.

$$\overline{i_{nd}^2} = \frac{g_m^2}{\omega^2 C_{gs}^2} \overline{i_{n1}^2} \quad 3.20$$

Based on the assumption in previous section, the Eq. 3.17 and Eq. 3.20 can be extended and applied to CICR LNA. Therefore:

$$\overline{v_m^2} = \frac{1}{g_m^2} (\overline{i_{nd_n}^2} + \overline{i_{nd_p}^2}) \quad 3.21$$

$$\overline{i_m^2} = \omega^2 C_{tot}^2 \overline{v_m^2} = \frac{\omega^2 C_{tot}^2}{g_m^2} (\overline{i_{nd_n}^2} + \overline{i_{nd_p}^2}) \quad 3.22$$

By considering the traditional equivalent noise resistance (Eq. 2.51), the R_m is attained as:

$$\begin{aligned}
R_m &= \frac{\overline{v_m^2}}{4kT\Delta f} = \frac{1}{4kT\Delta f} \frac{(\overline{i_{nd_n}^2} + \overline{i_{nd_p}^2})}{g_m^2} \\
&= \frac{(4kT\gamma g_{d0_n}\Delta f + 4kT\gamma g_{d0_p}\Delta f)}{(g_{m_n} + g_{m_p})^2} = \frac{\gamma(g_{d0_n} + g_{d0_p})}{(g_{m_n} + g_{m_p})^2}
\end{aligned} \tag{3.23}$$

In the weak inversion we have:

$$\frac{g_{d0_n}}{g_{m_n}} \approx \frac{g_{d0_p}}{g_{m_p}} \approx \frac{1}{\alpha} \tag{3.24}$$

where the constant of α is defined as g_{d0}/g_m , and equals to 1 for long channel devices, and it is same for both NMOS and PMOS transistors. The channel scaling down directly decreases the α . For any sets of 4 real number which:

$$\frac{a}{b} = \frac{c}{d} \tag{3.25}$$

the following equality is given

$$\frac{a}{b} = \frac{c}{d} = \frac{a+c}{b+d} \tag{3.26}$$

Substituting Eq. 3.24 and Eq. 3.26 in Eq. 3.23 results:

$$R_m = \frac{\gamma}{g_m} \frac{(g_{d0_n} + g_{d0_p})}{(g_{m_n} + g_{m_p})} \approx \frac{\gamma}{\alpha g_m} \tag{3.27}$$

The correlation admittance, Y_{c_r} , can be expressed as:

$$Y_{c_r} = \frac{i_m + i_{ngc_n} + i_{ngc_p}}{v_m} = j\omega C_{tot} + g_m \frac{i_{ngc_n} + i_{ngc_p}}{i_{nd_n} + i_{nd_p}} \tag{3.28}$$

In order to apply more simplification to the Y_{c_r} , the correlation relation between noise sources should be considered precisely.

$$\begin{aligned}
\frac{i_{ngc_n} + i_{ngc_p}}{i_{nd_n} + i_{nd_p}} &= \theta \frac{i_{ngc_n} + i_{ngc_p}}{i_{nd_n} + i_{nd_p}} \frac{i_{nd_n}^*}{i_{nd_n}^*} + (1-\theta) \frac{i_{ngc_n} + i_{ngc_p}}{i_{nd_n} + i_{nd_p}} \frac{i_{nd_p}^*}{i_{nd_p}^*} \\
&= \theta \frac{i_{ngc_n} i_{nd_n}^* + i_{ngc_p} i_{nd_n}^*}{i_{nd_n} i_{nd_n}^* + i_{nd_p} i_{nd_n}^*} + (1-\theta) \frac{i_{ngc_n} i_{nd_p}^* + i_{ngc_p} i_{nd_p}^*}{i_{nd_n} i_{nd_p}^* + i_{nd_p} i_{nd_p}^*}
\end{aligned} \tag{3.29}$$

The correlation between all the possible pairs of CICR's noise sources is zero except those that belong to the same transistor (Eq. 20).

$$\begin{cases}
\text{Corr}(\overline{i_{nd_n}}, \overline{i_{nd_p}}) = 0 & \text{and} & \text{Corr}(\overline{i_{ng_n}}, \overline{i_{ng_p}}) = 0 \\
\text{Corr}(\overline{i_{ng_n}}, \overline{i_{nd_p}}) = 0 & \text{and} & \text{Corr}(\overline{i_{ng_p}}, \overline{i_{nd_n}}) = 0 \\
\text{Corr}(\overline{i_{ng_n}}, \overline{i_{nd_n}}) = c & \text{and} & \text{Corr}(\overline{i_{ng_p}}, \overline{i_{nd_p}}) = c
\end{cases} \tag{3.30}$$

By applying Eq. 3.30 to Eq. 3.29, we have:

$$\frac{i_{ngc_n} + i_{ngc_p}}{i_{nd_n} + i_{nd_p}} = \theta \frac{i_{ngc_n} i_{nd_n}^* + 0}{i_{nd_n} i_{nd_n}^* + 0} + (1-\theta) \frac{0 + i_{ngc_p} i_{nd_p}^*}{0 + i_{nd_p} i_{nd_p}^*} \tag{3.31}$$

which can be rewrite as:

$$\begin{aligned}
\frac{\overline{i_{ngc_n} + i_{ngc_p}}}{\overline{i_{nd_n} + i_{nd_p}}} &= \theta \frac{\overline{i_{ng_n} i_{nd_n}^*}}{i_{nd_n}^2} + (1-\theta) \frac{\overline{i_{ng_p} i_{nd_p}^*}}{i_{nd_p}^2} \\
&= \theta \frac{\overline{i_{ng_n} i_{nd_n}^*}}{i_{nd_n}^2} \frac{\sqrt{i_{ng_n}^2}}{\sqrt{i_{ng_n}^2}} + (1-\theta) \frac{\overline{i_{ng_p} i_{nd_p}^*}}{i_{nd_p}^2} \frac{\sqrt{i_{ng_p}^2}}{\sqrt{i_{ng_p}^2}}
\end{aligned} \tag{3.32}$$

More simplification will be done by substituting Eq. 2.44 in Eq. 3.32:

$$\frac{\overline{i_{ngc_n} + i_{ngc_p}}}{\overline{i_{nd_n} + i_{nd_p}}} = \theta c \sqrt{\frac{\delta\omega^2 C_{gs_n}^2}{5\gamma g_{d0_n}^2}} + (1-\theta) c \sqrt{\frac{\delta\omega^2 C_{gs_p}^2}{5\gamma g_{d0_p}^2}} \tag{3.33}$$

where θ is the constant and equals to $1/2$. Thus, Eq. 3.28 will be:

$$Y_{c_T} = 0 + j\omega C_{tot} \left\{ 1 + \alpha |c| \sqrt{\frac{\delta}{5\gamma}} \frac{C_{gs_n} + C_{gs_p}}{C_{tot}} \right\} \quad 3.34$$

By considering the basic explanation for the equivalent noise conductance (Eq. 2.52), the total uncorrelated conductance (G_{u_T}) is calculated as follow:

$$\overline{i_{ng}^2} = \overline{i_{ng_n}^2} + \overline{i_{ng_p}^2} = (\overline{i_{ng_n}^2} + \overline{i_{ng_p}^2})|c|^2 + (\overline{i_{ng_n}^2} + \overline{i_{ng_p}^2})(1-|c|^2) \quad 3.35$$

which the second term represents the un-correlated part of gate noise ($\overline{i_{ngu}^2}$).

$$\begin{aligned} G_{u_T} &= \frac{\overline{i_{ngu}^2}}{4kT\Delta f} = \frac{(\overline{i_{ng_n}^2} + \overline{i_{ng_p}^2})(1-|c|^2)}{4kT\Delta f} \\ &\Rightarrow G_{u_T} = \frac{\delta\omega^2}{5} \left(\frac{C_{gs_n}^2}{g_{d0n}} + \frac{C_{gs_p}^2}{g_{d0p}} \right) (1-|c|^2) \end{aligned} \quad 3.36$$

Based on the details that provided in Table 3.1 and the relation between C_{gs_n} and C_{gs_p} , it can be concluded:

$$2(C_{gs_n}^2 + C_{gs_p}^2) \approx (C_{gs_n} + C_{gs_p})^2 \text{ for } 2 \leq \mathfrak{R} \leq 3 \quad 3.37$$

Substituting Eq. 3.37 into Eq. 3.36, we have:

$$G_{u_T} = \frac{\delta\omega^2}{5} \frac{(C_{gs_n} + C_{gs_p})^2}{g_{d0n} + g_{d0p}} (1-|c|^2) \quad 3.38$$

According to the above results one can rewrite Eq. 3.14 as:

$$F = 1 + \frac{G_{u_T} + |Y_{c_T} + Y_s|^2 R_m}{Y_s} \quad 3.39$$

3.1.1.3 Minimum Noise Figure

Based on the parameters derived in previous sections and Eq. 2.62, the minimum noise figure of CICR can be attained as:

$$F_{\min} = 1 + 2R_m G_{opt} \approx 1 + (1 + \Re) \frac{\omega}{\omega_T} \sqrt{\frac{\gamma\delta}{5} (1 - |c|^2)} \quad 3.40$$

where:

$$G_{opt} = \alpha\omega \left[\delta/5\gamma (1 - |c|^2) \right]^{0.5} (C_{gs_n} + C_{gs_p}) \quad 3.41$$

As a result, Z_{opt} is found to be:

$$Z_{opt} = (G_{opt} + Y_{c_r}^*)^{-1} = \frac{1}{\omega C_{gs_n} (1 + \Re)} \frac{\alpha \sqrt{\frac{\delta}{5\gamma} (1 - |c|^2)} + j \left\{ \frac{C_{tot}}{C_{gs_n} + C_{gs_p}} + \alpha |c| \sqrt{\frac{\delta}{5\gamma}} \right\}}{\left\{ \frac{\alpha^2 \delta}{5\gamma} (1 - |c|^2) + \left[\frac{C_{tot}}{C_{gs_n} + C_{gs_p}} + \alpha |c| \sqrt{\frac{\delta}{5\gamma}} \right]^2 \right\}} \quad 3.42$$

Based on the section 2.4.4 discussions, the optimization condition, $Z_{opt} = Z_{in}^*$, require to observe:

$$\Re\{Z_{opt}\} = \Re\{Z_{in}\} \quad 3.43$$

After some calculation one obtains:

$$L_s C_{tot} \approx \frac{2\alpha C_{gs_n} (1 + \Re) \sqrt{\frac{\delta}{5\gamma} (1 - |c|^2)}}{\omega g_m} \quad 3.44$$

As discussed in chapter 2, Eq. 3.44 represents the essential condition for designing optimum LNA. In the next section, this criteria is applied for the designing the CICR LNA.

3.2 Simulation and Discussion

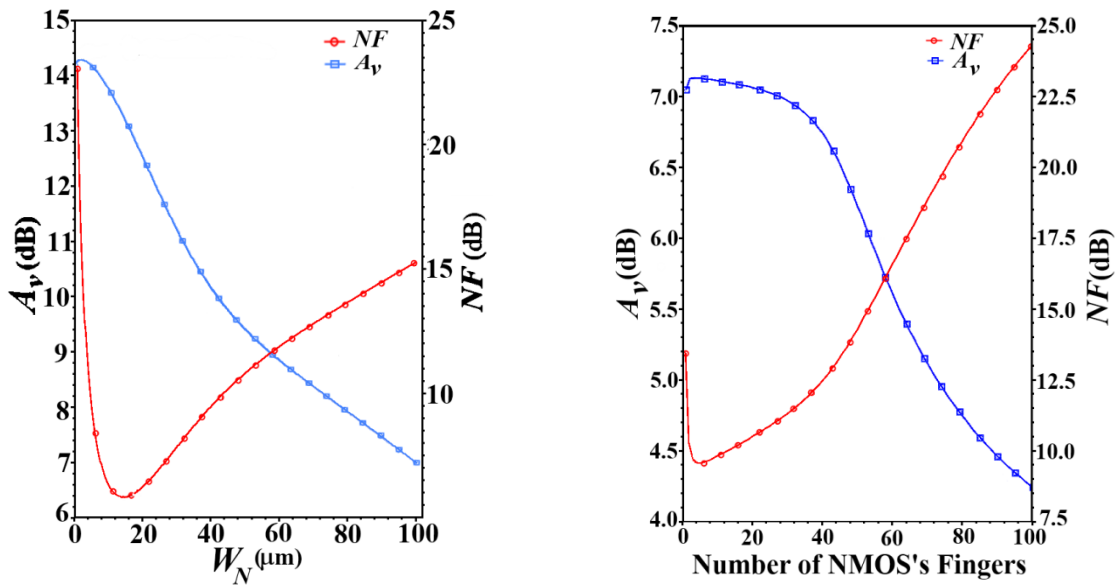
3.2.1 Noise Figure and Transistor's Size

Considering the fact that no analytical procedure could reasonably approximate the optimum value for transistor size and number of fingers, in this part we deduce their values through numerical investigation. Figure 3.4.a demonstrates that NMOS optimum size should be 14.5 μm . Despite of common belief, the multi-fingered transistors demonstrate better NF than a single transistor with the same equal width. Figure 3.4.b indicates that by increasing the number of fingers per transistor to 4, NF is significantly decreased. Figure 3.4.b depicts the optimum transistor size and number of fingers for each of NMOS and PMOS can be derived. It is necessary to remind that number of fingers for PMOS should be extracted from NMOS ones by applying the ratio factor.

The next point is the value of biasing voltage. As mentioned in Section I, the gate voltage of transistors should be pulled up to $V_{dd}/2$, due to the equivalency considered for inverter pair at the optimum ratio. Figure 3.4.c illustrates both the NF_{\min} and $A_{v,\max}$ can be achieved when V_b equals to 0.6 V for the ratio between 2 to 3.

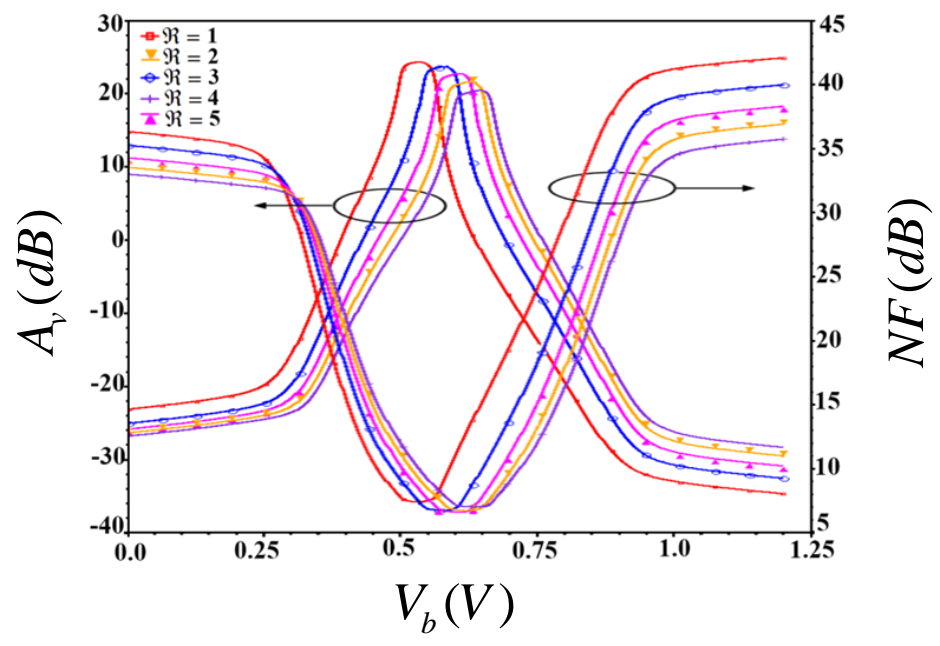
3.2.1.1 CICR's Optimized Noise Figure

By utilizing the optimum values obtained in Section 03.1, both L_s and C_{tot} are found by Eq. 3.44. The operation frequency is 2.4GHz which is intended for WBAN applications. Figure 3.5.a depicts the NF and forward gain variations with L_s , in different C_{tot} . It can be inferred from the plots, NF_{\min} occurs at higher L_s and lower C_{tot} , indicated by dashed line. However, as the source inductors cannot take arbitrary large values due to the area limitation, we restrict it to 10nH. Therefore, the size of compensator capacitances will be found by substituting the L_s value in Eq. 3.44. Figure 3.5.b depicts that the optimum C_{tot} value is adequately close to the designed one. This small mismatching is caused by the primary assumption that neglects the drain-source parasitic capacitances.



(a)

(b)



(c)

Figure 3.4: Variation of A_v and NF as function of: (a) transistor width, (b) number of fingers, (c) DC biasing.

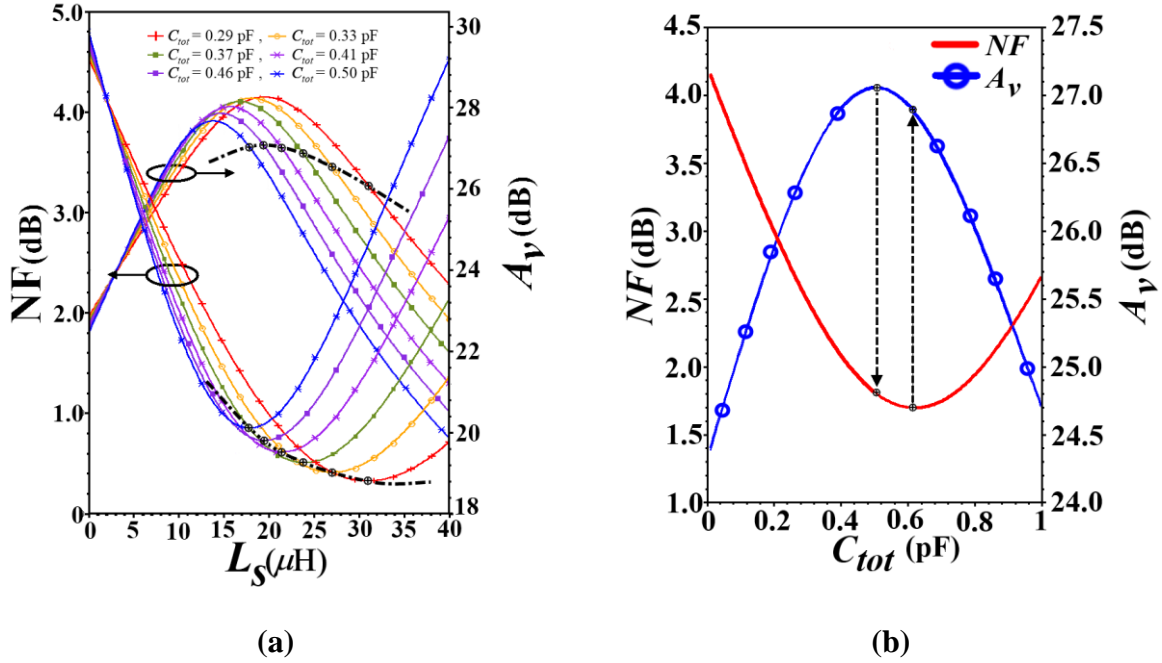


Figure 3.5: Variation of A_v and NF as function of: (a) degeneration inductors, (b) compensation capacitors.

This set of parameters' values result in 1.69dB for NF, 27dB for A_v , and -9.14dB for S_{11} . To improve these values that are extracted without employing any matching network, we suggest a very small L matching at the LNA input. Therefore, this design will be more compact compared with the previous ones that utilized the gate inductor (L_g). Using this approach, S_{11} and A_v improve to -18.6dB and 28, respectively, although NF increases to 2.46dB (Figure 3.6.a). Figure 3.6.b represents the third-order intercept point (IIP3) of LNA which is equal to -10.1 dBm.

3.2.1.2 Process, Power Supply, and Temperature Variation Monitoring

To clarify the reliability of our optimization method and guarantee fabrication of designed CICR LNA, the process, supply voltage, and temperature (PVT) variation monitoring was applied. The test were done within 45 different states, which include all the five possible

CMOS process variations (f_f , f_s , s_f , s_s , and t_t), $\pm 10\%$ fluctuation in power supply, and temperature variation between -27 to 100°C (Figure 3.7). The PVT test results are shown in

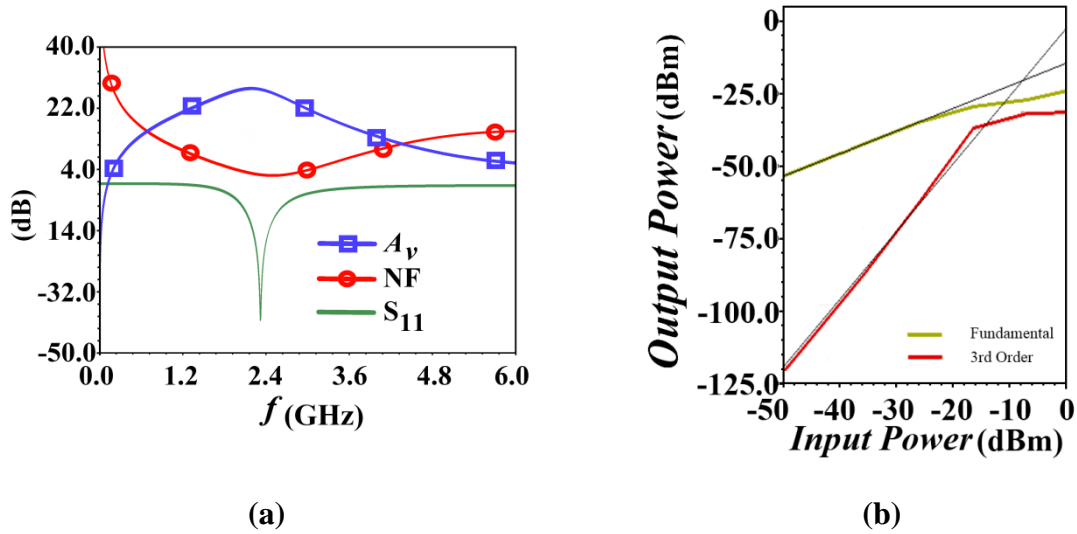


Figure 3.6: CICR LNA with L matching at input results: (a) Forward gain, Noise Figure, and input reflection, (b) third-order intercept point (IIP3).

Table 3.2, reveal that the designed LNA insignificantly affected which indicated robustness of this design to the PVT variation. Besides, as depicted in Figure 3.7, the proposed LNA based on the CICR optimization method is always tracking the best possible gain, NF, and input matching. In other words, the optimization provides a mechanism which the best achievable performance of design at the desirable frequency.

Table 3.2: PVT Test Result at 2.4 GHz

	A_v (dB)	NF (dB)
Min	25.9	1.93
Max	28.5	3.27

3.3 Summery

To summarize, this chapter sparked off a novel technique of LNA noise optimization by introducing a CMOC inverter current reused architecture and suggested a powerful mathematical

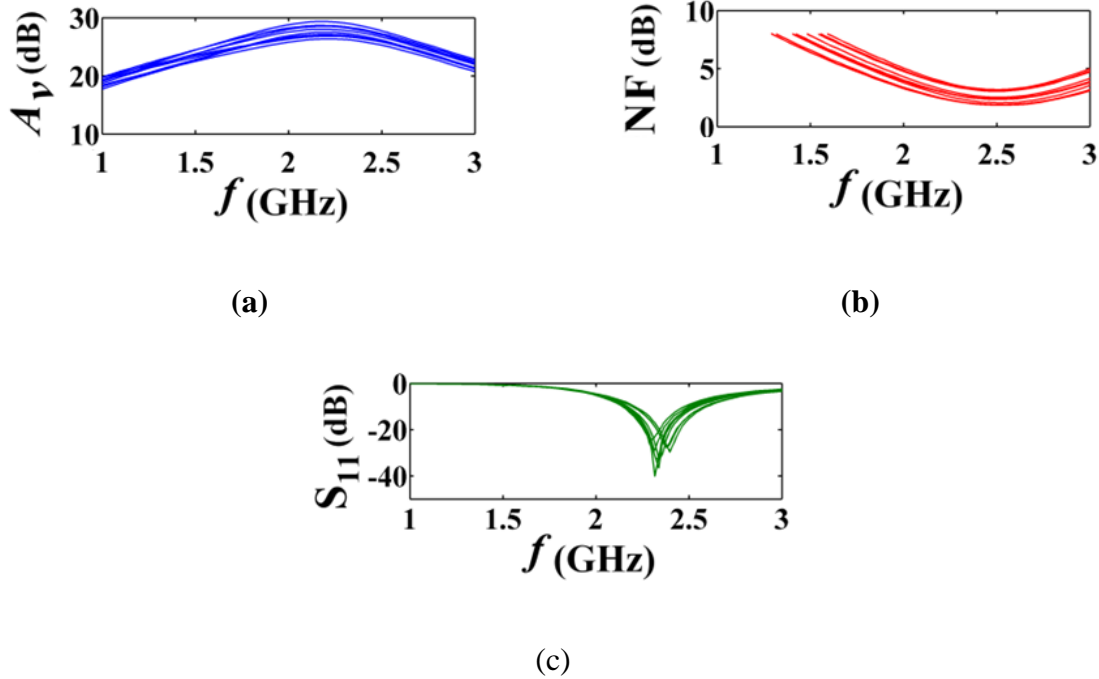


Figure 3.7: PVT test results, (a) voltage gain, (b) noise figure, (c) input matching (S_{11}).

foundation that excelled from all previous ones at precise prediction and achievements. A huge load of calculation, eight times greater than the precedent methods which all focused on one transistor optimization, was required to take to account all the noise sources, including the both transistors at the same time in addition to their sizes' ratio. This mainly is due to the fact that all the parameters such as gain, input matching, and power are associated with the transistors width' ratio. Besides, there are two inductors and two capacitors to be optimized which are twice the numbers of elements in the preceding techniques. Considering all together, it can be conclude that the difficulty and the amount of the computations of the presented method will be about eight times compared to the former ones like PCSNIM. As a result, we could achieve the LNA design with as high gain as 27dB, as well as a low noise figure of 1.69dB. The analytical procedure included determining the transistor size, noise parameters, and minimum noise figure are fully discussed in this chapter and the multifaceted simulation results completely elaborates the performance.

Chapter 4

Feedback and Nonlinearity

4.1 Introduction

The input to output transfer function of a circuit with the linear elements and feedbacks could be simply presented based on the linear feedback theory. This method covers the circuit with the memory effect. It is also applicable for the circuit with the first degree of nonlinearity effects. As it discussed in Section 2.6.1, the power series should be employed for this case with some assumptions. However, in the case of circuits with third and higher nonlinearity effects as well as the memory ones this method sounds ineffective. Thus, it's required an alternative means for this type of calculations: The Volterra nonlinear elements, memory effects, and feedbacks [73]. Working with multi excitations' input is the most significant point about the Volterra series. In other words, the Volterra kernels which is also known as the multi-dimensional Fourier transfer function give us opportunity to work with multi tones input as well as the produced intermodulation (IM) terms.

This chapter will mostly discuss around the nonlinear effects over the circuit with negative feedback and memory effects. While Section 4.2 is assigned to Volterra series calculation, an extensive comparison between these results and power series' ones is presented in Section 0. To keep the simplicity of this chapter and reduce the weight of mathematical equations, a well-organized tutorial for Volterra series is presented at Appendix A.

4.2 Nonlinear Analyses of Feedback

Based on the proposed steps in Appendix A (Figure A.2), Figure 4.1 depicts the block diagram of typical CMOS LNA with the negative feedback. The backward block, $\beta(\omega)$, represents a feedback with memory effects. It's usually presented in term of either a band pass (BPF) or high pass (HPF) filter. The main transistor, M_{Main} , is modeled by forward block, while $f(u)$ represents the nonlinearity behaviors of its transconductance.

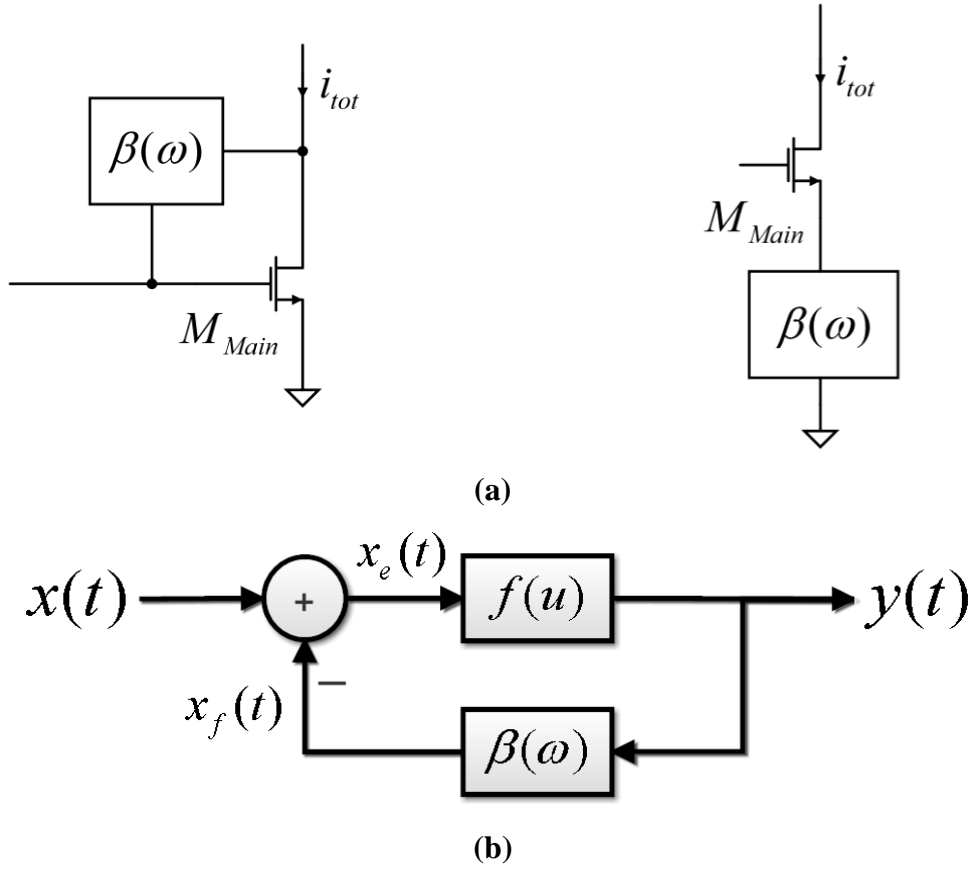


Figure 4.1: Typical CMOS LNA with negative feedback: (a) schematics' presentation, (b) equivalent block diagram.

$$f(u) = g_1 u + g_2 u^2 + \dots + g_n u^n = \sum_{m_f=1}^{N_f} g_{m_f} u^{m_f} \quad 4.1$$

where g_i represents the i th-order derivative of drain-source current which widely discussed in Section 2.6.2. For the CS LNA circuit, $x(t)$ and $y(t)$ identify the input voltage and output current and are defined by Eq. A.3 and A.5, respectively. In this manner, the source voltage and gate-source one is specified by $x_f(t)$ and $x_e(t)$, respectively, and are defined as follow:

$$x_f(t) = \beta(\omega)y(t) \quad 4.2$$

$$x_e(t) = x(t) - x_f(t) \quad 4.3$$

Substituting Eq. 4.2 and 4.3 in Eq. 4.1, we have:

$$y(t) = \sum_{m_f=1}^{N_f} g_{m_f} (x(t) - \beta(\omega)y(t))^{m_f} \quad 4.4$$

Up to this point, the mathematical relation between the input and output has been formulated from the block diagram of circuit. The Volterra kernels will be calculated in the next steps.

4.2.1 Volterra kernels

Considering the output formula, the volterra kernels could be extracted from Eq. A.11 and A.12 when the circuit is excited by a single frequency, ω_1 .

$$x(t) = \frac{1}{2} \sum_{q_1=1}^1 X_{q_1} \exp(j\omega_{q_1} t) = \exp(j\omega_1 t) \quad 4.5$$

Applying Eq. A.5 and 4.5 into Eq. 4.4 and eliminating the higher order terms, we would have:

$$y_1(t) + \overbrace{\sum_{n=2}^N y_n(t)}^0 = g_1 \left[x(t) - \beta(\omega) \left(y_1(t) + \overbrace{\sum_{n=2}^N y_n(t)}^0 \right) \right] + \overbrace{\sum_{m_f=2}^{N_f} g_{m_f} (x(t) - \beta(\omega)y(t))^{m_f}}^0 \quad 4.6$$

$$y_1(t) = g_1 [x(t) - \beta(\omega)y_1(t)] \quad 4.7$$

Eq. 4.7 represents the linear case of the circuit. Thus, the first kernel is extracted by applying Eq. A.10 into Eq. 4.7 as:

$$\begin{aligned} \frac{1}{2} \sum_{q_1=1}^1 X_{q_1} H_1(\omega_{q_1}) \exp(j\omega_{q_1} t) &= g_1 \left[\exp(j\omega_1 t) - \frac{1}{2} \sum_{q_1=1}^1 X_{q_1} \beta(\omega_{q_1}) H_1(\omega_{q_1}) \exp(j\omega_{q_1} t) \right] \\ \Rightarrow H_1(\omega_1) &= \frac{g_1}{1 + g_1 \beta(\omega_1)} \end{aligned} \quad 4.8$$

After calculation of the first order term, the second order kernel calculation could be started by increasing the number of excitations to two tones (ω_1, ω_2).

$$x(t) = \frac{1}{2} \sum_{q_1=1}^2 X_{q_1} \exp(j\omega_{q_1} t) = \exp(j\omega_1 t) + \exp(j\omega_2 t) \quad 4.9$$

Similar to the first order calculations, substituting Eq. A.5 and 4.9 into the circuit input to output function will result in:

$$\begin{aligned} \overbrace{y_1(t) + y_2(t) + \sum_{n=3}^N y_n(t)}^0 &= g_1 \left[\overbrace{x(t) - \beta(\omega)}^0 \left(\overbrace{y_1(t) + y_2(t) + \sum_{n=2}^N y_n(t)}^0 \right) \right] + \\ g_2 \left[\overbrace{x(t) - \beta(\omega)}^0 \left(\overbrace{y_1(t) + \sum_{n=2}^N y_n(t)}^0 \right) \right]^2 &+ \overbrace{\sum_{m_f=3}^{N_f} g_{m_f} (x(t) - \beta(\omega) y(t))^{m_f}}^0 \end{aligned} \quad 4.10$$

$$y_2(t)(1 + g_1\beta(\omega)) = g_2x^2(t) - 2g_2x(t)\beta(\omega)y_1(t) + g_2(\beta(\omega)y_1(t))^2 \quad 4.11$$

The Eq. 4.11 demonstrates only the terms which includes the second order harmonics. However, it still needs more purification in order to extract the exact terms which are function of just two different input tones. In the light of this statement, the terms in Eq. 4.11 are rewritten as follow:

$$\begin{aligned} \frac{1}{2^2} \sum_{q_1=1}^2 \sum_{q_2=1}^2 X_{q_1} X_{q_2} (1 + g_1\beta(\omega_{q_1} + \omega_{q_2})) H_2(\omega_{q_1}, \omega_{q_2}) \exp(j(\omega_{q_1} + \omega_{q_2})t) &= \\ + g_2 \left(\frac{1}{2} \sum_{q_1=1}^2 X_{q_1} \exp(j\omega_{q_1} t) \right) \left(\frac{1}{2} \sum_{q_2=1}^2 X_{q_2} \exp(j\omega_{q_2} t) \right) & \\ - 2g_2 \left(\frac{1}{2} \sum_{q_1=1}^2 X_{q_1} \exp(j\omega_{q_1} t) \right) \left(\frac{1}{2} \sum_{q_2=1}^2 X_{q_2} \beta(\omega_{q_2}) H_1(\omega_{q_2}) \exp(j\omega_{q_2} t) \right) & \\ + g_2 \left(\frac{1}{2} \sum_{q_1=1}^2 X_{q_1} \beta(\omega_{q_1}) H_1(\omega_{q_1}) \exp(j\omega_{q_1} t) \right) \left(\frac{1}{2} \sum_{q_2=1}^2 X_{q_2} \beta(\omega_{q_2}) H_1(\omega_{q_2}) \exp(j\omega_{q_2} t) \right) & \end{aligned} \quad 4.12$$

Applying the summations' order interchange methodology results in:

$$\begin{aligned}
& \sum_{q_1=1}^2 \sum_{q_2=1}^2 (1 + g_1 \beta(\omega_{q_1} + \omega_{q_2})) H_2(\omega_{q_1}, \omega_{q_2}) \exp(j(\omega_{q_1} + \omega_{q_2})t) = \\
& + g_2 \sum_{q_1=1}^2 \sum_{q_2=1}^2 \exp(j(\omega_{q_1} + \omega_{q_2})t) - 2g_2 \sum_{q_1=1}^2 \sum_{q_2=1}^2 \beta(\omega_{q_2}) H_1(\omega_{q_2}) \exp(j(\omega_{q_1} + \omega_{q_2})t) \quad 4.13 \\
& + g_2 \sum_{q_1=1}^2 \sum_{q_2=1}^2 \beta(\omega_{q_1}) H_1(\omega_{q_1}) \beta(\omega_{q_2}) H_1(\omega_{q_2}) \exp(j(\omega_{q_1} + \omega_{q_2})t)
\end{aligned}$$

By extracting the terms which includes ω_1 and ω_2 simultaneously we would have:

$$\begin{aligned}
2(1 + g_1 \beta(\omega_1 + \omega_2)) H_2(\omega_1, \omega_2) &= 2g_2 - 2g_2 [\beta(\omega_1) H_1(\omega_1) + \beta(\omega_2) H_1(\omega_2)] \\
&+ 2g_2 \beta(\omega_1) H_1(\omega_1) \beta(\omega_2) H_1(\omega_2) \quad 4.14
\end{aligned}$$

$$H_2(\omega_1, \omega_2) = \frac{g_2 \{1 - [\beta(\omega_1) H_1(\omega_1) + \beta(\omega_2) H_1(\omega_2)] + \beta(\omega_1) H_1(\omega_1) \beta(\omega_2) H_1(\omega_2)\}}{(1 + g_1 \beta(\omega_1 + \omega_2))} \quad 4.15$$

The Eq. 4.15 could be more simplified by substituting Eq. 4.8:

$$H_2(\omega_1, \omega_2) = \frac{g_2}{(1 + g_1 \beta(\omega_1 + \omega_2))(1 + g_1 \beta(\omega_1))(1 + g_1 \beta(\omega_2))} \quad 4.16$$

So far, the first and second kernels are calculated. As recursive flowchart (Figure A.2) indicates, all the essentials for the third order transfer function computation are provided.

$$x(t) = \frac{1}{2} \sum_{q_1=1}^3 X_{q_1} \exp(j\omega_{q_1} t) = \exp(j\omega_1 t) + \exp(j\omega_2 t) + \exp(j\omega_3 t) \quad 4.17$$

Hence, exciting circuit by three different tones (Eq. 4.17) and apply it to Eq. A.12 will result in:

$$\begin{aligned}
y_3(t) + \cancel{\dots} &= a_1 \left[\cancel{x(t)} - \beta(\omega) \left(y_3(t) + \cancel{\dots} \right) \right] + a_2 \left[x(t) - \beta(\omega) \left(y_1(t) + y_2(t) + \cancel{\dots} \right) \right]^2 \\
&+ a_3 \left[x(t) - \beta(\omega) \left(y_1(t) + \cancel{\dots} \right) \right]^3 + \cancel{\dots} \quad 4.18
\end{aligned}$$

Simplifying Eq. 4.18 and extracting only the third order terms yields:

$$\begin{aligned}
y_3(t)(1+g_1\beta(\omega)) &= -2g_2x(t)\beta(\omega)y_2(t) + 2g_2\beta(\omega)y_1(t)\beta(\omega)y_2(t) + g_3x^3(t) \\
&\quad - 3g_3x^2(t)\beta(\omega)y_1(t) + 3g_3x(t)(\beta(\omega)y_1(t))^2 - g_3(\beta(\omega)y_1(t))^3
\end{aligned} \tag{4.19}$$

As can be inferred from Eq. 4.19, the number of terms is increased compare to the first and second order equations. So, to keep tracking easier, we can calculate them separately:

$$\begin{aligned}
y_3(t)(1+g_1\beta(\omega))\Big|_{\omega_1, \omega_2, \omega_3} &= \frac{1}{2^3} \sum_{q_1=1}^3 \sum_{q_2=1}^3 \sum_{q_3=1}^3 \left[X_{q_1} X_{q_2} X_{q_3} \left(1 + g_1\beta(\omega_{q_1} + \omega_{q_2} + \omega_{q_3}) \right) \times \right. \\
&\quad \left. H_3(\omega_{q_1}, \omega_{q_2}, \omega_{q_3}) \exp(j(\omega_{q_1} + \omega_{q_2} + \omega_{q_3})t) \right] \\
&= 6(1+g_1\beta(\omega_1 + \omega_2 + \omega_3)) H_3(\omega_1, \omega_2, \omega_3) \exp(j(\omega_1 + \omega_2 + \omega_3)t)
\end{aligned} \tag{4.20}$$

The coefficient six is calculated by employing Eq. A.13 as:

$$t_{n,k} = \frac{3!}{1!1!1!} = 6 \tag{4.21}$$

In Eq. 4.19, for all the terms including a combination of the first and second order components, such as y_1 and y_2 , we could have the following distribution of frequencies:

$$\begin{array}{cccc}
y_1 & \omega_1 & \omega_2 & \omega_3 \\
y_2 & \omega_2, \omega_3 & \omega_1, \omega_3 & \omega_1, \omega_2
\end{array} \tag{4.22}$$

Eq. 4.22 is a great help for calculating the rest of the second terms in Eq. 4.19:

$$\begin{aligned}
&-2g_2x(t)\beta(\omega)y_2(t)\Big|_{\omega_1, \omega_2, \omega_3} = \\
&\quad -2g_2 \left[2\exp(j\omega_1t)\beta(\omega_2 + \omega_3)H_2(\omega_2, \omega_3)\exp(j(\omega_2 + \omega_3)t) \right. \\
&\quad \quad + 2\exp(j\omega_2t)\beta(\omega_1 + \omega_3)H_2(\omega_1, \omega_3)\exp(j(\omega_1 + \omega_3)t) \\
&\quad \quad \left. + 2\exp(j\omega_3t)\beta(\omega_1 + \omega_2)H_2(\omega_1, \omega_2)\exp(j(\omega_1 + \omega_2)t) \right] \\
&= -4g_2 \left[\beta(\omega_1 + \omega_2)H_2(\omega_1, \omega_2) + \beta(\omega_1 + \omega_3)H_2(\omega_1, \omega_3) \right. \\
&\quad \quad \left. + \beta(\omega_2 + \omega_3)H_2(\omega_2, \omega_3) \right] \exp(j(\omega_1 + \omega_2 + \omega_3)t) \\
&= -4g_2 \overbrace{\left\{ \beta(\omega_{q_1} + \omega_{q_2})H_2(\omega_{q_1}, \omega_{q_2}) \right\}}_{\omega_1, \omega_2, \omega_3} \exp(j(\omega_1 + \omega_2 + \omega_3)t)
\end{aligned} \tag{4.23}$$

The following is the general operant which obtained from the summation of the corresponding Volterra kernels over all possible permutations of the indexed frequencies without any repetition

of output terms:

$$\overline{\left\{ X_1(\omega_{q_1})X_2(\omega_{q_2}, \omega_{q_3}) \right\}}_{\omega_1, \omega_2, \omega_3} = X_1(\omega_1)X_2(\omega_2, \omega_3) + X_1(\omega_2)X_2(\omega_1, \omega_3) + X_1(\omega_3)X_2(\omega_1, \omega_2) \quad 4.24$$

Applying a same approach to the rest of the terms, we will have:

$$\begin{aligned} & 2g_2\beta(\omega)y_1(t)\beta(\omega)y_2(t)\Big|_{\omega_1, \omega_2, \omega_3} = \\ & 2g_2 \left[2\beta(\omega_1)H_1(\omega_1)\exp(j\omega_1 t)\beta(\omega_2 + \omega_3)H_2(\omega_2, \omega_3)\exp(j(\omega_2 + \omega_3)t) \right. \\ & \quad + 2\beta(\omega_2)H_1(\omega_2)\exp(j\omega_2 t)\beta(\omega_1 + \omega_3)H_2(\omega_1, \omega_3)\exp(j(\omega_1 + \omega_3)t) \\ & \quad \left. + 2\beta(\omega_3)H_1(\omega_3)\exp(j\omega_3 t)\beta(\omega_1 + \omega_2)H_2(\omega_1, \omega_2)\exp(j(\omega_1 + \omega_2)t) \right] \quad 4.25 \\ & = 4g_2 \left[\beta(\omega_1)H_1(\omega_1)\beta(\omega_1 + \omega_2)H_2(\omega_1, \omega_2) + \beta(\omega_2)H_1(\omega_2)\beta(\omega_1 + \omega_3)H_2(\omega_1, \omega_3) \right. \\ & \quad \left. + \beta(\omega_3)H_1(\omega_3)\beta(\omega_2 + \omega_3)H_2(\omega_2, \omega_3) \right] \exp(j(\omega_1 + \omega_2 + \omega_3)t) \\ & = 4g_2 \overline{\left\{ \beta(\omega_{q_1})H_1(\omega_{q_1})\beta(\omega_{q_2} + \omega_{q_3})H_2(\omega_{q_2}, \omega_{q_3}) \right\}}_{\omega_1, \omega_2, \omega_3} \exp(j(\omega_1 + \omega_2 + \omega_3)t) \end{aligned}$$

$$\begin{aligned} & -3g_3x^2(t)\beta(\omega)y_1(t)\Big|_{\omega_1, \omega_2, \omega_3} = \\ & -3g_3 \left[2\exp(j(\omega_1 + \omega_2)t)\beta(\omega_3)H_1(\omega_3)\exp(j\omega_3 t) \right. \\ & \quad + 2\exp(j(\omega_1 + \omega_3)t)\beta(\omega_2)H_1(\omega_2)\exp(j\omega_2 t) \\ & \quad \left. + 2\exp(j(\omega_2 + \omega_3)t)\beta(\omega_1)H_1(\omega_1)\exp(j\omega_1 t) \right] \quad 4.26 \\ & = -6g_3 \left[\beta(\omega_1)H_1(\omega_1) + \beta(\omega_2)H_1(\omega_2) + \beta(\omega_3)H_1(\omega_3) \right] \exp(j(\omega_1 + \omega_2 + \omega_3)t) \\ & = -6g_3 \overline{\left\{ \beta(\omega_{q_1})H_1(\omega_{q_1}) \right\}}_{\omega_1, \omega_2, \omega_3} \exp(j(\omega_1 + \omega_2 + \omega_3)t) \end{aligned}$$

$$\begin{aligned} & 3a_3x(t)(\beta(\omega)y_1(t))^2\Big|_{\omega_1, \omega_2, \omega_3} = \\ & 3g_3 \left[2\exp(j\omega_1 t)\beta(\omega_2)H_1(\omega_2)\beta(\omega_3)H_1(\omega_3)\exp(j(\omega_2 + \omega_3)t) \right. \\ & \quad + 2\exp(j\omega_2 t)\beta(\omega_1)H_1(\omega_1)\beta(\omega_3)H_1(\omega_3)\exp(j(\omega_1 + \omega_3)t) \\ & \quad \left. + 2\exp(j\omega_3 t)\beta(\omega_1)H_1(\omega_1)\beta(\omega_2)H_1(\omega_2)\exp(j(\omega_1 + \omega_2)t) \right] \quad 4.27 \\ & = -6g_3 \left[\beta(\omega_1)H_1(\omega_1)\beta(\omega_2)H_1(\omega_2) + \beta(\omega_1)H_1(\omega_1)\beta(\omega_3)H_1(\omega_3) \right. \\ & \quad \left. + \beta(\omega_2)H_1(\omega_2)\beta(\omega_3)H_1(\omega_3) \right] \exp(j(\omega_1 + \omega_2 + \omega_3)t) \\ & = -6g_3 \overline{\left\{ \beta(\omega_{q_1})H_1(\omega_{q_1})\beta(\omega_{q_2})H_1(\omega_{q_2}) \right\}}_{\omega_1, \omega_2, \omega_3} \exp(j(\omega_1 + \omega_2 + \omega_3)t) \end{aligned}$$

$$g_3 x^3(t) \Big|_{\omega_1, \omega_2, \omega_3} = 6g_3 \exp(j(\omega_1 + \omega_2 + \omega_3)t) \quad 4.28$$

$$\begin{aligned} -g_3 (\beta(\omega) y_1(t))^3 \Big|_{\omega_1, \omega_2, \omega_3} = \\ -6g_3 \beta(\omega_1) \beta(\omega_2) \beta(\omega_3) H_1(\omega_1) H_1(\omega_2) H_1(\omega_3) \exp(j(\omega_1 + \omega_2 + \omega_3)t) \end{aligned} \quad 4.29$$

Substituting Eq. 4.20, 4.23, and 4.25-4.29 into Eq. 4.19 results in:

$$\begin{aligned} H_3(\omega_1, \omega_2, \omega_3) = \frac{1}{6(1 + g_1 \beta(\omega_1 + \omega_2 + \omega_3))} \times \left\{ 4g_2 \left[-\overline{\{\beta(\omega_{q_1} + \omega_{q_2}) H_2(\omega_{q_1}, \omega_{q_2})\}}_{\omega_1, \omega_2, \omega_3}} \right. \right. \\ \left. \left. + \overline{\{\beta(\omega_{q_1}) H_1(\omega_{q_1}) \beta(\omega_{q_2} + \omega_{q_3}) H_2(\omega_{q_2}, \omega_{q_3})\}}_{\omega_1, \omega_2, \omega_3}} \right] + 6g_3 \left[1 - \overline{\{\beta(\omega_{q_1}) H_1(\omega_{q_1})\}}_{\omega_1, \omega_2, \omega_3}} \right. \right. \\ \left. \left. - \overline{\{\beta(\omega_{q_1}) H_1(\omega_{q_1}) \beta(\omega_{q_2}) H_1(\omega_{q_2})\}}_{\omega_1, \omega_2, \omega_3}} - \beta(\omega_1) \beta(\omega_2) \beta(\omega_3) H_1(\omega_1) H_1(\omega_2) H_1(\omega_3) \right] \right\} \end{aligned} \quad 4.30$$

By calculating the third Volterra kernel, H_3 , the most of the materials required for IIP3 calculation is collected. The final step is reminded is to reconfigure and apply them to IIP3 equation which would be the subject of the next section.

4.2.2 IIP3

As discussed in Appendix A, for IIP3 calculation, we have to prepare the Volterra kernels to be acceptable by Eq. A.20. Having this attitude, first $H_3(\omega, \omega, -\omega)$ should be provided which in turn requires the calculation of $H_1(\omega)$, $H_1(-\omega)$, $H_2(\omega, \omega)$, and $H_2(\omega, -\omega)$. Before continuing these computations, it is helpful to consider an important assumption of:

$$\beta(-\omega) = -\beta(\omega) \quad 4.31$$

Applying this assumption, the volterra kernels for those specific pairs of frequencies would be:

$$H_1(\omega) = \frac{g_1}{1 + g_1 \beta(\omega)} \quad 4.32$$

$$H_1(-\omega) = \frac{g_1}{1 - g_1 \beta(\omega)} \quad 4.33$$

$$H_2(\omega, \omega) = \frac{g_2}{(1 + g_1\beta(2\omega))(1 + g_1\beta(\omega))^2} \quad 4.34$$

$$H_2(\omega, -\omega) = \frac{g_2}{(1 + g_1\beta(0))(1 - g_1^2\beta^2(\omega))} \quad 4.35$$

$$H_3(\omega, \omega, -\omega) = \frac{g_2^2 A_f(\omega) - g_3 B_f(\omega)}{C_f(\omega)} \quad 4.36$$

where:

$$A_f(\omega) = 2\beta(2\omega)(2g_1\beta(\omega) - 1) + \beta(0)[2 + g_1\beta(2\omega)(2g_1\beta(\omega) + 1)] \quad 4.37$$

$$B_f(\omega) = 3(1 + g_1\beta(0))(1 + g_1\beta(2\omega))[1 + 2g_1^2\beta^2(\omega)(1 + 3g_1\beta(\omega))] \quad 4.38$$

$$C_f(\omega) = 3(g_1\beta(\omega) + 1)^3 (g_1\beta(\omega) - 1)(1 + g_1\beta(0))(1 + g_1\beta(2\omega)) \quad 4.39$$

Substituting $H_1(\omega)$ and $H_3(\omega, \omega, -\omega)$ in Eq. A.20 yields:

$$IIP3 = \sqrt{\frac{4}{3} \left| \frac{g_1 C_f(\omega)}{(g_1\beta(\omega) + 1)[g_2^2 A_f(\omega) - g_3 B_f(\omega)]} \right|} \quad 4.40$$

Eq. 4.40 shows the IIP3 of the circuit with nonlinear forward gain and feedback with memory effects. We will elaborate to this point later.

4.3 Power series vs. Volterra Series

In Section 2.6.1, the close loop gain of nonlinear amplifier with negative feedback had been discussed. However, as it was mentioned, the equation does not take care of the memory effects. The aim of this section is investigating the Volterra series results versus the power series' ones for the same circuit. This comparison will prove the accuracy of this method. Furthermore, it would shows the comprehensiveness of this series when we have to deal with a nonlinear circuit with the memory and feedback effects. Therefore, to start, the memory effects will be removed from Figure 4.1.b which will transform it to the Figure 2.39. To apply this change to the Volterra kernels and IIP3, the memory effects have to be removed from the equations as follow:

$$\beta(\omega) = \beta \text{ for } \omega \in \mathbb{R} \quad 4.41$$

Substituting Eq. 4.41 into Eq. 4.8, 4.16, and 4.30 yields:

$$H_1(\omega_1) = \frac{g_1}{1 + g_1\beta} \quad 4.42$$

$$H_2(\omega_1, \omega_2) = \frac{g_2}{(1 + g_1\beta)^3} \quad 4.43$$

$$H_3(\omega_1, \omega_2, \omega_3) = \frac{g_3(1 + g_1\beta) - 2g_2^2\beta}{(1 + g_1\beta)^5} = \frac{g_3 - \frac{2g_2^2\beta}{(1 + g_1\beta)}}{(1 + g_1\beta)^4} \quad 4.44$$

A comparison between the Eq. 4.42 through 4.44 as well as Eq. 2.103 through 2.105 reveals that Volterra series shows same functionality as the power series for a memoryless circuit. However, when it comes to memory affected circuits, the result of Volterra kernels presents more precise prediction than the power series ones. To verify the validity of this statement, IIP3 of both methods should be compared with each other. As a result, we must first calculate the IIP3 for power series results in advance. Hence, applying Eq. 2.103 and 2.105 into Eq. 2.37 leads to:

$$IIP3_{Power-Series} = \sqrt{\frac{4}{3} \frac{|g_1(1 + A_{OL})^3|}{\left|g_3 - \frac{2g_2^2}{g_1} \frac{A_{OL}}{1 + A_{OL}}\right|}} \quad 4.45$$

Taking into account the Eq. 4.40 and 4.45, the advantages of Volterra method will be easily understood. Due to the fact that the power series is unable to work with memory effects, there is a huge gap between its predicted results and real values. In other hand, the Volterra series and its multi-dimensional kernels present high accuracy analysis for such complicated circuits.

Chapter 5

A Novel CMOS 65 nm Low Noise Amplifier for WBAN application with Nonlinearity Neutralization

5.1 Introduction

Advances in CMOS technology in wireless communication systems and innovation of wireless body area networks (WBAN) and wireless personal area networks (WPAN) has addressed for the development of low-power wireless sensors [32]. These sensors can be used to monitor human bodily functions. Recently, highly integrated low-power wireless receivers have incited strong concern to meet IEEE 802.15.6 application's requirements of being lightweight and unobtrusively portable. The low-noise amplifiers (LNAs), as a result, are of critical importance, due to the determining situation of the front-end stage in transceiver architectures. While CMOS LNAs provide significant advantages in terms of low-cost, high gain, low noise, and low power consumption, the linearity of output signal has remained an issue, demanding efficient linearization techniques. Among various linearity enhancement methods, derivative superposition (DS) method and its modified version (MDS), also known as multi gate transistor (MGTR), can partly address the issue by utilizing an auxiliary transistor to nullify the third-order harmonics of the core transistor [77]. However, this improvement comes at the cost of limitations in the gain performance and quality factor of the input matching circuit. Employing a common-gate topology with positive feedback is the other method, which seems to be as beneficial only to the extent that it enhances linearity. However, utilizing positive feedback requires multiple conditions for stability which limits its applicability [91]. These problems, however, can be solved by employing intermodulation distortion sink method (IMS) [77, 92]. Although, this sounds appealing in the gain and stability characteristics, this method still suffers from the local feedback that is caused by source degeneration inductor. In this paper, a new approach based on negative feedback IMD sinker (NF-IMS) method is presented. To eliminate the above drawbacks, a negative feedback is introduced to achieve a high level of linearity, unconditional stability, and high forward gain, simultaneously.

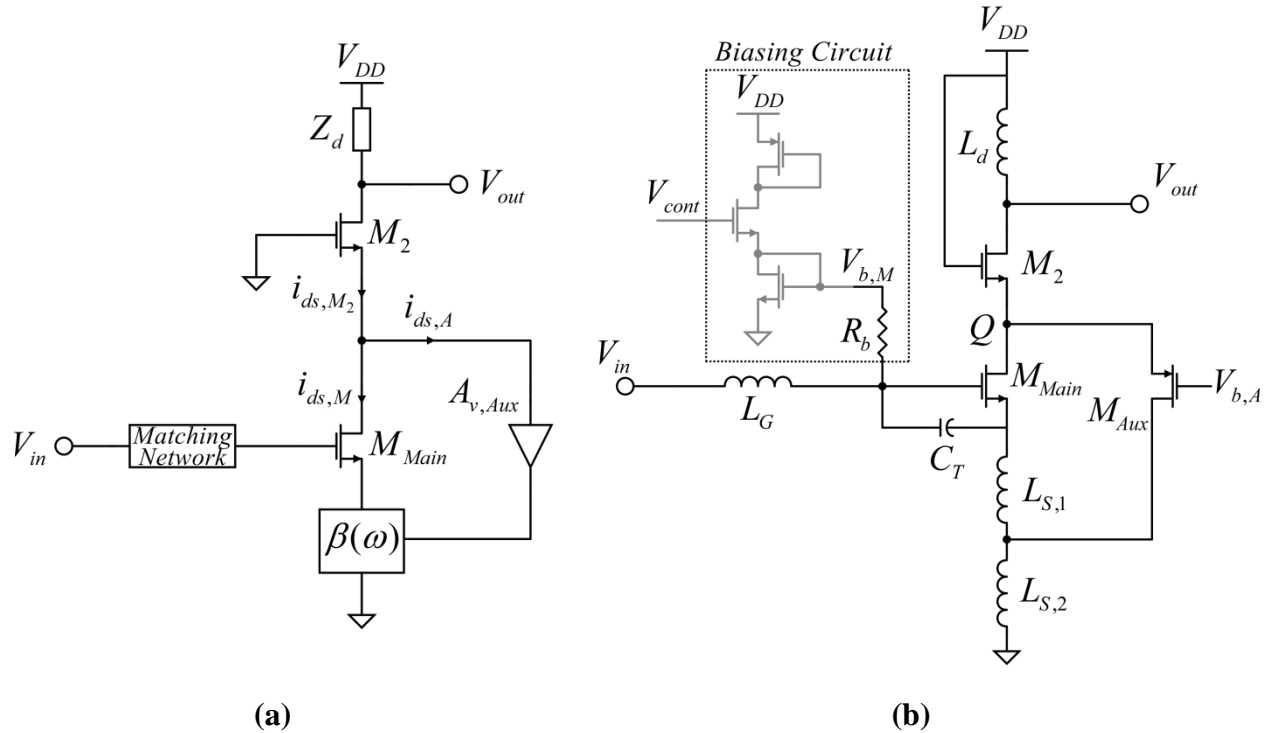


Figure 5.1: Proposed NF-IMS method over optimized CC-LNA: (a) main circuit and additional blocks, (b) full schematic's presentation.

Referring to Figure 5.1, this architecture consists of two main blocks, the core LNA, and the negative feedback loop. The core amplifier is designed for optimal noise figure (NF), whereas the auxiliary path adds a degree of freedom to linearity improvement. The great advantage of the proposed feedback loop method is that it adds less than 3mW to the power consumption, while improves the linearity more than 9dBm. The front-end amplifier is designed in CMOS 65nm technology process for WBAN and WPAN application at 2.4GHz. For the simulation results, the TSMC 65nm CRN65GP library is applied.

This chapter is organized as follows. Section 5.2 presents LNA noise optimization techniques. Section 5.3 describes the effects of NF-IMS method over gain and input-referred third-order intercept point (IIP3). The simulation results are described in Section 5.4, while section 5.5 concludes our achievements.

5.2 LNA Core Design

Achieving simultaneous efficient performance of noise, gain, input matching, linearity, and power dissipation is the main goal of LNA architectures. Due to the tradeoff between these objectives and the wide range of structures, there is a strong interest in developing LNA techniques. As discussed in Section 2.4.4, the power-constrained simultaneous noise and input matching approach is consequently a modified method that allows low-power implementation of wireless communications. By employing this technique and applying Eq. 2.87, the cascade LNA (CC-LNA) noise parameters can be optimized as:

$$L_S = 0.25 \text{ nH} , C_T = 0.4 \text{ pF} \quad 5.1$$

Considering these results, the core will be ready for nonlinearity neutralization.

5.3 Feedback and Nonlinearity Neutralization

5.3.1 CC-LNA Close Loop Gain

The gain of the optimized CC-LNA has been widely discussed in Section 2.4.4. However, the impact of a negative feedback on this structure has not yet been investigated. Furthermore, the effects of feedback in the close loop gain are a key factor in reaching a balance between IIP3 improvement and NF increase. The LNA's gain and NF have a direct relationship with each other, which is the increase of gain leads to NF improvement. The topology of negative feedback in Figure 5.1.a is a shunt-voltage and its open loop equivalent output impedance of feedback's network would be

$$Z_1 = j\omega(L_{S1} + L_{S2}) \quad 5.2$$

Also, the feedback factor is:

$$\beta(\omega) = j\omega g_{m,A} L_{S2} \quad 5.3$$

where $g_{m,A}$ represents the transconductance of auxiliary transistor. Eqs. 5.4 and 5.5 express the admittances that are seen from the drain and source of main transistor, respectively.

$$Y_2 = Y_{Aux} + Y_{M_2} = (j\omega C_{gs,A} + g_{m,A}) + (j\omega C_{gs,M_2} + g_{m,M_2}) \quad 5.4$$

$$Y_1 = j\omega C_T + g_{m,M} \quad 5.5$$

Applying the current equation at M_{Main} source and node Q, results in the open gain loop of:

$$A'_{v,int} = \frac{v_Q}{v_{in}} = \frac{-r_{o,M} \left\{ g_{m,M} \left[(1 + Y_1 Z_1) r_{o,M} + Z_1 \right] - (1 + g_{m,M} r_{o,M}) Y_2 Z_1 \right\}}{(1 + Y_2 r_{o,M}) \left[(1 + Y_1 Z_1) r_{o,M} + Z_1 \right] - (1 + g_{m,M} r_{o,M}) Y_2 Z_1} \quad 5.6$$

Considering Eq. 5.6 and the feedback theory, the close loop gain, input, and output impedance of the common-source (CS) stage will be as:

$$A_{v,int} = \frac{A'_{v,int}}{1 + \beta(\omega) A'_{v,int}} \quad 5.7$$

$$Z_{o,int} = \frac{Y_2^{-1} \parallel \left[(1 + g_{m,M} r_{o,M}) Z_1 \right]}{1 + \beta(\omega) A'_{v,int}} \quad 5.8$$

$$Z_{in} = Z_{in,opt} (1 + \beta(\omega) A'_{v,int}) \quad 5.9$$

where from Section 2.4.4 $Z_{in,opt}$ is input impedance of the CS stage and can be expressed:

$$Z_{in,opt} = j\omega(L_{S1} + L_{S2}) + \frac{1}{j\omega C_T} + \frac{g_{m,M} (L_{S1} + L_{S2})}{C_T} \quad 5.10$$

Besides, the total gain of CC-LNA with considering the negative feedback is

$$A_{tot} = A_{v,int} A_{v,CG} \quad 5.11$$

which $A_{v,CG}$ represents the gain of common-gate (CG) stage and equals to:

$$A_{v,CG} \approx \frac{Z_o (1 + g_{m,M_2} r_{o,M_2})}{Z_o + r_{o,M_2} + Z_{o,int} (1 + g_{m,M_2} r_{o,M_2})} \quad 5.12$$

Therefore, by calculating the forward linear gain of amplifier, the requirements for nonlinearity computation are met.

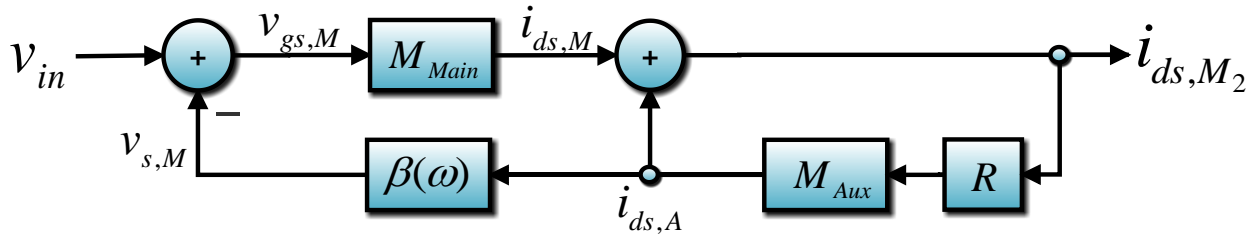


Figure 5.2: Equivalent block diagram of CC-LNA with NF-IMS method.

5.3.2 IIP3 Enhancement

The proposed negative feedback IMD sinker (NF-IMS) technique is a perfect combination of both the modified DS method and IMD sinkers. The NF-IMS method establishes a negative feedback by applying an auxiliary PMOS transistor between the drain and source of the common source (CS) stage of CC-LNA. As depicted in Figure 5.1.b, the negative feedback samples the node Q and compares the result with the input. Simultaneously, the PMOS introduces an internal current loop to trap and cancel out the nonlinear component of the main transistor current ($i_{ds,M}$). The auxiliary transistor current, ($i_{sd,A}$), prevents the third nonlinearity component of main transistor to feed the CG stage by generating a same third harmonic in the opposite phase. In other words, the third harmonic will be sank and removed from the output current (i_{ds,M_2}) by $i_{sd,A}$. At the same time, the same components of nonlinearity are presented in the source of the main transistor. The next problem is known as second-order interaction which is caused by a combination of the source local feedback and the second order harmonics (Section 2.6). To avoid this phenomenon from contributing in the IM3, the auxiliary current is injected to the source node of the main transistor. The IIP3's expression provides a better overview of this technique. The first step in IIP3's calculation is to derive the largest source of nonlinearity of MOSFETs. The nonlinearity is mostly contributed by the transconductance of a transistor (g_m). Although, the parasitic elements, like junction capacitors and channel conductance (g_{ds}) show nonlinear behaviors, g_m is known as the most nonlinear factor. Thus, the nonlinearity of drain-source current can be expressed as (Section 2.6):

$$i_{ds,M}(v_{gs,M}) = g_{1,M}v_{gs,M} + g_{2,M}v_{gs,M}^2 + \dots + g_{N_M,M}v_{gs,M}^{N_M} = \sum_{m_M=1}^{N_M} g_{m_M,M}v_{gs,M}^{m_M} \quad 5.13$$

$$i_{sd,A}(v_{gs,A}) = g_{1,A}v_{gs,A} + g_{2,A}v_{gs,A}^2 + \dots + g_{N_A,A}v_{gs,A}^{N_A} = \sum_{m_A=1}^{N_A} g_{m_A,A}v_{gs,A}^{m_A} \quad 5.14$$

where the g_i is defined as i th-order derivation of the drain current. Based on the Figure A.2, the extracting the block diagram of circuit is our first priority (Figure 5.2) and the input to output function is placed in the second step. Thus, starting from output results:

$$i_{ds,M_2}(t) = i_{ds,M}(t) + i_{sd,A}(t) \quad 5.15$$

where by considering Eq. 5.14 and Figure 5.2, the auxiliary current is defined as:

$$i_{sd,A}(t) = \sum_{m_A=1}^{N_A} g_{m_A,A} \left[R i_{ds,M_2}(t) \right]^{m_A} v_{gs,A}^{m_A} \quad 5.16$$

which R is frequency dependent constant and defined as the total impedance seen from the M_{Main} 's drain and the main transistor current would be:

$$i_{ds,M}(v_{gs,M}) = \sum_{m_M=1}^{N_M} g_{m_M,M} \left(v_{in}(t) - v_{s,M}(t) \right)^{m_M} \quad 5.17$$

where the source voltage is represented by:

$$v_{s,M}(t) = \beta(\omega) i_{sd,A}(t) \quad 5.18$$

Substituting Eqs. 5.16-5.18 into Eq. 5.15, the total output current is equaled to:

$$i_{ds,M_2}(t) = \sum_{m_M=1}^{N_M} g_{m_M,M} \left(v_{in}(t) - \sum_{m_A=1}^{N_A} g_{m_A,A} \left[R i_{ds,M_2}(t) \right]^{m_A} \right)^{m_M} + \sum_{m_A=1}^{N_A} g_{m_A,A} \left[R i_{ds,M_2}(t) \right]^{m_A} \quad 5.19$$

So far, the nonlinear time base transfer function has been extracted by the aid of the equivalent block diagram. To start the computation of the Volterra kernels, Eqs. A.11 and A.12 should be modified in order to be compatible with NF-IMS calculations:

$$v_{in}(t) = \frac{1}{2} \sum_{q_1=-Q}^Q V_{in,q_1} \exp(j\omega_{q_1} t) \quad 5.20$$

$$i_{ds,M_2(n)} = \frac{1}{2^n} \sum_{q_1=-3}^3 \dots \sum_{q_n=-3}^3 V_{in,q_1} \dots V_{in,q_n} H_n(\omega_{q_1}, \dots, \omega_{q_n}) e^{j(\omega_{q_1} + \dots + \omega_{q_n})t} \quad 5.21$$

Now, by exciting the circuit with a single frequency tone, ω_1 , and apply it to Eq. 5.19 results:

$$\begin{aligned} i_{ds,M_2(1)}(t) + \overbrace{\sum_{p=2}^N i_{ds,M_2(p)}(t)}^0 = \\ g_{1,M} \left[v_{in}(t) - g_{1,A} R \beta(\omega) \left(i_{ds,M_2(1)}(t) + \overbrace{\sum_{p=2}^N i_{ds,M_2(p)}(t)}^0 \right) - \overbrace{\sum_{m_A=2}^{N_A} g_{m_A,A} [R i_{ds,M_2}(t)]^{m_A}}^0 \right] \\ + \overbrace{\sum_{m_M=2}^{N_M} g_{m_M,M} \left(v_{in}(t) - \sum_{m_A=1}^{N_A} g_{m_A,A} [R i_{ds,M_2}(t)]^{m_A} \right)^{m_M}}^0 \\ + g_{1,A} R i_{ds,M_2(1)}(t) + \overbrace{\sum_{m_A=2}^{N_A} g_{m_A,A} [R i_{ds,M_2}(t)]^{m_A}}^0 \end{aligned} \quad 5.22$$

Applying Eq. 5.21 into Eq. 5.22 results:

$$\begin{aligned} \frac{1}{2} \sum_{q_1=1}^1 V_{in,q_1} (1 + g_{1,M} g_{1,A} \beta(\omega_{q_1}) R - g_{1,A} R) H_1(\omega_{q_1}) \exp(j\omega_{q_1} t) = g_{1,M} \exp(j\omega_1 t) \\ H_1(\omega_1) = \frac{g_{1,M}}{1 + [g_{1,M} \beta(\omega_1) - 1] g_{1,A} R} \quad 5.23 \end{aligned}$$

In the same way of the first order kernel computation, the second order kernel calculation is initiated by increasing the number of excitations to two tones (ω_1, ω_2).

$$v_{in}(t) = \frac{1}{2} \sum_{q_1=1}^2 V_{in,q_1} \exp(j\omega_{q_1} t) = \exp(j\omega_1 t) + \exp(j\omega_2 t) \quad 5.24$$

Substituting Eq. 5.24 in Eq. 5.19 yields:

$$\begin{aligned} & \overbrace{i_{ds,M_2(1)}(t)}^0 + i_{ds,M_2(2)}(t) + \sum_{n=3}^N \overbrace{i_{ds,M_2(n)}(t)}^0 = \\ & g_{1,M} \left[\overbrace{v_{in}(t)}^0 - g_{1,A} R \beta(\omega) \left(i_{ds,M_2(2)}(t) + \overbrace{\dots}^0 \right) - g_{2,A} R^2 \beta(\omega) \left(i_{ds,M_2(1)}(t) + \overbrace{\dots}^0 \right) - \overbrace{\dots}^0 \right] \\ & + g_{2,M} \left[v_{in}(t) - g_{1,A} R \beta(\omega) \left(i_{ds,M_2(1)}(t) + \overbrace{\dots}^0 \right) - \overbrace{\dots}^0 \right]^2 + \sum_{m_M=3}^{N_M} \overbrace{g_{m_M,M}(\dots)}^0{}^{m_M} \\ & + g_{1,A} R \left(i_{ds,M_2(2)}(t) + \overbrace{\dots}^0 \right) + g_{2,A} R^2 \left(i_{ds,M_2(1)}(t) + \overbrace{\dots}^0 \right)^2 + \sum_{m_A=3}^{N_A} \overbrace{g_{m_A,A} [R i_{ds,M_2}(t)]}^0{}^{m_A} \\ & i_{ds,M_2(2)}(t) \left[1 + g_{1,M} g_{1,A} R \beta(\omega) - g_{1,A} R \right] = g_{2,M} v_{in}^2(t) - 2g_{2,M} g_{1,A} R v_{in}(t) \beta(\omega) i_{ds,M_2(1)}(t) \\ & + g_{2,M} g_{1,A}^2 R^2 \left(\beta(\omega) i_{ds,M_2(1)}(t) \right)^2 + g_{2,A} R^2 \left(i_{ds,M_2(1)}(t) \right)^2 - g_{1,M} g_{2,A} R^2 \beta(\omega) \left(i_{ds,M_2(1)}(t) \right)^2 \end{aligned} \quad 5.25$$

Purifying Eq. 5.25 from the terms which does not contains both of the input tones (ω_1, ω_2), simultaneously.

$$\begin{aligned} & \left[1 + g_{1,M} g_{1,A} R \beta(\omega) - g_{1,A} R \right] i_{ds,M_2(2)}(t) \Big|_{\omega_1, \omega_2} = \\ & \frac{1}{2^2} \sum_{q_1=1}^2 \sum_{q_2=1}^2 V_{in,q_1} V_{in,q_2} \left[1 + g_{1,A} R \left(g_{1,M} \beta(\omega_{q_1} + \omega_{q_2}) - 1 \right) \right] H_2(\omega_{q_1}, \omega_{q_2}) \exp(j(\omega_{q_1} + \omega_{q_2})t) \quad 5.26 \\ & = 2 \left[1 + g_{1,M} g_{1,A} R \beta(\omega_1 + \omega_2) - g_{1,A} R \right] H_2(\omega_1, \omega_2) \exp(j(\omega_1 + \omega_2)t) \end{aligned}$$

$$\begin{aligned}
g_{2,M} v_{in}^2(t) \Big|_{\omega_1, \omega_2} &= g_{2,M} \left(\frac{1}{2} \sum_{q_1=1}^2 V_{in,q_1} \exp(j\omega_{q_1} t) \right) \left(\frac{1}{2} \sum_{q_2=1}^2 V_{in,q_2} \exp(j\omega_{q_2} t) \right) \\
&= 2g_{2,M} \exp(j(\omega_1 + \omega_2)t)
\end{aligned} \tag{5.27}$$

$$\begin{aligned}
-2g_{2,M} g_{1,A} R v_{in}(t) \beta(\omega) i_{ds,M_2(1)}(t) \Big|_{\omega_1, \omega_2} &= \\
-2g_{2,M} g_{1,A} R \left(\frac{1}{\sqrt{2}} \sum_{q_1=1}^2 V_{m,q_1} \exp(j\omega_{q_1} t) \right) \left(\frac{1}{\sqrt{2}} \sum_{q_2=1}^2 V_{m,q_2} \beta(\omega_{q_2}) H_1(\omega_{q_2}) \exp(j\omega_{q_2} t) \right) &= \\
-2g_{2,M} g_{1,A} R \overbrace{\left\{ \beta(\omega_{q_1}) H_1(\omega_{q_1}) \right\}}_{\omega_1, \omega_2} \exp(j(\omega_1 + \omega_2)t) &
\end{aligned} \tag{5.28}$$

$$\begin{aligned}
g_{2,M} g_{1,A}^2 R^2 \left(\beta(\omega) i_{ds,M_2(1)}(t) \right)^2 \Big|_{\omega_1, \omega_2} &= \\
g_{2,M} g_{1,A}^2 R^2 \left(\frac{1}{\sqrt{2}} \sum_{q_1=1}^2 V_{m,q_1} \beta(\omega_{q_1}) H_1(\omega_{q_1}) \exp(j\omega_{q_1} t) \right) \times & \\
\left(\frac{1}{\sqrt{2}} \sum_{q_2=1}^2 V_{m,q_2} \beta(\omega_{q_2}) H_1(\omega_{q_2}) \exp(j\omega_{q_2} t) \right) & \\
= 2g_{2,M} g_{1,A}^2 R^2 \beta(\omega_1) \beta(\omega_2) H_1(\omega_1) H_1(\omega_2) \exp(j(\omega_1 + \omega_2)t) &
\end{aligned} \tag{5.29}$$

$$\begin{aligned}
g_{2,A} R^2 \left(i_{ds,M_2(1)}(t) \right)^2 \Big|_{\omega_1, \omega_2} &= \\
g_{2,A} R^2 \left(\frac{1}{\sqrt{2}} \sum_{q_1=1}^2 V_{m,q_1} H_1(\omega_{q_1}) \exp(j\omega_{q_1} t) \right) \left(\frac{1}{\sqrt{2}} \sum_{q_2=1}^2 V_{m,q_2} H_1(\omega_{q_2}) \exp(j\omega_{q_2} t) \right) & \\
= g_{2,A} R^2 \sum_{q_1=1}^2 \sum_{q_2=1}^2 H_1(\omega_{q_1}) H_1(\omega_{q_2}) \exp(j(\omega_{q_1} + \omega_{q_2})t) & \\
= 2g_{2,A} R^2 H_1(\omega_1) H_1(\omega_2) \exp(j(\omega_1 + \omega_2)t) &
\end{aligned} \tag{5.30}$$

$$\begin{aligned}
-g_{1,M} g_{2,A} R^2 \beta(\omega) \left(i_{ds,M_2(1)}(t) \right)^2 \Big|_{\omega_1, \omega_2} &= \\
-g_{1,M} g_{2,A} R^2 \beta(\omega) \left(\frac{1}{\sqrt{2}} \sum_{q_1=1}^2 V_{m,q_1} H_1(\omega_{q_1}) \exp(j\omega_{q_1} t) \right) \left(\frac{1}{\sqrt{2}} \sum_{q_2=1}^2 V_{m,q_2} H_1(\omega_{q_2}) \exp(j\omega_{q_2} t) \right) & \\
= -g_{1,M} g_{2,A} R^2 \sum_{q_1=1}^2 \sum_{q_2=1}^2 \beta(\omega_{q_1} + \omega_{q_2}) H_1(\omega_{q_1}) H_1(\omega_{q_2}) \exp(j(\omega_{q_1} + \omega_{q_2})t) & \\
= -2g_{1,M} g_{2,A} R^2 \beta(\omega_1 + \omega_2) H_1(\omega_1) H_1(\omega_2) \exp(j(\omega_1 + \omega_2)t) &
\end{aligned} \tag{5.31}$$

Substituting Eqs. 5.26-5.31 into Eq. 5.25 is given:

$$\begin{aligned}
H_2(\omega_1, \omega_2) &= \frac{1}{1 + (g_{1,M} \beta(\omega_1 + \omega_2) - 1) g_{1,A} R} \times \\
&\left\{ g_{2,M} - g_{2,M} g_{1,A} R \overline{\beta(\omega_{q_1}) H_1(\omega_{q_1})} \right\}_{\omega_1, \omega_2} + \\
&\left[g_{2,M} g_{1,A}^2 \beta(\omega_1) \beta(\omega_2) - g_{1,M} g_{2,A} \beta(\omega_1 + \omega_2) + g_{2,A} \right] R^2 H_1(\omega_1) H_1(\omega_2) \}
\end{aligned} \tag{5.32}$$

The first and second Volterra kernels are obtained in Eqs. 5.23 and 5.32, respectively. Depicting in IIP3 calculation flowchart (Figure A.2), the third order kernel's computation could be carried out by applying an input with three different tones:

$$v_{in}(t) = \frac{1}{2} \sum_{q_1=1}^3 V_{in,q_1} \exp(j\omega_{q_1} t) = \exp(j\omega_1 t) + \exp(j\omega_2 t) + \exp(j\omega_3 t) \tag{5.33}$$

So, applying Eq. 5.31 into Eq. 5.19 will result:

$$\begin{aligned}
&\overbrace{i_{ds,M_2(1)}(t) + i_{ds,M_2(2)}(t)}^0 + i_{ds,M_2(3)}(t) + \sum_{n=4}^N \overbrace{i_{ds,M_2(n)}(t)}^0 = g_{1,M} \left[\overbrace{x(t)}^0 - g_{1,A} R \times \right. \\
&\beta(\omega) \left(i_{ds,M_2(3)}(t) + \overbrace{\cancel{\dots}}^0 \right) - g_{2,A} R^2 \beta(\omega) \left(i_{ds,M_2(1)}(t) + i_{ds,M_2(2)}(t) + \overbrace{\cancel{\dots}}^0 \right)^2 - g_{3,A} R^3 \beta(\omega) \times \\
&\left(i_{ds,M_2(1)}(t) + \overbrace{\cancel{\dots}}^0 \right)^3 - \overbrace{\cancel{\dots}}^0 \left. + g_{2,M} \left[v_{in}(t) - g_{1,A} R \beta(\omega) \left(i_{ds,M_2(1)}(t) + i_{ds,M_2(2)}(t) + \overbrace{\cancel{\dots}}^0 \right) \right. \right. \\
&\left. \left. - g_{2,A} R^2 \beta(\omega) \left(i_{ds,M_2(1)}(t) + \overbrace{\cancel{\dots}}^0 \right)^2 - \overbrace{\cancel{\dots}}^0 \right] + g_{3,M} \left[v_{in}(t) - g_{1,A} R \beta(\omega) \left(i_{ds,M_2(1)}(t) + \overbrace{\cancel{\dots}}^0 \right) \right. \right. \\
&\left. \left. - \overbrace{\cancel{\dots}}^0 \right]^3 + \sum_{m=3}^N \overbrace{g_{m,M} (\dots)^{m_M}}^0 + g_{1,A} R \left(i_{ds,M_2(3)}(t) + \overbrace{\cancel{\dots}}^0 \right) + g_{2,A} R^2 \left(i_{ds,M_2(1)}(t) + i_{ds,M_2(2)}(t) \right) \right.
\end{aligned} \tag{5.34}$$

$$+ \overbrace{\left[\frac{0}{\dots} \right]^2} + g_{3,A} R^3 \left(i_{ds,M_2(1)}(t) + \overbrace{\left[\frac{0}{\dots} \right]^3} + \sum_{m_A=3}^{M_A} \overbrace{g_{m_A,A} [\dots]^{m_A}}^0 \right)$$

Simplifying Eq. 4.185.34 yields:

$$\begin{aligned} & i_{ds,M_2(3)}(t) \left[1 + g_{1,M} g_{1,A} R \beta(\omega) - g_{1,A} R \right] = g_{3,A} R^3 \left(i_{ds,M_2(1)}(t) \right)^3 \\ & + g_{1,M} \left[-g_{2,A} R^2 \beta(\omega) \left(i_{ds,M_2(1)}(t) + i_{ds,M_2(2)}(t) \right)^2 - g_{3,A} R^3 \beta(\omega) \left(i_{ds,M_2(1)}(t) \right)^3 \right] \\ & + g_{2,M} \left[v_{in}(t) - g_{1,A} R \beta(\omega) \left(i_{ds,M_2(1)}(t) + i_{ds,M_2(2)}(t) \right) - g_{2,A} R^2 \beta(\omega) \left(i_{ds,M_2(1)}(t) \right)^2 \right]^2 \\ & + g_{3,M} \left[v_{in}(t) - g_{1,A} R \beta(\omega) i_{ds,M_2(1)}(t) \right]^3 + g_{2,A} R^2 \left[i_{ds,M_2(1)}(t) + i_{ds,M_2(2)}(t) \right]^2 \end{aligned} \quad 5.35$$

Expanding and extracting only the third order terms brings out:

$$\begin{aligned} & \left[1 + g_{1,M} g_{1,A} R \beta(\omega) - g_{1,A} R \right] i_{ds,M_2(3)}(t) = -2 g_{1,M} g_{2,A} R^2 \beta(\omega) i_{ds,M_2(1)}(t) i_{ds,M_2(2)}(t) \\ & + g_{2,M} \left[-2 g_{1,A} R v_{in}(t) \beta(\omega) i_{ds,M_2(2)}(t) - 2 g_{2,A} R^2 v_{in}(t) \beta(\omega) \left(i_{ds,M_2(1)}(t) \right)^2 + 2 g_{1,A}^2 R^2 \times \right. \\ & \left. \beta(\omega) i_{ds,M_2(1)}(t) \beta(\omega) i_{ds,M_2(2)}(t) + 2 g_{1,A} g_{2,A} R^3 \beta(\omega) i_{ds,M_2(1)}(t) \beta(\omega) \left(i_{ds,M_2(1)}(t) \right)^2 \right] \\ & + g_{3,M} \left[v_{in}^3(t) - 3 g_{1,A} R v_{in}^2(t) \beta(\omega) i_{ds,M_2(1)}(t) + 3 g_{1,A}^2 R^2 v_{in}(t) \left(\beta(\omega) i_{ds,M_2(1)}(t) \right)^2 - g_{1,A}^3 \times \right. \\ & \left. R^3 \left(\beta(\omega) i_{ds,M_2(1)}(t) \right)^3 \right] + 2 g_{2,A} R^2 i_{ds,M_2(1)}(t) i_{ds,M_2(2)}(t) + g_{3,A} R^3 \left(1 - g_{1,M} \beta(\omega) \right) \left(i_{ds,M_2(1)}(t) \right)^3 \end{aligned} \quad 5.36$$

Same as process was done over Eq. 4.19, the third-order terms in Eq. 5.36 should be translated to first, second, and third order kernels as well as the extraction of their coefficients. However, the number of terms influences us to analyses each term separately due to simplicity in tracing the equations.

$$\begin{aligned} & \left[1 + g_{1,M} g_{1,A} R \beta(\omega) - g_{1,A} R \right] i_{ds,M_2(3)}(t) \Big|_{\omega_1, \omega_2, \omega_3} = \\ & \frac{1}{2^3} \sum_{q_1=1}^3 \sum_{q_2=1}^3 \sum_{q_3=1}^3 \left\{ \cancel{v_{in,q_1} v_{in,q_2} v_{in,q_3}} \left[1 + g_{1,M} g_{1,A} R \beta(\omega_{q_1} + \omega_{q_2} + \omega_{q_3}) - g_{1,A} R \right] \times \right. \\ & \left. H_3(\omega_{q_1}, \omega_{q_2}, \omega_{q_3}) \exp(j(\omega_{q_1} + \omega_{q_2} + \omega_{q_3})t) \right\} \\ & = 6 \left[1 + g_{1,M} g_{1,A} R \beta(\omega_1 + \omega_2 + \omega_3) - g_{1,A} R \right] H_3(\omega_1, \omega_2, \omega_3) \exp(j(\omega_1 + \omega_2 + \omega_3)t) \end{aligned} \quad 5.37$$

In Eq. 5.36, for the rest of the terms that includes a pair of the first and second order terms, the following frequencies' distribution is required:

$$\begin{array}{ccc} i_{ds,M_2(1)}, v_{in}(t) & \omega_1 & \omega_2 & \omega_3 \\ i_{ds,M_2(2)}, (i_{ds,M_2(1)})^2 & \omega_2, \omega_3 & \omega_1, \omega_3 & \omega_1, \omega_2 \end{array} \quad 5.38$$

By the aid of Eq. 5.38, the rest of calculation would be as following:

$$\begin{aligned} & -2g_{1,M}g_{2,A}R^2\beta(\omega)i_{ds,M_2(1)}(t)i_{ds,M_2(2)}(t)\Big|_{\omega_1,\omega_2,\omega_3} = \\ & -2g_{1,M}g_{2,A}R^2\beta(\omega)\left[\frac{1}{2^2}\sum_{q_1=1}^3V_{m,q_1}H_1(\omega_{q_1})\exp(j\omega_{q_1}t)\right] \\ & \left[\frac{1}{2^2}\sum_{q_2=1}^3\sum_{q_3=1}^3V_{m,q_2}V_{m,q_3}H_2(\omega_{q_2},\omega_{q_3})\exp(j(\omega_{q_2},\omega_{q_3})t)\right] = \quad 5.39 \end{aligned}$$

$$\begin{aligned} & -4g_{1,M}g_{2,A}R^2\beta(\omega_1+\omega_2+\omega_3)[H_1(\omega_1)H_2(\omega_2,\omega_3)+H_1(\omega_2)H_2(\omega_1,\omega_3)+ \\ & \quad H_1(\omega_3)H_2(\omega_1,\omega_2)]\exp(j(\omega_1+\omega_2+\omega_3)t) = \\ & -4g_{1,M}g_{2,A}R^2\beta(\omega_1+\omega_2+\omega_3)\{H_1(\omega_{q_1})H_2(\omega_{q_2},\omega_{q_3})\}_{\omega_1,\omega_2,\omega_3}\exp(j(\omega_1+\omega_2+\omega_3)t) \\ & -2g_{2,M}g_{1,A}Rv_{in}(t)\beta(\omega)i_{ds,M_2(2)}(t)\Big|_{\omega_1,\omega_2,\omega_3} = \\ & -2g_{2,M}g_{1,A}R\left[2\exp(j\omega_1t)\beta(\omega_2+\omega_3)H_2(\omega_2,\omega_3)\exp(j(\omega_2+\omega_3)t) \right. \\ & \quad + 2\exp(j\omega_2t)\beta(\omega_1+\omega_3)H_2(\omega_1,\omega_3)\exp(j(\omega_1+\omega_3)t) \\ & \quad \left. + 2\exp(j\omega_3t)\beta(\omega_1+\omega_2)H_2(\omega_1,\omega_2)\exp(j(\omega_1+\omega_3)t)\right] \quad 5.40 \end{aligned}$$

$$\begin{aligned} & = -4g_{2,M}g_{1,A}R\left[\beta(\omega_1+\omega_2)H_2(\omega_1,\omega_2)+\beta(\omega_1+\omega_3)H_2(\omega_1,\omega_3) \right. \\ & \quad \left. +\beta(\omega_2+\omega_3)H_2(\omega_2,\omega_3)\right]\exp(j(\omega_1+\omega_2+\omega_3)t) \\ & = -4g_{2,M}g_{1,A}R\{\beta(\omega_{q_1}+\omega_{q_2})H_2(\omega_{q_1},\omega_{q_2})\}_{\omega_1,\omega_2,\omega_3}\exp(j(\omega_1+\omega_2+\omega_3)t) \end{aligned}$$

$$\begin{aligned} & -2g_{2,M}g_{2,A}R^2v_{in}(t)\beta(\omega)(i_{ds,M_2(1)}(t))^2\Big|_{\omega_1,\omega_2,\omega_3} = \\ & -2g_{2,M}g_{2,A}R^2\left[2\exp(j\omega_1t)\beta(\omega_2+\omega_3)H_1(\omega_2)H_1(\omega_3)\exp(j(\omega_2+\omega_3)t) \right. \\ & \quad + 2\exp(j\omega_2t)\beta(\omega_1+\omega_3)H_1(\omega_1)H_1(\omega_3)\exp(j(\omega_1+\omega_3)t) \\ & \quad \left. + 2\exp(j\omega_3t)\beta(\omega_1+\omega_2)H_1(\omega_1)H_1(\omega_2)\exp(j(\omega_1+\omega_2)t)\right] \quad 5.41 \end{aligned}$$

$$\begin{aligned}
&= -4g_{2,M}g_{2,A}R^2 \left[\beta(\omega_1 + \omega_2)H_1(\omega_1)H_1(\omega_2) + \beta(\omega_1 + \omega_3)H_1(\omega_1)H_1(\omega_3) \right. \\
&\quad \left. + \beta(\omega_2 + \omega_3)H_1(\omega_2)H_1(\omega_3) \right] \exp(j(\omega_1 + \omega_2 + \omega_3)t) \\
&= -4g_{2,M}g_{2,A}R^2 \overline{\left\{ \beta(\omega_{q_1} + \omega_{q_2})H_1(\omega_{q_1})H_1(\omega_{q_2}) \right\}}_{\omega_1, \omega_2, \omega_3} \exp(j(\omega_1 + \omega_2 + \omega_3)t) \\
&+ 2g_{2,M}g_{1,A}^2R^2\beta(\omega)i_{ds,M_2(1)}(t)\beta(\omega)i_{ds,M_2(2)}(t)\Big|_{\omega_1, \omega_2, \omega_3} = \\
&2g_{2,M}g_{1,A}^2R^2 \left[2\beta(\omega_1)H_1(\omega_1)\exp(j\omega_1t)\beta(\omega_2 + \omega_3)H_2(\omega_2, \omega_3)\exp(j(\omega_2 + \omega_3)t) \right. \\
&\quad + 2\beta(\omega_2)H_1(\omega_2)\exp(j\omega_2t)\beta(\omega_1 + \omega_3)H_2(\omega_1, \omega_3)\exp(j(\omega_1 + \omega_3)t) \\
&\quad \left. + 2\beta(\omega_3)H_1(\omega_3)\exp(j\omega_3t)\beta(\omega_1 + \omega_2)H_2(\omega_1, \omega_2)\exp(j(\omega_1 + \omega_2)t) \right] \\
&= 4g_{2,M}g_{1,A}^2R^2 \left[\beta(\omega_1)H_1(\omega_1)\beta(\omega_2 + \omega_3)H_2(\omega_2, \omega_3) \right. \\
&\quad + \beta(\omega_2)H_1(\omega_2)\beta(\omega_1 + \omega_3)H_2(\omega_1, \omega_3) \\
&\quad \left. + \beta(\omega_3)H_1(\omega_3)\beta(\omega_1, \omega_2)H_2(\omega_1, \omega_2) \right] \exp(j(\omega_1 + \omega_2 + \omega_3)t) \\
&= 4g_{2,M}g_{1,A}^2R^2 \overline{\left\{ \beta(\omega_{q_1})H_1(\omega_{q_1})\beta(\omega_{q_2} + \omega_{q_3})H_2(\omega_{q_2}, \omega_{q_3}) \right\}}_{\omega_1, \omega_2, \omega_3} \exp(j(\omega_1 + \omega_2 + \omega_3)t)
\end{aligned} \tag{5.42}$$

$$\begin{aligned}
&+ 2g_{2,M}g_{1,A}g_{2,A}R^3\beta(\omega)i_{ds,M_2(1)}(t)\beta(\omega)\left(i_{ds,M_2(1)}(t)\right)^2\Big|_{\omega_1, \omega_2, \omega_3} = \\
&2g_{2,M}g_{1,A}g_{2,A}R^3 \times \\
&\quad \left\{ 2\beta(\omega_1)H_1(\omega_1)\exp(j\omega_1t)\beta(\omega_2 + \omega_3)H_1(\omega_2)H_1(\omega_3)\exp(j(\omega_2 + \omega_3)t) \right. \\
&\quad + 2\beta(\omega_2)H_1(\omega_2)\exp(j\omega_2t)\beta(\omega_1 + \omega_3)H_1(\omega_1)H_1(\omega_3)\exp(j(\omega_1 + \omega_3)t) \\
&\quad \left. + 2\beta(\omega_3)H_1(\omega_3)\exp(j\omega_3t)\beta(\omega_1 + \omega_2)H_1(\omega_1)H_1(\omega_2)\exp(j(\omega_1 + \omega_2)t) \right\} \\
&= 4g_{2,M}g_{1,A}g_{2,A}R^3 \left[\beta(\omega_1)\beta(\omega_2 + \omega_3) + \beta(\omega_2)\beta(\omega_1 + \omega_3) + \beta(\omega_3)\beta(\omega_1 + \omega_2) \right] \times \\
&\quad H_1(\omega_1)H_1(\omega_2)H_1(\omega_3)\exp(j(\omega_1 + \omega_2 + \omega_3)t) \\
&= 4g_{2,M}g_{1,A}g_{2,A}R^3 \overline{\left\{ \beta(\omega_{q_1})\beta(\omega_{q_2} + \omega_{q_3}) \right\}}_{\omega_1, \omega_2, \omega_3} \times \\
&\quad H_1(\omega_1)H_1(\omega_2)H_1(\omega_3)\exp(j(\omega_1 + \omega_2 + \omega_3)t)
\end{aligned} \tag{5.43}$$

$$\begin{aligned}
&+ g_{3,M}V_{in}^3(t)\Big|_{\omega_1, \omega_2, \omega_3} = \frac{1}{2^3} \sum_{q_1=1}^3 \sum_{q_2=1}^3 \sum_{q_3=1}^3 \cancel{V_{in,q_1} V_{in,q_2} V_{in,q_3}} \exp(j(\omega_{q_1} + \omega_{q_2} + \omega_{q_3})t) \\
&= 6g_{3,M} \exp(j(\omega_1 + \omega_2 + \omega_3)t)
\end{aligned} \tag{5.44}$$

$$\begin{aligned}
& -3g_{3,M}g_{1,A}Rv_{in}^2(t)\beta(\omega)i_{ds,M_2(1)}(t)\Big|_{\omega_1,\omega_2,\omega_3} = \\
& -3g_{3,M}g_{1,A}R\left[\frac{1}{Z^2}\sum_{q_1=1}^3\sum_{q_2=1}^3V_{in,q_1}V_{in,q_2}\exp(j(\omega_{q_1}+\omega_{q_2})t)\right]\times \\
& \left[\frac{1}{Z}\sum_{q_3=1}^3V_{in,q_3}\beta(\omega_{q_3})H_1(\omega_{q_3})\exp(j\omega_{q_3}t)\right]= \\
& -3g_{3,M}g_{1,A}R\left[2\exp(j(\omega_1+\omega_2)t)\beta(\omega_3)H_1(\omega_3)\exp(j\omega_3t)\right. \\
& \quad +2\exp(j(\omega_1+\omega_3)t)\beta(\omega_2)H_1(\omega_2)\exp(j\omega_2t) \\
& \quad \left.+2\exp(j(\omega_2+\omega_3)t)\beta(\omega_1)H_1(\omega_1)\exp(j\omega_1t)\right] \tag{5.45} \\
& =-6g_{3,M}g_{1,A}R\left[\beta(\omega_1)H_1(\omega_1)+\beta(\omega_2)H_1(\omega_2)+\beta(\omega_3)H_1(\omega_3)\right]\exp(j(\omega_1+\omega_2+\omega_3)t) \\
& =-6g_{3,M}g_{1,A}R\overline{\left\{\beta(\omega_{q_1})H_1(\omega_{q_1})\right\}_{\omega_1,\omega_2,\omega_3}}\exp(j(\omega_1+\omega_2+\omega_3)t)
\end{aligned}$$

$$\begin{aligned}
& +3g_{3,M}g_{1,A}^2R^2v_{in}(t)\left(\beta(\omega)i_{ds,M_2(1)}(t)\right)^2\Big|_{\omega_1,\omega_2,\omega_3} = \\
& +3g_{3,M}g_{1,A}^2R^2\left[\frac{1}{Z}\sum_{q_1=1}^3V_{in,q_1}\exp(j\omega_{q_1}t)\right]\times \\
& \left[\frac{1}{Z^2}\sum_{q_2=1}^3\sum_{q_3=1}^3V_{in,q_2}V_{in,q_3}\beta(\omega_{q_2})H_1(\omega_{q_2})\beta(\omega_{q_3})H_1(\omega_{q_3})\exp(j(\omega_{q_2}+\omega_{q_3})t)\right]= \\
& +3g_{3,M}g_{1,A}^2R^2\left[2\exp(j\omega_1t)\beta(\omega_2)H_1(\omega_2)\beta(\omega_3)H_1(\omega_3)\exp(j(\omega_2+\omega_3)t)\right. \\
& \quad +2\exp(j\omega_2t)\beta(\omega_1)H_1(\omega_1)\beta(\omega_3)H_1(\omega_3)\exp(j(\omega_1+\omega_3)t) \\
& \quad \left.+2\exp(j\omega_3t)\beta(\omega_1)H_1(\omega_1)\beta(\omega_2)H_1(\omega_2)\exp(j(\omega_1+\omega_2)t)\right]= \\
& 6g_{3,M}g_{1,A}^2R^2\left[\beta(\omega_1)H_1(\omega_1)\beta(\omega_2)H_1(\omega_2)+\beta(\omega_1)H_1(\omega_1)\beta(\omega_3)H_1(\omega_3)\right. \\
& \quad \left.+\beta(\omega_2)H_1(\omega_2)\beta(\omega_3)H_1(\omega_3)\right]\exp(j(\omega_1+\omega_2+\omega_3)t) = \\
& 6g_{3,M}g_{1,A}^2R^2\overline{\left\{\beta(\omega_{q_1})H_1(\omega_{q_1})\beta(\omega_{q_2})H_1(\omega_{q_2})\right\}_{\omega_1,\omega_2,\omega_3}}\exp(j(\omega_1+\omega_2+\omega_3)t)
\end{aligned} \tag{5.46}$$

$$\begin{aligned}
& -g_{3,M} g_{1,A}^3 R^3 \left(\beta(\omega) i_{ds,M_2(1)}(t) \right)^3 \Big|_{\omega_1, \omega_2, \omega_3} = \\
& -g_{3,M} g_{1,A}^3 R^3 \frac{1}{2^3} \sum_{q_1=1}^3 \sum_{q_2=1}^3 \sum_{q_3=1}^3 \left[\cancel{V_{in,q_1}} \cancel{V_{in,q_2}} \cancel{V_{in,q_3}} \beta(\omega_{q_1}) H_1(\omega_{q_1}) \beta(\omega_{q_2}) H_1(\omega_{q_2}) \times \right. \\
& \qquad \qquad \qquad \left. \beta(\omega_{q_3}) H_1(\omega_{q_3}) \exp(j(\omega_{q_1} + \omega_{q_2} + \omega_{q_3})t) \right] = \\
& -6g_{3,M} g_{1,A}^3 R^3 \beta(\omega_1) \beta(\omega_2) \beta(\omega_3) H_1(\omega_1) H_1(\omega_2) H_1(\omega_3) \exp(j(\omega_1 + \omega_2 + \omega_3)t)
\end{aligned} \tag{5.47}$$

$$\begin{aligned}
& +2g_{2,A} R^2 i_{ds,M_2(1)}(t) i_{ds,M_2(2)}(t) \Big|_{\omega_1, \omega_2, \omega_3} = \\
& +2g_{2,A} R^2 \left[\frac{1}{2} \sum_{q_1=1}^3 \cancel{V_{in,q_1}} H_1(\omega_{q_1}) \exp(j\omega_{q_1} t) \right] \times \\
& \qquad \qquad \qquad \left[\frac{1}{2} \sum_{q_2=1}^3 \sum_{q_3=1}^3 \cancel{V_{in,q_2}} \cancel{V_{in,q_3}} H_2(\omega_{q_2}, \omega_{q_3}) \exp(j(\omega_{q_2}, \omega_{q_3})t) \right] = \\
& +4g_{2,A} R^2 \left[H_1(\omega_1) H_2(\omega_2, \omega_3) + H_1(\omega_2) H_2(\omega_1, \omega_3) \right. \\
& \qquad \qquad \qquad \left. + H_1(\omega_3) H_2(\omega_1, \omega_2) \right] \exp(j(\omega_1 + \omega_2 + \omega_3)t) = \\
& +4g_{2,A} R^2 \overline{\left\{ H_1(\omega_{q_1}) H_2(\omega_{q_2}, \omega_{q_3}) \right\}}_{\omega_1, \omega_2, \omega_3} \exp(j(\omega_1 + \omega_2 + \omega_3)t)
\end{aligned} \tag{5.48}$$

$$\begin{aligned}
& g_{3,A} R^3 \left(1 - g_{1,M} \beta(\omega) \right) \left(i_{ds,M_2(1)}(t) \right)^3 \Big|_{\omega_1, \omega_2, \omega_3} = \\
& g_{3,A} R^3 \sum_{q_1=1}^3 \sum_{q_2=1}^3 \sum_{q_3=1}^3 \left[\cancel{V_{in,q_1}} \cancel{V_{in,q_2}} \cancel{V_{in,q_3}} \left(1 - g_{1,M} \beta(\omega_{q_1} + \omega_{q_2} + \omega_{q_3}) \right) \times \right. \\
& \qquad \qquad \qquad \left. H_1(\omega_{q_1}) H_1(\omega_{q_2}) H_1(\omega_{q_3}) \exp(j(\omega_{q_1} + \omega_{q_2} + \omega_{q_3})t) \right] = \\
& = 6g_{3,A} R^3 \left(1 - g_{1,M} \beta(\omega_1 + \omega_2 + \omega_3) \right) H_1(\omega_1) H_1(\omega_2) H_1(\omega_3) \exp(j(\omega_1 + \omega_2 + \omega_3)t)
\end{aligned} \tag{5.49}$$

Substituting Eq. 5.37 and 5.39-5.49 into Eq. 5.36 is given:

$$\begin{aligned}
H_3(\omega_1, \omega_2, \omega_3) &= \frac{1}{6(1 + g_{1,A}R \llbracket g_{1,M}\beta(\omega_1 + \omega_2 + \omega_3) - 1 \rrbracket)} \times \\
&\left\{ 4g_{2,A}R^2 \llbracket 1 - g_{1,M}\beta(\omega_1 + \omega_2 + \omega_3) \rrbracket \overline{\{H_1(\omega_{q_1})H_2(\omega_{q_2}, \omega_{q_3})\}}_{\omega_1, \omega_2, \omega_3}} + 4g_{2,M}g_{1,A}^2R^2 \times \right. \\
&\overline{\{\beta(\omega_{q_1})H_1(\omega_{q_1})\beta(\omega_{q_2} + \omega_{q_3})H_2(\omega_{q_2}, \omega_{q_3})\}}_{\omega_1, \omega_2, \omega_3}} + \left[6g_{3,A} \llbracket 1 - g_{1,M}\beta(\omega_1 + \omega_2 + \omega_3) \rrbracket \right. \\
&+ 4g_{2,M}g_{1,A}g_{2,A} \overline{\{\beta(\omega_{q_1})\beta(\omega_{q_2} + \omega_{q_3})\}}_{\omega_1, \omega_2, \omega_3}} - 6g_{3,M}g_{1,A}^3\beta(\omega_1)\beta(\omega_2)\beta(\omega_3) \left. \right] R^3 H_1(\omega_1) \\
&\times H_1(\omega_2)H_1(\omega_3) - 4g_{2,M}g_{1,A}R \overline{\{\beta(\omega_{q_1} + \omega_{q_2})H_2(\omega_{q_1}, \omega_{q_2})\}}_{\omega_1, \omega_2, \omega_3}} + 6g_{3,M} \left[1 - g_{1,A}R \times \right. \\
&\left. \overline{\{\beta(\omega_{q_1})H_1(\omega_{q_1})\}}_{\omega_1, \omega_2, \omega_3}} \right] - \left\{ R^2 \left[4g_{2,M}g_{2,A}\beta(\omega_{q_1} + \omega_{q_2}) - 6g_{3,M}g_{1,A}^2\beta(\omega_{q_1})\beta(\omega_{q_2}) \right] \times \right. \\
&\left. \overline{\{H_1(\omega_{q_1})H_1(\omega_{q_2})\}}_{\omega_1, \omega_2, \omega_3}} \right\}
\end{aligned} \tag{5.50}$$

So far, all the Volterra kernels required for IIP3 computation are collected. The reminded task is to prepare and substitute them in A.20. Based on this explanation the $H_1(\omega)$ and $H_1(-\omega)$, $H_2(\omega, \omega)$ and $H_2(\omega, -\omega)$, and $H_3(\omega, \omega, -\omega)$ is calculated from Eq. 5.23, 5.32, and 5.50, respectively, as follow:

$$H_1(\omega) = \frac{g_{1,M}}{1 + \llbracket g_{1,M}\beta(\omega) - 1 \rrbracket g_{1,A}R} \tag{5.51}$$

$$H_1(-\omega) = \frac{g_{1,M}}{1 - \llbracket g_{1,M}\beta(\omega) + 1 \rrbracket g_{1,A}R} \tag{5.52}$$

$$\begin{aligned}
H_2(\omega, \omega) &= \frac{1}{1 + g_{1,A}R(g_{1,M}\beta(2\omega) - 1)} \times \\
&\left\{ g_{2,M} - 2g_{2,M}g_{1,A}R\beta(\omega)H_1(\omega) + \left[g_{2,M}g_{1,A}^2\beta^2(\omega) - g_{1,M}g_{2,A}\beta(2\omega) + g_{2,A} \right] R^2 H_1^2(\omega) \right\}
\end{aligned} \tag{5.53}$$

$$\begin{aligned}
H_2(\omega, -\omega) &= \frac{1}{1 + (g_{1,M}\beta(0) - 1)g_{1,A}R} \times \\
&\{g_{2,M} - g_{2,M}g_{1,A}R[\beta(\omega)H_1(\omega) - \beta(\omega)H_1(-\omega)] + \\
&\quad [-g_{2,M}g_{1,A}^2\beta^2(\omega) - g_{1,M}g_{2,A}\beta(0) + g_{2,A}]R^2H_1(\omega)H_1(-\omega)\}
\end{aligned} \tag{5.54}$$

$$\begin{aligned}
H_3(\omega, \omega, -\omega) &= \frac{1}{6(1 + g_{1,A}R\llbracket g_{1,M}\beta(\omega) - 1 \rrbracket)} \times \\
&\{4g_{2,A}R^2\llbracket 1 - g_{1,M}\beta(\omega) \rrbracket\{2H_1(\omega)H_2(\omega, -\omega) + H_1(-\omega)H_2(\omega, \omega)\} \\
&+ 4g_{2,M}g_{1,A}^2R^2\beta(\omega)\{2\beta(0)H_1(\omega)H_2(\omega, -\omega) - \beta(2\omega)H_1(-\omega)H_2(\omega, \omega)\} \\
&+ \llbracket 6g_{3,A}\llbracket 1 - g_{1,M}\beta(\omega) \rrbracket + 4g_{2,M}g_{1,A}g_{2,A}\beta(\omega)\{2\beta(0) - \beta(2\omega)\} \\
&+ 6g_{3,M}g_{1,A}^3\beta^3(\omega)\rrbracket R^3H_1^2(\omega)H_1(-\omega) + 6g_{3,M}\llbracket 1 - g_{1,A}R\beta(\omega)(2H_1(\omega) - H_1(-\omega)) \rrbracket \\
&- 4g_{2,M}g_{1,A}R\{2\beta(0)H_2(\omega, -\omega) + \beta(2\omega)H_2(\omega, \omega)\} + \llbracket 6g_{3,M}g_{1,A}^2\beta^2(\omega) \times \\
&(H_1(\omega) - 2H_1(-\omega)) - 4g_{2,M}g_{2,A}(\beta(2\omega)H_1(\omega) + 2\beta(0)H_1(-\omega)) \rrbracket R^2H_1(\omega)\}
\end{aligned} \tag{5.55}$$

Due to the fact that the feedback factor is almost equal to zero at low frequencies, ($\beta(0) \approx 0$), Eq. 5.54 and 5.55 would simplified as:

$$\begin{aligned}
H_2(\omega, -\omega) &= \frac{1}{1 - g_{1,A}R} \times \\
&\{g_{2,M} - g_{2,M}g_{1,A}R[\beta(\omega)H_1(\omega) - \beta(\omega)H_1(-\omega)] + \\
&\quad [-g_{2,M}g_{1,A}^2\beta^2(\omega) + g_{2,A}]R^2H_1(\omega)H_1(-\omega)\}
\end{aligned} \tag{5.56}$$

$$\begin{aligned}
H_3(\omega, \omega, -\omega) &= \frac{1}{6(1 + g_{1,A}R[g_{1,M}\beta(\omega) - 1])} \times \\
&\{4g_{2,A}R^2[1 - g_{1,M}\beta(\omega)]\{2H_1(\omega)H_2(\omega, -\omega) + H_1(-\omega)H_2(\omega, \omega)\} \\
&\quad + [1 + g_{1,A}R\beta(\omega)H_1(-\omega)][6g_{3,M} - 4g_{2,M}g_{1,A}R\beta(2\omega)H_2(\omega, \omega)] \\
&\quad + [6g_{3,A}[1 - g_{1,M}\beta(\omega)] - 4g_{2,M}g_{1,A}g_{2,A}\beta^2(\omega)\beta(2\omega) + 6g_{3,M}g_{1,A}^3\beta^3(\omega)] \times \\
&\quad \quad R^3H_1^2(\omega)H_1(-\omega) + 6g_{3,M}[1 - 2g_{1,A}R\beta(\omega)H_1(\omega)] \\
&\quad + [6g_{3,M}g_{1,A}^2\beta^2(\omega)(H_1(\omega) - 2H_1(-\omega)) - 4g_{2,M}g_{2,A}\beta(2\omega)H_1(\omega)]R^2H_1(\omega)\}
\end{aligned} \tag{5.57}$$

Assuming $R \approx 1/g_{1,M}$, $g_{2,A} \approx 0$, and $g_{1,A} = \alpha g_{1,M}$, where $\alpha < 1$, Eq. 5.51 and 5.57 would be:

$$H_1(\omega) = \frac{g_{1,M}}{1 + [g_{1,M}\beta(\omega) - 1]g_{1,A}R} \tag{5.58}$$

$$H_3(\omega, \omega, -\omega) = \frac{A_{3,M}(\omega)g_{3,M} - A_{3,A}(\omega)g_{3,A} + A_{3,2}(\omega)g_{2,M}^2}{A_{3,D}(\omega)} \tag{5.59}$$

where

$$\begin{aligned}
A_{3,M}(\omega) &= \left[-2 + \alpha(6 - g_{1,M}\beta(\omega)) - \alpha^2(7 - (1 + g_{1,M}\beta(\omega))^2) \right. \\
&\quad \left. + \alpha^3(2 - g_{1,M}\beta(\omega) - g_{1,M}^2\beta^2(\omega) + g_{1,M}^3\beta^3(\omega)) \right]
\end{aligned} \tag{5.60}$$

$$\begin{aligned}
A_{3,2}(\omega) &= 2\alpha(1 - \alpha)\beta(2\omega) \times \\
&\quad [1 - 2\beta(\omega) - 2\alpha(1 - \beta(\omega))(1 - g_{1,M}\beta(\omega)) + \alpha^2(1 - 2g_{1,M}\beta(\omega) + 2g_{1,M}^2\beta^2(\omega))]
\end{aligned} \tag{5.61}$$

$$A_{3,A}(\omega) = 3(1 - g_{1,M}\beta(\omega))[1 - 3\alpha(1 - g_{1,M}\beta(2\omega))] \tag{5.62}$$

$$A_{3,D}(\omega) = -3[1 + \alpha(\beta(\omega)g_{1,M} - 1)]^3[1 - \alpha(1 + g_{1,M}\beta(\omega))][1 - \alpha(1 - g_{1,M}\beta(2\omega))] \tag{5.63}$$

Consequently, by applying Eq. 5.58 and 5.59 in Eq. A.20 it can be concluded to:

$$IIP3 = \sqrt{\frac{4|-g_{1,M}A_{Num}(\omega)|}{3\left[1 + \alpha(\beta(\omega)g_{1,M} - 1)\right]\{A_{D,M}(\omega)g_{3,M} - A_{D,A}(\omega)g_{3,A} + A_{D,2}(\omega)g_{2,M}^2\}}} \quad 5.64$$

where

$$A_{D,M}(\omega) = \left[-2 + \alpha(6 - g_{1,M}\beta(\omega)) - \alpha^2(7 - (1 + g_{1,M}\beta(\omega))^2) + \alpha^3(2 - g_{1,M}\beta(\omega) - g_{1,M}^2\beta^2(\omega) + g_{1,M}^3\beta^3(\omega)) \right] \quad 5.65$$

$$A_{D,2}(\omega) = 2\alpha(1 - \alpha)\beta(2\omega) \times \left[1 - 2\beta(\omega) - 2\alpha(1 - \beta(\omega))(1 - g_{1,M}\beta(\omega)) + \alpha^2(1 - 2g_{1,M}\beta(\omega) + 2g_{1,M}^2\beta^2(\omega)) \right] \quad 5.66$$

$$A_{D,A}(\omega) = 3(1 - g_{1,M}\beta(\omega)) \left[1 - \alpha(1 - g_{1,M}\beta(2\omega)) \right] g_{3a} \quad 5.67$$

$$A_{Num}(\omega) = \left[1 - \alpha(1 + g_{1,M}\beta(\omega)) \right] \left[1 + \alpha(\beta(\omega)g_{1,M} - 1) \right]^3 \quad 5.68$$

As it is apparent from the above analytical derivations, this method takes into account a wider range of nonlinear elements' effects, as compared to the pervious works. In fact, considering the more derivative orders of the auxiliary current allows for a comprehensive description of the feedback impact, as well as providing a higher level of linearity.

5.3.3 Noise Cancelation

One of the interesting points regarding to the CC-LNA with NF-IMS method compare to IMS method is its noise performance. As it is predictable, NF of a circuit would experience an increase when an additional active device like a transistor is added to its structure. This scenario will be applied to NF of the optimized CC-LNA when the IMS method and M_{Aux} present to it. However, the NF-IMS method restores some of these noise performance side effects. In other words, the proposed method shows a degree of noise cancellation behavior, which promotes a decrease in NF_{NF-IMS} respect to NF_{IMS} . To have been better over-view on this improvement, the mean square of noise at node Q due to the channel thermal noise sources of M_{Main} and M_{Aux}

provides an essential comparison means for us. Thus, applying Kirchhoff's current and voltage law (KCL and KVL), the $\overline{v_Q}$ for CC-LNA with IMS and NF-IMS will calculate as follows:

$$\overline{v_{Q,IMS}^2} = \frac{\overline{i_{nd,M}^2} + (1 + \omega^2 g_{m,M}^2 L_S^2) \overline{i_{nd,A}^2}}{(1 + \omega^2 g_{m,M}^2 L_S^2)(g_{m,2} + g_{m,A})^2} \quad 5.69$$

$$\overline{v_{Q,NFIMS}^2} = \frac{\overline{i_{nd,M}^2} + (1 + \omega^2 g_{m,M}^2 L_{S1}^2) \overline{i_{nd,A}^2}}{(g_{m,2} + g_{m,A})^2 + \omega^2 [(g_{m,2} + g_{m,A}) g_{m,M} L_{S1} + g_{m,M} g_{m,2} L_{S2}]^2} \quad 5.70$$

Where $i_{nd,M}$ and $i_{nd,A}$ represent the channel thermal noise sources of main and auxiliary transistors, respectively. Assuming $L_{S1} = \eta L_S$, $L_{S2} = (1 - \eta) L_S$, and $g_{m,2} = \sigma g_{m,M}$ where $\sigma > 1$. Substituting them in Eq. 5.69 and 5.70 lead to:

$$\overline{v_{Q,IMS}^2} = \frac{\overline{i_{nd,M}^2} + (1 + \omega^2 g_{m,M}^2 L_S^2) \overline{i_{nd,A}^2}}{(1 + \omega^2 g_{m,M}^2 L_S^2)(\sigma + \alpha)^2 g_{m,M}^2} \quad 5.71$$

$$\overline{v_{Q,NFIMS}^2} = \frac{\overline{i_{nd,M}^2} + (1 + \eta^2 \omega^2 g_{m,M}^2 L_S^2) \overline{i_{nd,A}^2}}{\{(\sigma + \alpha)^2 + \omega^2 (\sigma + \eta \alpha)^2 g_{m,M}^2 L_S^2\} g_{m,M}^2} \quad 5.72$$

A comparison between Eq. 5.71 and 5.72 shows a roughly 10% improvement in NF_{NF-IMS} . A comprehensive explanation to this phenomenon is the noise source of the main transistor presents two voltages with opposite phase at the drain and source of it. Later, the drain noise will be sampled by the auxiliary pass and added to the source node. Because of the phase difference, they would nullify each other. The same story could be applied to $i_{nd,A}$ while this time the main transistor samples the drain of auxiliary one.

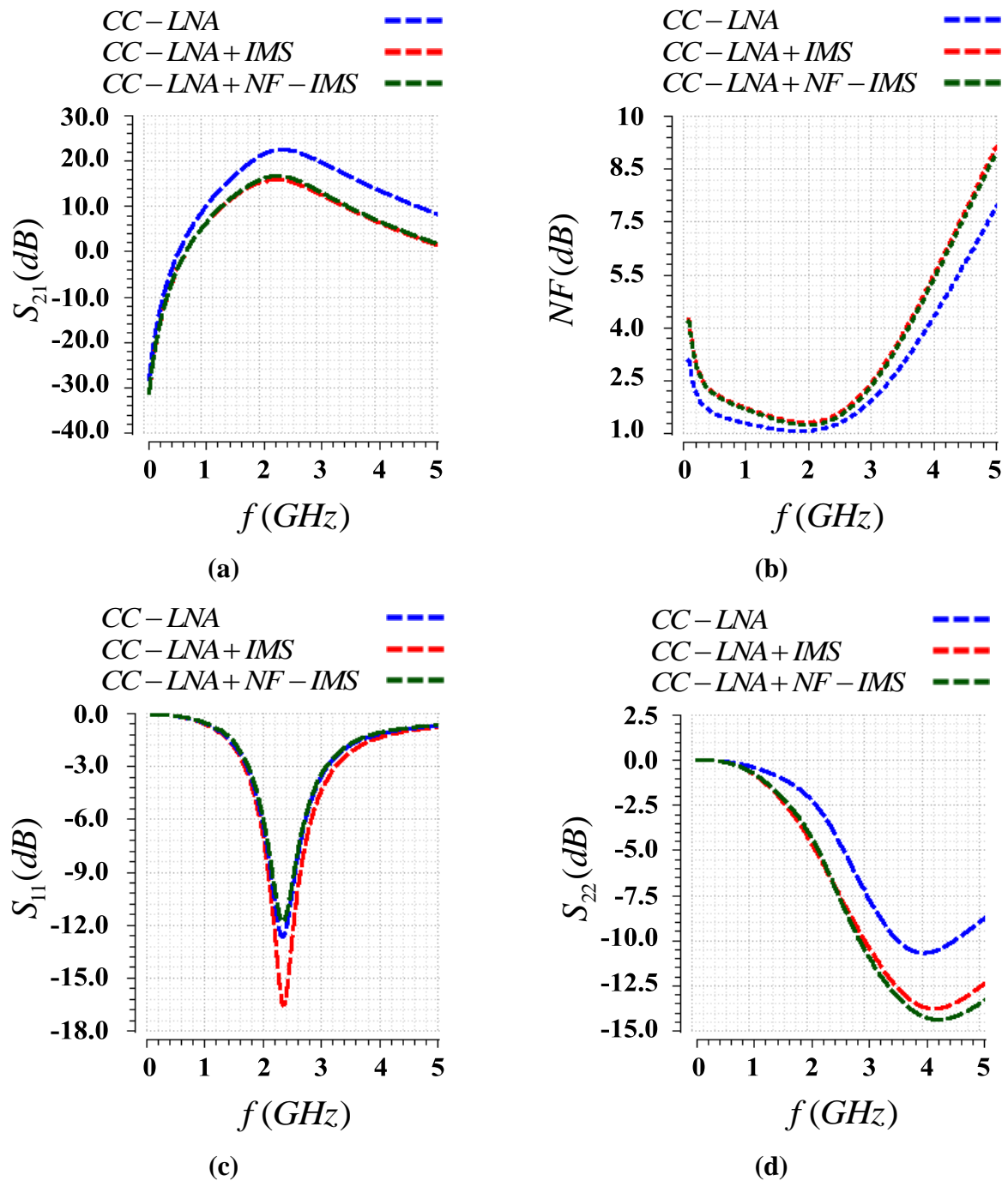


Figure 5.3: The S-parameters and NF result of CC-LNA with and without nonlinearity enhancement.

5.4 Simulation and Results

The NF-IMS method parameters' specifications are discussed as follow; first, the transistor, capacitors, and inductor size of the core LNA are optimized with respect to gain, NF, input matching, and power consumption. Then, the size and number of fingers of the auxiliary transistor is investigated to achieve a maximum IIP3 and minimum DC power.

To increase the practical reliability of this simulation, we employ the real element model from TSMC 65nm CRN65GP rather than the ideal one. Besides, in order to simulate and measure the IIP3, the two-tone test is conducted by applying harmonic balance analysis. To indicate the robustness of proposed method, the selected tones are absolutely close to each other with 1MHz frequency separation.

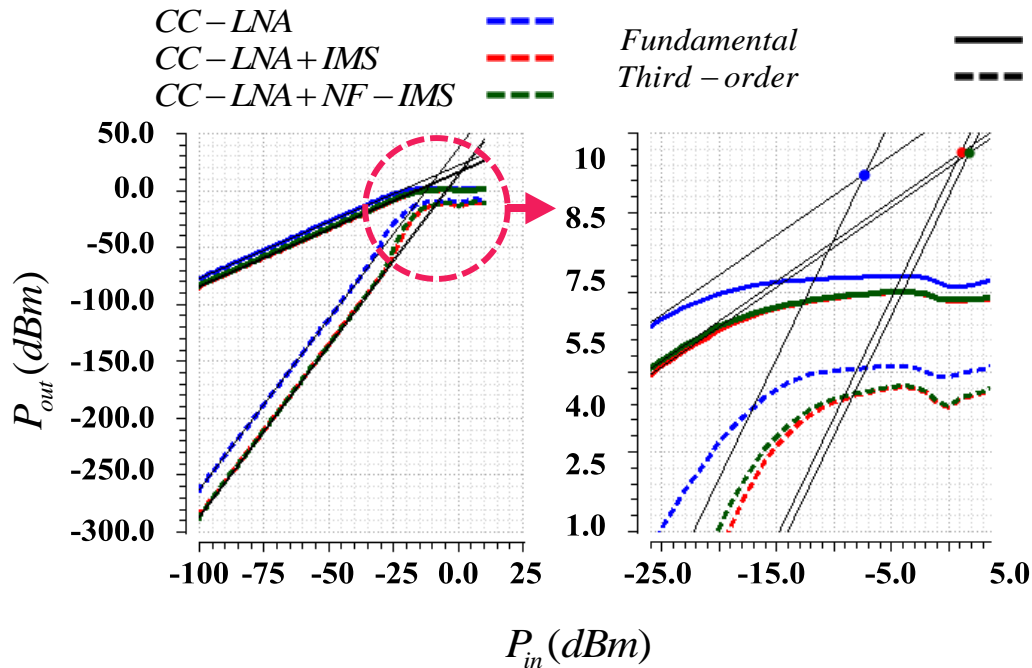


Figure 5.4: IIP3 result of CC-LNA with and without nonlinearity enhancement.

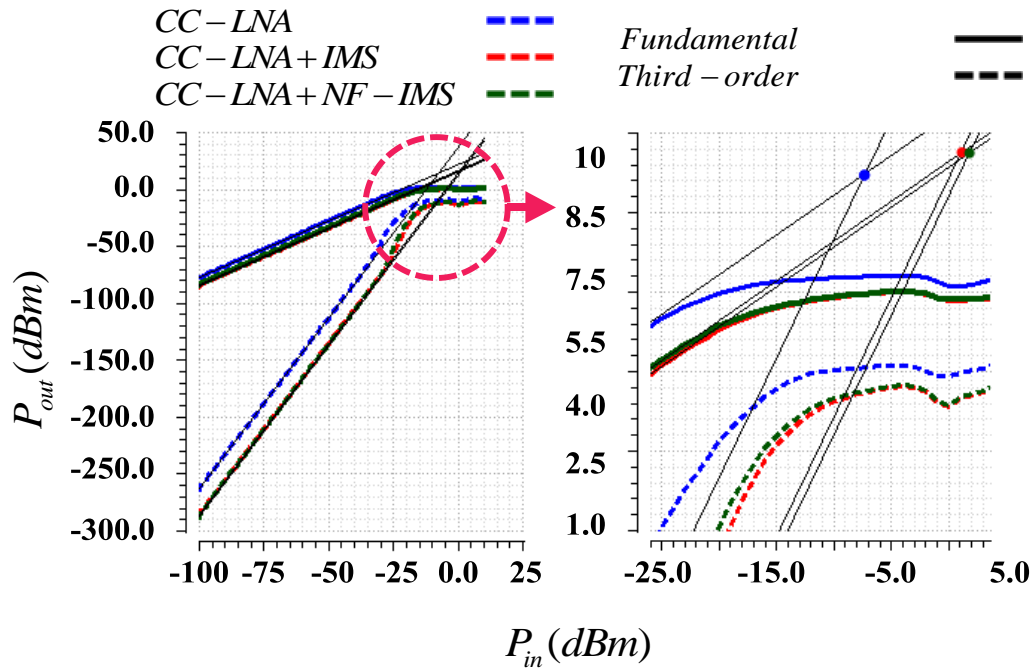


Figure 5.5: IIP3 as function of PMOS's width for auxiliary biasing equals to 0V.

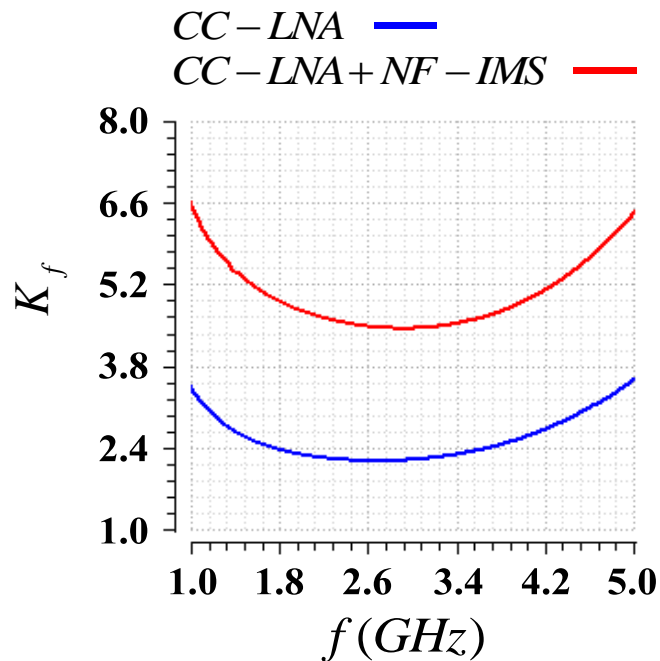


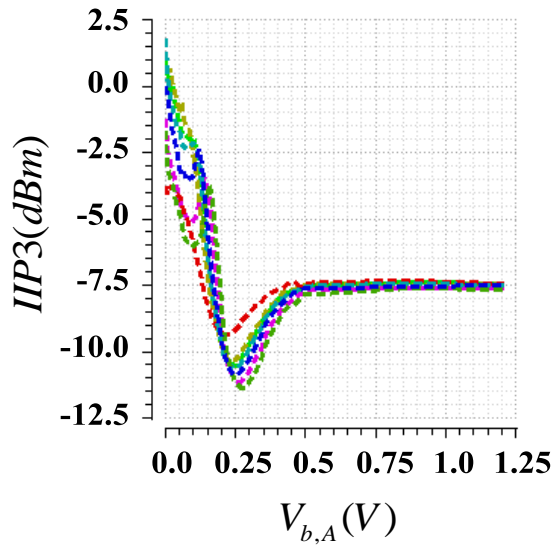
Figure 5.6: IIP3 as function of PMOS's width for auxiliary biasing equals to 0V.

As depicted in Figure 5.3 and Figure 5.4, the designed CC-LNA with real model elements presents 22.4dB gain (S_{21}), 1.24dB NF, -12.38dB input impedance matching (S_{11}), -7.44dBm IIP3, and 12.62mW power consumptions from a 1.2V power supply. Moreover, Fig. 7 represents that the minimum unconditional stability (K_f) factor is 2.2 at 2.4GHz.

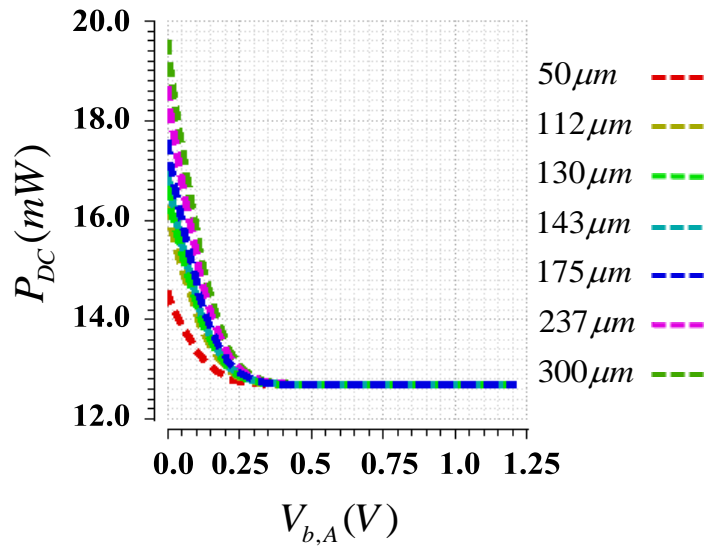
Based on the (24), the variable α plays a critical role in IIP3 calculation. Due to the fact that CC-LNA parameters are constant and they would not be affected by linearization methods, α can be considered just as function of the width and gate biasing of the PMOS. It allows us to assume the variation of IIP3 as a function of the auxiliary transistor's width and biasing. The demonstrated curve in Figure 5.5 reveals the relation between IIP3 and the PMOS's width. In addition, the variation of IIP3 and DC power as function of auxiliary transistor's gate biasing are shown in Figure 5.7.a and 5.7.b, respectively. As it is apparent, the optimum value for the IIP3 is occurs for the PMOS with 140 μ m width and a gate bias of 0V. As depicted in Figure 5.7.c and 5.7.d, the relation between the linearity and the number of the fingers for the auxiliary transistor is not as effective as width of the PMOS. In other words, the IIP3 and power consumption are not sensitive to number of fingers.

Base on the above consideration and results of Figure 5.3 and Figure 5.4, the designed LNA with NF-IMS method presents a maximum S_{21} of 16.67dB, minimum S_{11} of -11.78dB, 1.26dB NF_{min} , and 2.08dBm IIP3, while dissipate 16.9mW power from a 1.2V power supply. Consistently with our expectation, the negative feedback improves the unconditional stability factor. The new $K_{f,min}$ is 4.8 which are two times larger than the previous one (Fig. 7).

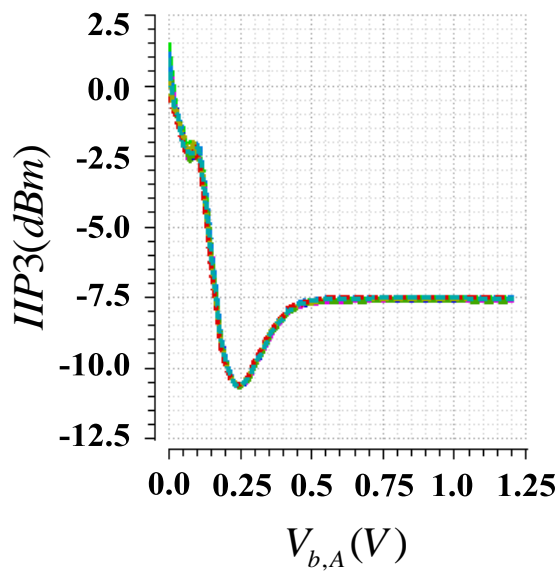
Based on the above results, it's clear that the NF-IMS method had been strongly improved the CC-LNA characteristics. However, to prove the effectiveness of the proposed NF-IMS method, an investigation could be conducted between the IMS method's results and the above ones. To have a fairly comparison, the size and biasing of transistors, value of the passive element, and power's level of the input signal are identical for the both tests. As Figure 5.3 and Figure 5.4 demonstrate, the designed CC-LNA with IMS methods shows the maximum forward



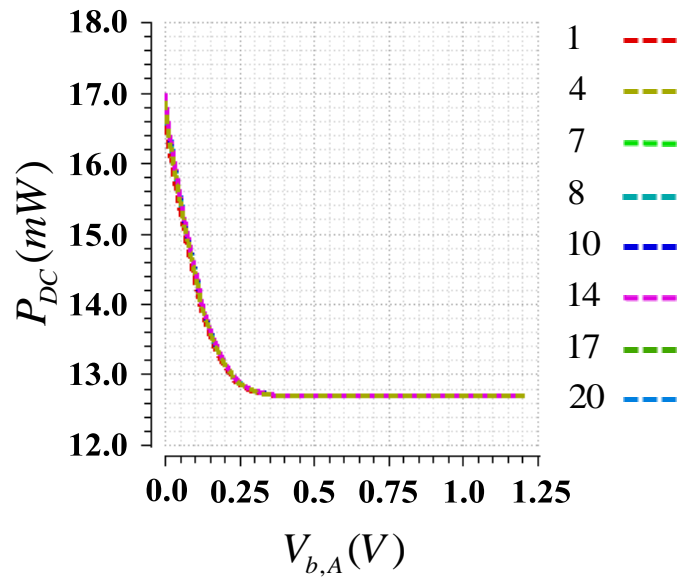
(a)



(b)



(c)



(d)

Figure 5.7: IIP3 and dissipation power as function of the auxiliary transistor; (a) and (b) width and biasing, (c) and (d) number of fingers and biasing

gain (S_{21}) of 15.83dB, -16.56dB as the minimum input return loss (S_{11}), 1.51dB for the minimum NF, and IIP3 of 0.54dBm, while consumes 16.88mW from 1.2V power supply.

A simple calculation reveals the 1.5dBm improvement in IIP3 of NF-IMS method compares to the IMS one. In addition to nonlinearity, it's also slightly enhancing the S_{21} and NF while dissipating almost same power as IMS method uses.

5.5 Conclusion

A CMOS LNA designed based on NF-LMS methods has been presented. As a result of the negative feedback, a highly linear amplifier is proposed with unconditional stability and low power consumption. According to the analyses and simulations, the suggested design provides more than 9dBm IIP3 improvement, while presenting as high gain as 16.67.6dB. The designed LNA based on this method could be employed as best candidate for the WBAN and WPAN gateway's receiver due to its high linearity characteristics.

Chapter 6

Conclusion and Future work

6.1 Conclusion

In this thesis a new optimization technique have been presented for the CMOS inverter LNA. The proposed technique provides the ability of optimizing two transistors simultaneously and taking into account all effective noise sources of inverter topology. Applying this optimization approach, a novel high gain, low power, CMOS low noise current reused LNA circuit has been designed for the WBAN applications, which employs noise optimization technique to achieve higher performance. The suggested solution applies noise equations to achieve low noise figure and high gain simultaneously. The presented theoretical analyses and design methodologies are aimed to cover the weakness of previous reported techniques. The theoretical procedure involved fundamental concept and principals of noise parameters expressions and provided critical assumptions to simplify the complicated relationships between noise parameters and circuit elements. Considering the fact that there is no pure analytic approach for acceptable optimizing of CMOS inverter several numerical investigation and simulations where utilized to obtained optimum values.

The LNA's circuit has been designed and simulated based on IBM 0.13 μm and TSMC 65 nm. The circuit attained 28.5 dB gain, 2.4 dB noise figure, -18 dB impedance matching, and power dissipating less than 1mW at 2.4 GHz frequency.

In addition, a novel linearization technique was introduced based on the Cascaded-LNA (CC-LNA) structure. Utilizing this technique, we attained a highly linear device that provides a 1.5dB IIP3 improvement without affecting NF or gain. This architecture was aimed to be used in gateway applications. The importance of the suggested method will be more clear by considering the fact that no extra element was used in the structure.

6.2 Future work

There are several improvements can be applied to the techniques and designs that was described. The optimization technique that was presented in chapter Chapter 3 is capable to

apply to the other frequency bands of NB-WBAN. It would be good practice to design the CICR LNA for the lower frequency as well as UWB-WBAN frequencies.

The inductors used in the LNAs were modeled with the inductor model kits from the either IBM 0.13 μm or TSMC 65 nm design kits. Although, these models were carried out at the time of the design, the extended model form an electromagnetic (EM) simulator can improve the accuracy of simulation.

Besides the above design enhancement, providing layout, chip fabrication, and test and measurement are of other future works.

Appendix A

Volterra Series Tutorial

A.1. History

The low noise amplifiers should be analyzed as a weakly nonlinear time invariant system with memory effects, in which the term “weakly nonlinear” denotes the condition of small input excitation that can be modeled with polynomials. The memory effect is originated from energy storage elements such as capacitors and inductors in which the output is depended to both the current input and the previous one. At high frequencies, unlike the low frequencies, there is not sufficient time for discharging the pervious input thoroughly. Thus, memory effects must be taken into the account. Taylor series is not efficient in predicting high-frequency-low-distortion terms due to the discrepancy of the analysis. The power-series analysis is also improper for LNA analyzing since it can be applied only for the systems with separated frequency-sensitive linear part from memory less nonlinear elements, as shown in Figure A.1.a. As a result, the best method for analyzing such a system is the Volterra series, which is valid for weakly nonlinear systems.

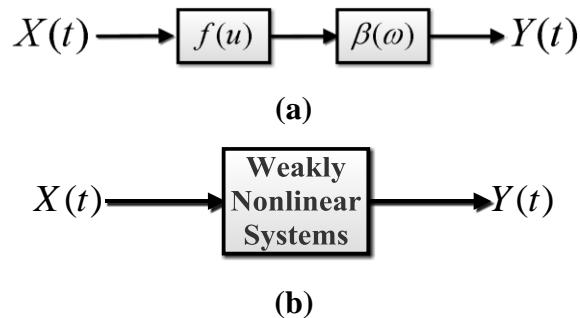


Figure A.1: a) Typical nonlinear system with memory effects, b) Weakly nonlinear system model for Volterra series analysis.

A.2. Volterra Series Analysis

In the theory of linear systems, it is postulated that the output $Y(t)$ can be written as:

$$Y(t) = \int_{-\infty}^{\infty} h(\tau)X(t-\tau)d\tau \quad \text{A.1}$$

where $h(t)$ denotes the impulse response to the Direct-delta function ($\delta(t)$) [93]. Figure A.1.b shows the model employed for Volterra-series approach, in which the circuit could be a combination of linear and nonlinear elements and may have memory or feedback. They also can be resistive or reactive. The excitation $X(t)$ is a series of a number of individual sinusoidal components of non-commensurate frequencies. The voltage corresponds to $X(t)$ can be written as:

$$X(t) = \frac{1}{2} \sum_{q_1=1}^Q V_{X,q_1} \exp(j\omega_{q_1} t) + V_{X,q_1}^* \exp(-j\omega_{q_1} t) = \frac{1}{2} \sum_{\substack{q_1=-Q \\ q_1 \neq 0}}^Q V_{X,q_1} \exp(j\omega_{q_1} t) \quad \text{A.2}$$

where $V_{X,-q_1} = V_{X,q_1}^*$, $\omega_{-q_1} = -\omega_{q_1}$, V_{X,q_1}^* is the complex conjugate of $V_{X,-q_1}$, and we assume that there is no DC component in the excitation and the response. The only DC excitation component in RF systems is the bias which can be implicitly comprised by assessing the a_n coefficients at the bias point. However, the response of a nonlinear system to a sinusoidal excitation includes DC term. In a weakly nonlinear circuit with small excitation, this DC term is negligible. Thus, in LNA analysis the output DC component can only affects the bias currents and voltages offset. It is worth mentioning that in the case of high offset bias, neither power series nor volterra series is convenient. Considering the above assumption, the excitation $X(t)$, the incremental small signal voltage or current can be expressed as::

$$X(t) = \frac{1}{2} \sum_{q_1=-Q}^Q V_{X,q_1} \exp(j\omega_{q_1} t) \quad \text{A.3}$$

in which $q_1 \neq 0$. Norbert Wiener, who modified the Volterra series analysis to nonlinear systems, proved that the weakly nonlinear circuit with small excitations response can be presented as [73, 94]:

$$Y(t) = \int_{-\infty}^{\infty} h_1(\tau_1)X(t-\tau_1)d\tau_1 + \int_{-\infty}^{\infty} \int_{-\infty}^{\infty} h_2(\tau_1, \tau_2)X(t-\tau_1)X(t-\tau_2)d\tau_1d\tau_2 + \dots \quad A.4$$

where $h_n(\tau_1, \tau_2, \dots, \tau_n)$ is the n th-order kernel (or nonlinear impulse response) and the nonlinear transfer function $H_n(\omega_{q_1}, \omega_{q_2}, \dots, \omega_{q_n})$ is its n -dimensional Fourier and transform. It can be shown that this series is convergent and magnitude of each consecutive term is less than the previous one. We can rewrite Eq. A.4 in the compact form with limited series to N terms (N th-order) as:

$$Y(t) = \sum_{n=1}^N Y_n(t) \quad A.5$$

where

$$Y_n(t) = \int_{-\infty}^{\infty} \int_{-\infty}^{\infty} \dots \int_{-\infty}^{\infty} h_n(\tau_1, \tau_2, \dots, \tau_n)X(t-\tau_1)X(t-\tau_2)\dots X(t-\tau_n)d\tau_1d\tau_2\dots d\tau_n \quad A.6$$

By replacing Eq. A.3 into Eq. A.6 and applying the interchange methodology of the order of integration and summation, the frequency-domain response will be obtained as:

$$Y_n(t) = \frac{1}{2^n} \sum_{q_1=-Q}^Q \sum_{q_2=-Q}^Q \dots \sum_{q_n=-Q}^Q \left[V_{X,q_1} V_{X,q_2} \dots V_{X,q_n} \exp(j(\omega_{q_1} + \omega_{q_2} + \dots + \omega_{q_n})t) \right. \\ \left. \times \int_{-\infty}^{\infty} \int_{-\infty}^{\infty} \dots \int_{-\infty}^{\infty} h_n(\tau_1, \tau_2, \dots, \tau_n) \exp(-j(\omega_{q_1}\tau_1 + \omega_{q_2}\tau_2 + \dots + \omega_{q_n}\tau_n)) d\tau_1d\tau_2\dots d\tau_n \right] \quad A.7$$

where $q_i \neq 0$ and the last term of Eq. A.7 is known as multidimensional Fourier transform:

$$H_n(\omega_{q_1}, \omega_{q_2}, \dots, \omega_{q_n}) = \int_{-\infty}^{\infty} \int_{-\infty}^{\infty} \dots \int_{-\infty}^{\infty} \left[h_n(\tau_1, \tau_2, \dots, \tau_n) \right. \\ \left. \times \exp(-j(\omega_{q_1}\tau_1 + \omega_{q_2}\tau_2 + \dots + \omega_{q_n}\tau_n)) d\tau_1d\tau_2\dots d\tau_n \right] \quad A.8$$

from which, the nonlinear impulse response can be attained through inverse-Fourier transform:

$$h_n(\tau_1, \tau_2, \dots, \tau_n) = \frac{1}{(2\pi)^2} \int_{-\infty}^{\infty} \int_{-\infty}^{\infty} \dots \int_{-\infty}^{\infty} \left[H_n(\omega_{q_1}, \omega_{q_2}, \dots, \omega_{q_n}) \right. \\ \left. \times \exp(j(\omega_{q_1} \tau_1 + \omega_{q_2} \tau_2 + \dots + \omega_{q_n} \tau_n)) d\omega_{q_1} d\omega_{q_2} \dots d\omega_{q_n} \right] \quad \text{A.9}$$

As a result, the frequency domain response will be achieved as:

$$Y_n(t) = \frac{1}{2^n} \sum_{q_1=-Q}^Q \sum_{q_2=-Q}^Q \dots \sum_{q_n=-Q}^Q \left[V_{X,q_1} V_{X,q_2} \dots V_{X,q_n} H_n(\omega_{q_1}, \omega_{q_2}, \dots, \omega_{q_n}) \right. \\ \left. \times \exp(j(\omega_{q_1} + \omega_{q_2} + \dots + \omega_{q_n})t) \right] \quad \text{A.10}$$

that summation of $Y_n(t)$ over $n=1,2,\dots,N$ results in $Y(t)$. in other words, by summing the individual n th-order responses, the final response will be attained. The advantage of Volterra series approach is that we can separate the mixing products of the same order. Furthermore, the nonlinear transfer function $H_n(\omega_{q_1}, \omega_{q_2}, \dots, \omega_{q_n})$ and the n th-order nonlinear impulse response $h_n(\tau_1, \tau_2, \dots, \tau_n)$ must be symmetrical in ω and τ , respectively. This statement will be clear by considering the fact that the excitation $X(t)$ does not have any order associated with different tones. As a result, permuting frequencies in $Y_n(t)$ should not change the response.

A.3. Nonlinear transfer function

Harmonic input or probing method is the technique to find the nonlinear transfer function. Assuming the excitation to be the simplest form of

$$X(t) = \exp(j\omega_1 t) + \exp(j\omega_2 t) + \dots + \exp(j\omega_n t) \quad \text{A.11}$$

The n th-order part of a nonlinear circuit response can be determined, according to A.10, as:

$$Y_n(t) = t_n H_n(\omega_1, \omega_2, \dots, \omega_n) \exp(j(\omega_1 + \omega_2 + \dots + \omega_n)t) \quad \text{A.12}$$

where t_n represents the number of specific term which is generated by the given multinomial coefficients of input excitations.

$$t_{n,k} = \frac{n!}{m_{-Q}! \dots m_{-1}! m_1! \dots m_Q!} \quad \text{A.13}$$

where n is the maximum possible number of all excitations for the particular n th-order term and the m_i is number of repetition for an individual excitation (ω_i). As a result, by replacing A.12 in the circuit equation and retaining the n th-order term, the nonlinear transfer function $H_n(\omega_{q_1}, \omega_{q_2}, \dots, \omega_{q_n})$ will be found. Since the n th-order nonlinear transfer function is depended on the transfer functions of the orders smaller than n , first we must employ $X(t) = \exp(j\omega_1 t)$ to calculate $H_1(\omega_1)$, and then $H_2(\omega_1, \omega_2)$ can be calculated by considering $X(t) = \exp(j\omega_1 t) + \exp(j\omega_2 t)$ and using $H_1(\omega_1)$ and $H_1(\omega_2)$. This procedure should be followed to obtain all orders. Then, by calculating $H_n(\omega_1, \omega_2, \dots, \omega_n)$ and applying A.10 and A.5 the desired frequency components level in the whole response can be determined.

A.4. Single tone formulation for IIP3

A single-tone expression for the third order intercept point (IP3) can be computed based on volterra kernels. The third order nonlinearity of the circuit with input tones of ω_1 and ω_2 is measured by IP3. As the input increases, these fundamental tones linearly increase with a slope of 1 in dB scale, however, the third order intermodulation (IM3) products ($2\omega_1 - \omega_2, 2\omega_2 - \omega_1$) grow linearly with a slop of 3. The intersection point of these line defined IP3. In other words, the input referred IP3 (IIP3) that is modulated by the system's gain is defined as output referred IP3 (OIP3), and can be expressed as [36]:

$$IIP3 = P_i + \frac{1}{2} [P_{o1} - P_{o3}] \quad \text{A.14}$$

where, P_i , P_{o1} , and P_{o3} are the input power, output power of the fundamental frequencies, and output power of the IM3 frequencies, respectively. There are two methods for obtaining IP3. One approach is a simulation based method and the other is analytical calculation of IP3 using Volterra kernels as follow [73]:

$$IIP3 = \sqrt{\frac{4|H_1(\omega_1)|}{3|H_1(\omega_1, \omega_1, -\omega_2)|}} \quad A.15$$

$$IIP3 = \sqrt{\frac{4|H_1(\omega_2)|}{3|H_1(\omega_2, \omega_2, -\omega_1)|}} \quad A.16$$

As the two fundamental tones of ω_1 and ω_2 are close to each other, we can write:

$$H_1(\omega_1) \approx H_1(\omega_2) \quad A.17$$

$$H_1(\omega_1, \omega_1, -\omega_2) \approx H_1(\omega_2, \omega_2, -\omega_1) \quad A.18$$

Thus, Eq. A.15 and A.16 can be used interchangeably. Once the Volterra kernels are obtained analytically for a frequency, IP3 can be calculated based on only a single tone (ω_1), since $\omega_1 \approx \omega_2$. Hence, we can have [95]:

$$|H_1(\omega_1, \omega_1, -\omega_2)| \approx |H_1(\omega_2, \omega_2, -\omega_1)| \quad A.19$$

$$IIP3 = \sqrt{\frac{4|H_1(\omega_1)|}{3|H_1(\omega_1, \omega_1, -\omega_1)|}} \quad A.20$$

which in dB scale will be as [62]:

$$IIP3_{dBm} = 20 \log_{10} \left(\sqrt{\frac{4|H_1(\omega_1)|}{3|H_1(\omega_1, \omega_1, -\omega_1)|}} \right) + 10dB \quad A.21$$

Although, IIP3 can be determined the capacitor and inductor memory and frequency effects, it does not take into account the effects of the elements that are not modeled in the transistor's equivalent circuit, such as body effect, parasitic capacitances, C_{gs} bias-dependency, gate/source resistance, and channel length modulation. The following flow chart summarized the Volterra kernel's derivation process to be used in IIP3 calculation.

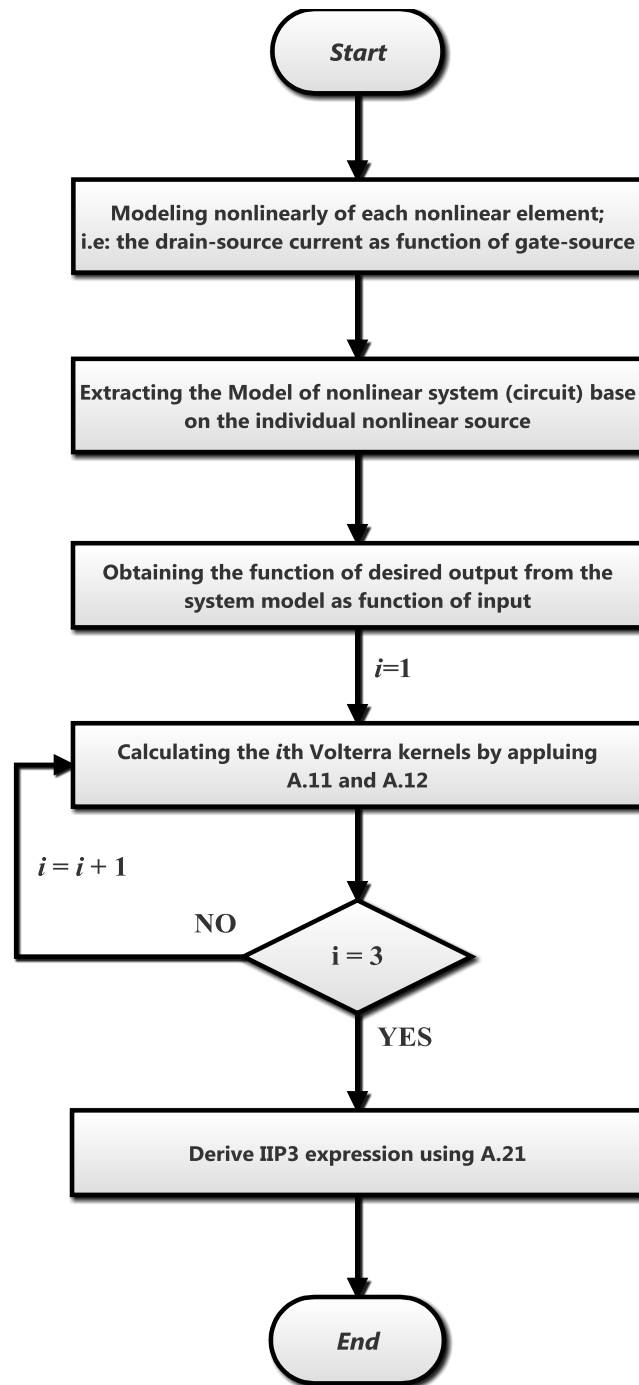


Figure A.2:IIP3 calculation flowchart of a nonlinear system.

Bibliography

- [1] B. Razavi, *RF Microelectronics*, 2nd ed.: Prentice Hall, 2011.
- [2] H. A. Haus, W. R. Atkinson, G. M. Branch, W. B. Davenport, W. H. Fonger, W. A. Harris, *et al.*, "Representation of Noise in Linear Twoports," *Proceedings of the IRE*, vol. 48, pp. 69-74, 1960.
- [3] S. P. Voinescu, M. C. Maliepaard, J. L. Showell, G. E. Babcock, D. Marchesan, M. Schroter, *et al.*, "A scalable high-frequency noise model for bipolar transistors with application to optimal transistor sizing for low-noise amplifier design," *IEEE Journal of Solid-State Circuits*, vol. 32, pp. 1430-1439, 1997.
- [4] D. K. Shaeffer and T. H. Lee, "A 1.5-V, 1.5-GHz CMOS low noise amplifier," *IEEE Journal of Solid-State Circuits*, vol. 32, pp. 745-759, 1997.
- [5] P. Andreani and H. Sjoland, "Noise optimization of an inductively degenerated CMOS low noise amplifier," *IEEE Transactions on Circuits and Systems II: Analog and Digital Signal Processing*, vol. 48, pp. 835-841, 2001.
- [6] D. Zhiming and A. M. Niknejad, "On the Noise Optimization of CMOS Common-Source Low-Noise Amplifiers," *IEEE Transactions on Circuits and Systems I: Regular Papers*, vol. 58, pp. 654-667, 2011.
- [7] S. Ullah, H. Higgins, B. Braem, B. Latre, C. Blondia, I. Moerman, *et al.*, "A Comprehensive Survey of Wireless Body Area Networks," *Journal of Medical Systems*, vol. 36, pp. 1065-1094, 2012/06/01 2012.
- [8] B. Regal, *Radio : the life story of a technology*. Westport, Conn.: Greenwood Press, 2005.
- [9] O. J. LODGE, US609154, Aug 16, 1898.
- [10] G. MARCONI, US627650, Jun 27, 1899.
- [11] E. H. Armstrong and R. C. o. America, *The Legacies of Edwin Howard Armstrong: The Regenerative Circuit, the Superheterodyne Circuit, the Superregenerative Circuit, Frequency Modulation*: Radio Club of America, 1990.
- [12] K. B. Schad, H. Schumacher, and A. Schuppen, "Low-power active mixer for Ku-band application using SiGe HBT MMIC technology," in *Microwave Symposium Digest. 2000 IEEE MTT-S International*, 2000, pp. 397-400 vol.1.
- [13] N. M. Madani, J. Hadi, and S. M. Fakhraie, "Design and implementation of a fully digital 4FSK demodulator," in *Circuit Theory and Design, 2005. Proceedings of the 2005 European Conference on*, 2005, pp. III/277-III/280 vol. 3.
- [14] B. P. Lathi and Z. Ding, *Modern digital and analog communication systems*. New York: Oxford University Press, 2010.
- [15] L. W. Couch, *Digital and Analog Communication Systems*, 8th ed.: Pearson Education, 2013.
- [16] R. V. L. Hartley, "Modulation System," U. S. Patent 1 666 206, Apr 17, 1928.
- [17] D. K. Weaver, "A Third Method of Generation and Detection of Single-Sideband Signals," *Proceedings of the IRE*, vol. 44, pp. 1703-1705, 1956.
- [18] T. Okanobu, H. Tomiyama, and H. Arimoto, "Advanced low voltage single chip radio IC," *Consumer Electronics, IEEE Transactions on*, vol. 38, pp. 465-475, 1992.
- [19] B. Razavi, "Design of Millimeter-Wave CMOS Radios: A Tutorial," *Circuits and Systems I: Regular Papers, IEEE Transactions on*, vol. 56, pp. 4-16, 2009.
- [20] A. Mashhour, W. Domino, and N. Beamish, "On the direct conversion receiver - A tutorial," *Microwave Journal*, vol. 44, pp. 114-128, 2001.

- [21] J. Vankka and K. A. Halonen, *Direct digital synthesizers: theory, design and applications*: Springer, 2001.
- [22] V. Giannini, J. Craninckx, and A. Baschirotto, *Baseband analog circuits for software defined radio*: Springer, 2008.
- [23] Z. Yuanjin, Y. Jiangnan, and X. Yong Ping, "A CMOS VGA With DC Offset Cancellation for Direct-Conversion Receivers," *Circuits and Systems I: Regular Papers, IEEE Transactions on*, vol. 56, pp. 103-113, 2009.
- [24] M. Inamori, A. Bostamam, Y. Sanada, and H. Minami, "IQ imbalance compensation scheme in the presence of frequency offset and dynamic DC offset for a direct conversion receiver," *Wireless Communications, IEEE Transactions on*, vol. 8, pp. 2214-2220, 2009.
- [25] I. Kwon, "Low-power design of CMOS baseband analog chain for direct conversion receiver," *International Journal of Circuit Theory and Applications*, vol. 38, pp. 111-122, 2010.
- [26] A. Mirzaei, H. Darabi, J. C. Leete, C. Xinyu, K. Juan, and A. Yazdi, "Analysis and Optimization of Current-Driven Passive Mixers in Narrowband Direct-Conversion Receivers," *Solid-State Circuits, IEEE Journal of*, vol. 44, pp. 2678-2688, 2009.
- [27] S. Jin-Siang, M. Chin-Chun, T. Ya-Hui, and L. Hua-Yu, "Large Improvement in Image Rejection of Double-Quadrature Dual-Conversion Low-IF Architectures," *Microwave Theory and Techniques, IEEE Transactions on*, vol. 58, pp. 1703-1712, 2010.
- [28] N. Trung-Kien, O. Nam-Jin, L. Viet-Hoang, and L. Sang-Gug, "A low-power CMOS direct conversion receiver with 3-dB NF and 30-kHz flicker-noise corner for 915-MHz band IEEE 802.15.4 ZigBee standard," *Microwave Theory and Techniques, IEEE Transactions on*, vol. 54, pp. 735-741, 2006.
- [29] M. Camus, B. Butaye, L. Garcia, M. Sie, B. Pellat, and T. Parra, "A 5.4mW 0.07mm² 2.4GHz Front-End Receiver in 90nm CMOS for IEEE 802.15.4 WPAN," in *Solid-State Circuits Conference, 2008. ISSCC 2008. Digest of Technical Papers. IEEE International*, 2008, pp. 368-620.
- [30] C. Namjun, L. Jeabin, Y. Long, B. Joonsung, K. Sunyoung, and Y. Hoi-Jun, "A 60kb/s-to-10Mb/s 0.37nJ/b Adaptive-Frequency-Hopping Transceiver for Body-Area Network," in *Solid-State Circuits Conference, 2008. ISSCC 2008. Digest of Technical Papers. IEEE International*, 2008, pp. 132-602.
- [31] K. Kyung-Sup, S. Ullah, and N. Ullah, "An overview of IEEE 802.15.6 standard," in *Applied Sciences in Biomedical and Communication Technologies (ISABEL), 2010 3rd International Symposium on*, 2010, pp. 1-6.
- [32] *IEEE 802.15 WPAN™ Task Group 6 (TG6) Body Area Networks*. Available: <http://www.ieee802.org/15/pub/TG6.html>
- [33] Beno, #238, t. Latr, #233, B. Braem, I. Moerman, *et al.*, "A survey on wireless body area networks," *Wirel. Netw.*, vol. 17, pp. 1-18, 2011.
- [34] M. Chen, S. Gonzalez, A. Vasilakos, H. Cao, and V. M. Leung, "Body Area Networks: A Survey," *Mobile Networks and Applications*, vol. 16, pp. 171-193, 2011/04/01 2011.
- [35] L. Miaoxin and Z. Mingjie, "An overview of Physical layers on wireless body area network," in *Anti-Counterfeiting, Security and Identification (ASID), 2012 International Conference on*, 2012, pp. 1-5.
- [36] J. Rogers and C. Plett, *Radio Frequency Integrated Circuit Design*, 2nd ed. Boston: Artech House, 2010.
- [37] B. Razavi, "Cognitive Radio Design Challenges and Techniques," *Solid-State Circuits, IEEE Journal of*, vol. 45, pp. 1542-1553, 2010.

- [38] A. J. Scholten, L. F. Tiemeijer, R. van Langevelde, R. J. Havens, A. T. A. Zegers-van Duijnhoven, and V. C. Venezia, "Noise modeling for RF CMOS circuit simulation," *Electron Devices, IEEE Transactions on*, vol. 50, pp. 618-632, 2003.
- [39] J. J. Ou, J. Xiaodong, H. Chenming, and P. R. Gray, "Submicron CMOS thermal noise modeling from an RF perspective," in *VLSI Technology, 1999. Digest of Technical Papers. 1999 Symposium on*, 1999, pp. 151-152.
- [40] A. J. Scholten, H. J. Tromp, L. F. Tiemeijer, R. van Langevelde, R. J. Havens, P. W. H. de Vreede, *et al.*, "Accurate thermal noise model for deep-submicron CMOS," in *Electron Devices Meeting, 1999. IEDM '99. Technical Digest. International*, 1999, pp. 155-158.
- [41] T. H. Lee, *The design of CMOS radio-frequency integrated circuits*, 2nd ed. Cambridge, : Cambridge University Press, 2004.
- [42] R. P. Jindal, "Compact Noise Models for MOSFETs," *Electron Devices, IEEE Transactions on*, vol. 53, pp. 2051-2061, 2006.
- [43] G. D. J. Smit, A. J. Scholten, R. M. T. Pijper, R. van Langevelde, L. F. Tiemeijer, and D. B. M. Klaassen, "Experimental Demonstration and Modeling of Excess RF Noise in Sub-100-nm CMOS Technologies," *Electron Device Letters, IEEE*, vol. 31, pp. 884-886, 2010.
- [44] C. C. Enz and E. A. Vittoz, *Charge-based MOS transistor modeling : the EKV model for low-power and RF IC design*. Chichester: Wiley, 2006.
- [45] A. Van Der Ziel, *Noise in Solid State Devices and Circuits*: Wiley, 1986.
- [46] Y. Tsidividis and C. McAndrew, *Operation and modeling of the MOS transistor*, 3rd ed. New York: Oxford University Press, 2011.
- [47] G. D. Vendelin, A. M. Pavio, and U. L. Rohde, *Microwave Circuit Design Using Linear and Nonlinear Techniques*. Hoboken: John Wiley & Sons, 2005.
- [48] S. C. Cripps, *RF power amplifiers for wireless communications*, 2nd ed. Boston: Artech House, 2006.
- [49] N. Trung-Kien, K. Chung-Hwan, I. Gook-Ju, Y. Moon-Su, and L. Sang-Gug, "CMOS low-noise amplifier design optimization techniques," *IEEE Transactions on Microwave Theory and Techniques*, vol. 52, pp. 1433-1442, 2004.
- [50] M. Yargholi and A. P. Tarighat, "Resistive feedback LNA with dual band notch filter for suppressing WLAN signals in UWB receivers," in *Communications (NCC), 2012 National Conference on*, 2012, pp. 1-4.
- [51] L. Hiu Fai and H. C. Luong, "A 1.2-6.6GHz LNA using transformer feedback for wideband input matching and noise cancellation in 0.13um CMOS," in *Radio Frequency Integrated Circuits Symposium (RFIC), 2012 IEEE*, 2012, pp. 17-20.
- [52] C. Ding, W. Zhang, D. Jin, H. Xie, Y. Zhao, Q. Fu, *et al.*, "An inductorless high linear UWB Cascode LNA with tunable active resistance feedback and post-linearization technique," *Microelectronics Journal*.
- [53] H. Kuang-Chi, L. Ming-Tsung, L. Chen-Ming, and T. Jenn-Hwan, "Parallel-RC Feedback Low-Noise Amplifier for UWB Applications," *Circuits and Systems II: Express Briefs, IEEE Transactions on*, vol. 57, pp. 582-586, 2010.
- [54] N. J. Oh, "Corrections to "CMOS Low-Noise Amplifier Design Optimization Techniques" [May 04 1433-1442]," *Microwave Theory and Techniques, IEEE Transactions on*, vol. 55, pp. 1255-1255, 2007.
- [55] N. Trung-Kien, K. Chung-Hwam, I. Gook-Ju, Y. Moon-Su, and L. Sang-Gug, "[Authors' reply to comments on "CMOS low-noise amplifier design optimization techniques"]," *Microwave Theory and Techniques, IEEE Transactions on*, vol. 54, pp. 3155-3156, 2006.

- [56] F. Bruccoleri, E. A. M. Klumperink, and B. Nauta, *Wideband low noise amplifiers exploiting thermal noise cancellation*. Dordrecht [u.a.]: Springer, 2005.
- [57] Y. Yueh-Hua, Y. Yong-Sian, and Y. J. E. Chen, "A Compact Wideband CMOS Low Noise Amplifier With Gain Flatness Enhancement," *Solid-State Circuits, IEEE Journal of*, vol. 45, pp. 502-509, 2010.
- [58] F. Bruccoleri, E. A. M. Klumperink, and B. Nauta, "Wide-band CMOS low-noise amplifier exploiting thermal noise canceling," *Solid-State Circuits, IEEE Journal of*, vol. 39, pp. 275-282, 2004.
- [59] T. B. Merkin, L. Ju-Ching, J. Sungyong, L. Mingyu, J. Gao, and L. Sung Chul, "A 100-960MHz CMOS Ultra-wideband Low noise Amplifier," in *Circuits and Systems, 2008. MWSCAS 2008. 51st Midwest Symposium on*, 2008, pp. 141-144.
- [60] T. Thu Nga Tran, B. Chirn Chye, D. Manh Anh, and Y. Kiat Seng, "Reciprocal noise canceling low power UWB LNA," in *SoC Design Conference (ISOCC), 2009 International*, 2009, pp. 13-16.
- [61] W. Keping, Y. Kiat Seng, M. Kaixue, and W. Zhigong, "An inductorless and capacitorless LNA with noise and distortion cancelation," in *Computer Research and Development (ICCRD), 2011 3rd International Conference on*, 2011, pp. 270-274.
- [62] S. C. Blaakmeer, E. A. M. Klumperink, D. M. W. Leenaerts, and B. Nauta, "Wideband Balun-LNA With Simultaneous Output Balancing, Noise-Canceling and Distortion-Canceling," *Solid-State Circuits, IEEE Journal of*, vol. 43, pp. 1341-1350, 2008.
- [63] W. Hongrui, Z. Li, and Y. Zhiping, "A Wideband Inductorless LNA With Local Feedback and Noise Cancelling for Low-Power Low-Voltage Applications," *Circuits and Systems I: Regular Papers, IEEE Transactions on*, vol. 57, pp. 1993-2005, 2010.
- [64] J. Yoon, H. Seo, I. Choi, and B. Kim, "Wideband LNA Using a Negative gm Cell for Improvement of Linearity and Noise Figure," *Journal of Electromagnetic Waves and Applications*, vol. 24, pp. 619-630, 2010/01/01 2010.
- [65] W. Sanghyun, K. Woonyun, L. Chang-Ho, L. Kyutae, and J. Laskar, "A 3.6mW differential common-gate CMOS LNA with positive-negative feedback," in *Solid-State Circuits Conference - Digest of Technical Papers, 2009. ISSCC 2009. IEEE International*, 2009, pp. 218-219,219a.
- [66] D. Ponton, P. Palestri, D. Esseni, L. Selmi, M. Tiebout, B. Parvais, *et al.*, "Design of Ultra-Wideband Low-Noise Amplifiers in 45-nm CMOS Technology: Comparison Between Planar Bulk and SOI FinFET Devices," *Circuits and Systems I: Regular Papers, IEEE Transactions on*, vol. 56, pp. 920-932, 2009.
- [67] F. Xiaohua, Z. Heng, and E. Sanchez-Sinencio, "A Noise Reduction and Linearity Improvement Technique for a Differential Cascode LNA," *Solid-State Circuits, IEEE Journal of*, vol. 43, pp. 588-599, 2008.
- [68] T. Kihara, T. Matsuoka, and K. Taniguchi, "A transformer noise-canceling ultra-wideband CMOS low-noise amplifier," *IEICE Transactions on Electronics*, vol. E93-C, pp. 187-199, 2010.
- [69] T. Kihara, H. J. Park, I. Takobe, F. Yamashita, T. Matsuoka, and K. Taniguchi, "A 0.5 V Area-Efficient Transformer Folded-Cascode CMOS Low-Noise Amplifier," *Ieice Transactions on Electronics*, vol. E92C, pp. 564-575, Apr 2009.
- [70] M. S. Mehrjoo and M. Yavari, "A low power UWB very low noise amplifier using an improved noise reduction technique," in *Circuits and Systems (ISCAS), 2011 IEEE International Symposium on*, 2011, pp. 277-280.
- [71] Y. Rong-Fu, H. Tzyy-Sheng, and W. Jian-Ming, "Wideband common-gate low-noise amplifier with dual-feedback for simultaneous input and noise matching," in *Radio Frequency Integrated Circuits Symposium (RFIC), 2011 IEEE*, 2011, pp. 1-4.

- [72] T. Kihara, T. Matsuoka, and K. Taniguchi, "A 1.0 V, 2.5 mW, transformer noise-canceling UWB CMOS LNA," in *Radio Frequency Integrated Circuits Symposium, 2008. RFIC 2008. IEEE*, 2008, pp. 493-496.
- [73] S. A. Maas, *Nonlinear microwave and RF circuits*, 2nd ed. Boston, Mass. [u.a.]: Artech House, 2003.
- [74] B. Leung, *VLSI for wireless communication*, 2nd ed. New York; London: Springer, 2011.
- [75] P. Wambacq and W. M. C. Sansen, *Distortion analysis of analog integrated circuits*. Boston: Kluwer, 1998.
- [76] M. C. Schneider and C. Galup-Montoro, *CMOS Analog Design Using All-Region MOSFET Modeling*: Cambridge University Press, 2010.
- [77] Z. Heng and E. Sanchez-Sinencio, "Linearization Techniques for CMOS Low Noise Amplifiers: A Tutorial," *Circuits and Systems I: Regular Papers, IEEE Transactions on*, vol. 58, pp. 22-36, 2011.
- [78] S. Narayanan, "Application of Volterra series to intermodulation distortion analysis of transistor feedback amplifiers," *Circuit Theory, IEEE Transactions on*, vol. 17, pp. 518-527, 1970.
- [79] R. Gharpurey, "Linearity Enhancement Techniques in Radio Receiver Front-Ends," *Circuits and Systems I: Regular Papers, IEEE Transactions on*, vol. 59, pp. 1667-1679, 2012.
- [80] J. Jiming and D. M. Holburn, "Design and analysis of a low-power highly linear mixer," in *Circuit Theory and Design, 2009. ECCTD 2009. European Conference on*, 2009, pp. 675-678.
- [81] Z. ZhiChao, M. R. Khan, C. Li, and D. Anh, "A broadband high linear LNA for GSM/LTE wireless communications," in *Electrical & Computer Engineering (CCECE), 2012 25th IEEE Canadian Conference on*, 2012, pp. 1-4.
- [82] H. M. Geddada, J. W. Park, and J. Silva-Martinez, "Robust derivative superposition method for linearising broadband LNAs," *Electronics Letters*, vol. 45, pp. 435-436, 2009.
- [83] B. Toole, C. Plett, and M. Cloutier, "RF circuit implications of moderate inversion enhanced linear region in MOSFETs," *IEEE Transactions on Circuits and Systems I: Regular Papers*, vol. 51, pp. 319-328, 2004.
- [84] V. Aparin, G. Brown, and L. E. Larson, "Linearization of CMOS LNA's via optimum gate biasing," in *Circuits and Systems, 2004. ISCAS '04. Proceedings of the 2004 International Symposium on*, 2004, pp. IV-748-51 Vol.4.
- [85] D. Yongwang and R. Harjani, "A +18 dBm IIP3 LNA in 0.35 μm CMOS," in *Solid-State Circuits Conference, 2001. Digest of Technical Papers. ISSCC. 2001 IEEE International*, 2001, pp. 162-163, 443.
- [86] T. W. Kim, "A Common-Gate Amplifier With Transconductance Nonlinearity Cancellation and Its High-Frequency Analysis Using the Volterra Series," *Microwave Theory and Techniques, IEEE Transactions on*, vol. 57, pp. 1461-1469, 2009.
- [87] K. Tae Wook, K. Bonkee, and L. Kwyro, "Highly linear receiver front-end adopting MOSFET transconductance linearization by multiple gated transistors," *Solid-State Circuits, IEEE Journal of*, vol. 39, pp. 223-229, 2004.
- [88] V. Aparin, "Linearization of CDMA receiver front-ends," Ph.D. 3167860, University of California, San Diego, United States -- California, 2005.
- [89] V. Aparin and L. E. Larson, "Modified derivative superposition method for linearizing FET low-noise amplifiers," *Microwave Theory and Techniques, IEEE Transactions on*, vol. 53, pp. 571-581, 2005.
- [90] S. Ganesan, E. Sanchez-Sinencio, and J. Silva-Martinez, "A Highly Linear Low-Noise Amplifier," *Microwave Theory and Techniques, IEEE Transactions on*, vol. 54, pp. 4079-4085, 2006.

- [91] A. Liscidini, M. Brandolini, D. Sanzogni, and R. Castello, "A 0.13 μm CMOS front-end, for DCS1800/UMTS/802.11b-g with multiband positive feedback low-noise amplifier," *Solid-State Circuits, IEEE Journal of*, vol. 41, pp. 981-989, 2006.
- [92] K. Tae-Sung and K. Byung-Sung, "Post-linearization of cascode CMOS low noise amplifier using folded PMOS IMD sinker," *Microwave and Wireless Components Letters, IEEE*, vol. 16, pp. 182-184, 2006.
- [93] G. B. Arfken, H.-J. Weber, F. E. Harris, and ScienceDirect, "Mathematical methods for physicists," vol. 7th, ed. Oxford: Academic, 2012.
- [94] S. Ikehara and M. I. o. T. R. L. o. Electronics, *A Method of Wiener in a Nonlinear Circuit: Research Laboratory of Electronics, Massachusetts Institute of Technology*, 1951.
- [95] D. Tannir and R. Khazaka, "Computation of Intermodulation Distortion in RF Circuits Using Single-Tone Moments Analysis," *Computer-Aided Design of Integrated Circuits and Systems, IEEE Transactions on*, vol. 29, pp. 1121-1125, 2010.